

**The Influence of Asteroid Surface Features on the YORP  
Effect and Dynamical Evolution**

by

**Dahlia A. Baker**

B.A., Coe College, 2018

M.S., University of Colorado Boulder, 2021

A thesis submitted to the  
Faculty of the Graduate School of the  
University of Colorado in partial fulfillment  
of the requirements for the degree of  
Doctor of Philosophy

Ann and H.J. Smead Department of Aerospace Engineering Sciences

2024

Committee Members:

Dr. Jay W. McMahon, Chair

Dr. Daniel J. Scheeres

Dr. Paul Sanchez

Dr. Paul Hayne

Dr. William Bottke

Baker, Dahlia A. (Ph.D., Aerospace Engineering Sciences)

The Influence of Asteroid Surface Features on the YORP Effect and Dynamical Evolution

Thesis directed by Dr. Jay W. McMahon

Small rubble-pile asteroids have rocky, rough surfaces and a wide variety of possible shapes that make them unique targets for mapping and estimating their dynamical evolution. The surface undergoes thermal interactions that induce a small additional torque over time. These small torques are the YORP effect, or re-radiated thermal energy from the surface that adds small torques to the spin pole of the body over time and is dependent on the surface material's thermal inertia and the asteroid's spin velocity and spin pole orientation. Much like solar radiation pressure, this interaction with the sun induces perturbations on the spin that can lead bodies secularly towards chaotic or destructive spin states. In order to understand their evolution towards these states, we investigate the relationship between the shape and dynamics. Modeling their shapes accurately requires knowledge of the surface through imagery, and then this contributes to better models of their dynamics since the shape and dynamics are coupled through the thermal interactions of the YORP effect. The limb can show a unique roughness pattern that can then be translated as a feature in three-dimensional space by leveraging what is known about the asteroid spin and orbit state as well as the camera or spacecraft attitude and trajectory. The work presented in this dissertation shows a method for dissecting a limb measurement into many points, associating them from the image frame to the three-dimensional body frame, and performing outlier rejection and shape reconstruction from the many observed points constraining the surface. In this effort, we show our shape modeling resolution and error to evaluate what the upper limit of boulder resolution could be with our methods. This upper limit informs what the largest observable boulder is, and then that is used to inform how accurate of a YORP prediction we are able to make by including boulders down to this size limit. This informs our overall uncertainty in YORP predictions when a shape model is accessible but the boulder population is not known accurately. We model the

impact of boulders on the YORP torque by applying the boulder statistics from mapped asteroid surfaces, adding statistically sampled boulder models to Bennu and Itokawa shape models, and randomizing many of these models to find the likelihood of large boulder-induced changes in the spin velocity and spin pole orientation dynamics. We have found that we can narrow down that YORP-induced torque from boulders is only influential from boulders 1m in diameter and above (equivalently stated as boulders sized at 1/500th of the asteroid diameter). This size regime makes up just 10% of the boulder population based on Bennu, Ryugu, and Itokawa. This reduces the number of features that one is required to model in order to obtain more accurate YORP estimates for a body. However, it also supports the conclusion that single boulders do not dominate the YORP prediction and that multiple of the largest and best placed boulders need to be known about and modeled in order to understand the net effect of YORP from the entire surface population. This also takes into consideration that the largest boulders on the surface are typically stationary, contributing the same influence to YORP over time, while smaller influential boulder motion can cause the walk seen in stochastic YORP.

## **Dedication**

I dedicate this manuscript to my Mom. Thank you for pushing me to strive for great things.

## Acknowledgements

I'd like to acknowledge my tireless advisor, Jay McMahon, for bringing me into the ORCCA lab and letting me do whatever I wanted with my research while supporting me at every step along the way. I have many exciting opportunities ahead of me thanks to you. I am also very grateful to my committee members, Dr. Scheeres, Dr. Hayne, Dr. Sánchez, and Dr. Bottke for their guidance and expertise which shapes this work. I thank my colleagues in the ORCCA Lab and CCAR whose advice, collaboration, and kindness made this all possible. Lyss, you deserve the so much recognition for your compassion and brilliance. Also, my close friend Liane, for giving me so many recipes and endless support and mentorship. Without your friendships, I would not have made it through. I would also like to recognize my professors from the Coe College physics department, who pushed me to continue with my education and became my family in Iowa. Thank you Ugur, Mario, Doc, and Firdevs for your dedication and guidance. Your commitment to student success and excellence in research let me chase my dreams. Another thank you goes to my partner, Nicholas, for your patience and support as I approach graduation and take on a job across the country. Lastly, I want to thank my all of my family and friends who are reading this, who know how difficult this has been and have been there for me in all of the hard times.

## Contents

### Chapter

<b>1</b>	<b>Background and Motivation</b>	<b>1</b>
1.1	Rubble-Pile Asteroid Surfaces . . . . .	1
1.2	Shape Modeling of Small Bodies . . . . .	2
1.3	Dynamics and the YORP effect . . . . .	4
1.4	Thesis Statement . . . . .	7
1.5	Thesis Overview . . . . .	7
1.5.1	Contributions . . . . .	7
<b>2</b>	<b>Boulder-induced YORP Altering Spin Acceleration</b>	<b>9</b>
2.1	Surface Interactions causing YORP . . . . .	9
2.2	Coordinate Frames . . . . .	11
2.3	Fourier YORP Coefficient Modeling . . . . .	13
2.4	Comments on Orbit Averaging . . . . .	15
2.5	Boulder Simulation Design . . . . .	15
2.5.1	Boulder Shape . . . . .	16
2.5.2	Bennu and Itokawa Surfaces . . . . .	18
2.5.3	Boulder Population Studies on Bennu and Itokawa . . . . .	21
2.5.4	Applying a Simplified Thermal Model . . . . .	22
2.5.5	Polyhedral Facet YORP Evaluation . . . . .	23

2.6	Analysis of boulder impact on YORP spin torque . . . . .	24
2.6.1	Power Law Distribution of Boulder Size . . . . .	25
2.6.2	Uniform Distribution of Boulder Location . . . . .	27
2.6.3	Uniform Distribution of Boulder Orientation . . . . .	27
2.6.4	Overall Uncertainty Distribution . . . . .	30
2.7	Bennu Results . . . . .	31
2.7.1	Total Boulder Impact . . . . .	31
2.7.2	Large Influence Boulder Parameters . . . . .	33
2.8	Itokawa Results . . . . .	35
2.8.1	Total Boulder Impact . . . . .	35
2.8.2	Large Influence Boulder Parameters . . . . .	36
2.9	Sensitivity Analysis . . . . .	38
2.9.1	Size Thresholding . . . . .	38
2.9.2	Orientation Biases: West Preference . . . . .	41
2.9.3	Location Bias: Polar Migration . . . . .	42
2.10	Efficiency of Boulder Shape . . . . .	44
2.11	Total YORP Discussion . . . . .	44
2.11.1	Crater YORP . . . . .	44
2.11.2	Tangential YORP . . . . .	46
2.11.3	Overall YORP Comparison . . . . .	48
2.12	Application to YORP Estimates . . . . .	50
2.13	Boulder Motion . . . . .	51
2.14	Summary of Spin Evolution Findings . . . . .	53
<b>3</b>	<b>Obliquity Evolution under Boulder-Induced YORP Torques</b>	<b>56</b>
3.1	YORP Torques for Obliquity . . . . .	56
3.2	Results . . . . .	57

3.2.1	Boulder Distribution Effects on Solar Inclination Change Rates . . . . .	57
3.2.2	Sensitivity . . . . .	58
3.2.3	Boulder Motion . . . . .	62
<b>4</b>	<b>Shape-from-Silhouette Modeling of Small Bodies</b>	<b>64</b>
4.1	Introduction . . . . .	64
4.2	2D to 3D Mapping of Images to Shapes . . . . .	65
4.2.1	Assumptions . . . . .	65
4.2.2	Simulated Image Procedure . . . . .	65
4.2.3	Mission Data . . . . .	65
4.2.4	Identification of the Silhouette . . . . .	66
4.2.5	Terminator and Limb Discrimination . . . . .	70
4.2.6	Ray Generation and Trimming . . . . .	71
4.2.7	Outlier Rejection Scheme . . . . .	75
4.2.8	Surface Reconstruction with Ball-pivoting . . . . .	75
4.3	Shape Results . . . . .	76
4.3.1	Simulated Data . . . . .	76
4.3.2	Shape Modeling from Mission Data . . . . .	79
4.4	Matching Localization with Normalized Cross-Correlation . . . . .	81
4.4.1	Methods . . . . .	81
4.4.2	Results . . . . .	82
4.5	Analysis . . . . .	85
4.5.1	Error Evaluation . . . . .	85
4.5.2	Boulder Resolution . . . . .	86
<b>5</b>	<b>Conclusion and Future Work</b>	<b>88</b>
5.1	Summary . . . . .	88
5.2	Applications of Boulder YORP Modeling . . . . .	89

5.3 Further Investigations . . . . .	89
--------------------------------------	----

**Tables****Table**

2.1	Bennu's Properties and Itokawa's Properties . . . . .	20
2.2	Coefficients for the sum of sines fit of boulder YORP for single boulder at equator and aligned to body $-\hat{x}$ axis. . . . .	29

## Figures

### **Figure**

2.1 Diagram of solar radiation, absorption, and YORP re-radiation . . . . .	10
2.2 Body frame diagram which shows $\hat{u}$ , the sun-pointing vector, $\hat{u}_{  xy}$ , the projection of the sun-pointing vector into the body x-y plane, $\hat{u}_\perp$ , the perpendicular vector to the sun-pointing vector, the body frame unit vectors $\hat{x}_B, \hat{y}_B$ , and $\hat{z}_B$ , as well as the solar inclination angle $i_s$ , the longitude of the ascending node $\Omega_s$ , and the spin pole obliquity angle $\eta$ . . . . .	13
2.3 First-order YORP spin coefficient variation per facet on Bennu and Itokawa . . . . .	16
2.4 Wedge shape boulders provide asymmetry that induces YORP effect . . . . .	17
2.5 Boulder model with frame . . . . .	18
2.6 Difference of per-facet distance from body center of mass and the average radius for three asteroid shape models: Bennu, Ryugu, and Itokawa. Darker points represent equatorial facets. Itokawa exhibits the greatest variation over longitude. . . . .	19
2.7 Cumulative number of boulders per square km . . . . .	22
2.8 Orientation of Prism Boulder Rotating from West to East, from 0 to $\pi$ . . . . .	27
2.9 Sinusoidal relationship of boulder orientation to YORP torque. Asymmetric boulder at equator and perfectly tangent to spin pole . . . . .	29
2.10 Frequency distribution of YORP with 500 random boulder populations for Bennu . .	32
2.12 Bennu distribution comparison of normalized frequencies of boulder latitude and orientation in the > 1% YORP spin coefficient boulder population. . . . .	33

2.11 Size distribution and mean diameter of boulders where $C_{0,z,i} > 1\%$ on Bennu . . . . .	33
2.13 Frequency distribution of total boulder YORP spin coefficients for Itokawa . . . . .	35
2.14 Size distribution and mean diameter of boulders where $C_{0,z,i} > 1\%$ for Itokawa . . . . .	36
2.15 Itokawa distribution comparison of normalized frequencies of boulder latitude and orientation in the $> 1\%$ YORP spin coefficient boulder population. . . . .	37
2.16 Change in Bennu's global YORP spin coefficient with boulders, shown in Fig.2.12, when removing boulders $< 1\text{m}$ , roughly 99% of original population. . . . .	39
2.17 Overlaid distribution of normalized YORP with and without 1 m boulders . . . . .	39
2.18 Boulder spin coefficients for Bennu, separated by size bins. Percentages represent the proportion of boulders in each bin to the size of the sample population. . . . .	40
2.19 Change in global YORP spin coefficient when enforcing a percentage of boulders with a westward orientation bias. Each profile is a histogram of global YORP spin coefficients. The black histogram represents the 100% west bias for all boulders . . . . .	41
2.20 Change in asteroid global YORP spin coefficients when removing boulders outside of $\pm 30^\circ$ latitude, varying the percentage until 100% are outside of the the bounds equivalent to a liberal cushion about Bennu's Roche lobe . . . . .	43
2.21 Normalized CYORP Contribution scaled by crater diameter frequency . . . . .	45
2.22 Incorporating the assumption of smooth transitions below and above the ideal thermal inertia length, $L_{cond}$ with a logarithmic scale factor . . . . .	46
2.23 Comparison of analytical YORP spin components for Bennu as a function of obliquity	49
2.24 Comparison of mean and standard deviation from several YORP models . . . . .	50
2.25 Differing amounts of YORP spin acceleration for boulders within 5 degrees in longitude but varying latitudes . . . . .	52
2.26 The change in YORP spin acceleration from boulder motion with the latitude degree change shown on the x-axis . . . . .	53

3.1	Solar Inclination Rates for entire asteroid with 5000 boulders added in 500 different configurations of size, orientation, and location on Bennu and Itokawa shape models	58
3.2	Boulder diameter power laws: dashed line is the model and histogram represents the population sampled from power law . . . . .	59
3.3	Full histogram of boulder diameters compared to the subsampled set that represents boulders contributing > 1% to solar inclination change . . . . .	59
3.4	Varying bins of percent contribution to solar inclination change, with darker colors representing higher % change from a single boulder, distributed over dominant pointing direction . . . . .	60
3.5	Boulder locations separated by percent contribution, showing a departure of boulders from equator at rates of > 1% and > 10% for both bodies . . . . .	61
3.6	Differing amounts of YORP obliquity acceleration for boulders within 5 degrees in longitude but varying latitudes . . . . .	62
3.7	The change in YORP obliquity rate from boulder motion with the latitude degree change shown on the x-axis . . . . .	63
4.1	Example Images . . . . .	66
4.4	Four Edge Results Overlaid in Image Space . . . . .	68
4.3	25 Examples of Canny Parameters and Impact on Edge Detection . . . . .	69
4.5	Limb and Terminator in Bennu Mission Image . . . . .	70
4.6	Geometry of Two Intersecting Planes . . . . .	71
4.7	Geometric Depiction of Patch Crossing Calculations . . . . .	73
4.8	Intersection Ray from Two Patches - Ten Sampled Points and Associated Ray Normals	74
4.9	Ball-Pivoting Surface Reconstruction Results of Itokawa and Bennu Point Clouds .	76
4.10	Pre- and Post-Processed Point Cloud of Itokawa Limb-Trimmed Shape . . . . .	77
4.11	Limb-based Itokawa shape compared to SPC, with surface error in units of kilometers	78
4.12	Pre- and Post-Processed Point Cloud of Bennu Limb-Trimmed Shape . . . . .	78

4.13 Limb-based Bennu shape compared to SPC, with surface error in units of kilometers	79
4.14 Bennu Shape Model from Real Images, compared to SPC, surface error in kilometers	81
4.15 Test image and Library Image, Expected Match Pair . . . . .	83
4.16 Test Image and Library image, Actual Match Pair . . . . .	84
4.17 2D Correlation scores between all library images and all test images, based on longitude	85

# Chapter 1

## Background and Motivation

### 1.1 Rubble-Pile Asteroid Surfaces

Studying asteroids is important to understanding the origin of our own planet. They are remnants of the protoplanetary disk, and provide insights as to the composition of the original materials that eventually formed rocky planets as well as gaseous ones. In this work, I will be focusing on the smallest members of the asteroid population and the unique dynamics at play in their evolution. We will discuss their composition, dynamics, and environmental concerns for imaging in a navigation context. Their shapes are unique and studying them provides much deeper context to the forces that made up our own planet. Refining the forces that influence these asteroids today can also improve our orbit estimates and give better predictions of what asteroids are potentially hazardous.

Small asteroids are often made up of many separate particles and boulders which is why they are referred to as "rubble piles" (Scheeres, 2018). Often originating from a previous impact event of a parent body, the many pieces come together over time and bond by weak gravity and electrostatic cohesion (Walsh, 2018). These bodies are resilient and active, frequently resurfacing, losing particles, and experiencing further bombardment. By our recent visits to asteroid targets in the sub-1 km size regime, we have seen high-resolution examples of these bodies and been able to characterize the boulders and regolith on their surfaces. These missions produced shape models that enabled both science and navigation. The OSIRIS-REx mission successfully orbited around the 492 m diameter asteroid Bennu for two years, measuring the gravitational properties and taking images to constrain

the shape (Scheeres et al., 2019). We observed the extremely dark and unexpectedly rocky surface of Bennu and even witnessed particle escape (Hergenrother et al., 2019). The sample taken from Bennu has already returned to Earth to undergo testing and characterization which will tell us more about the materials we should expect to find on B-type asteroids like Bennu in the future (Lauretta et al., 2023). Another recent mission that demonstrated the capabilities of asteroid rendezvous and high-resolution shape modeling was Hayabusa2, launched by JAXA to arrive at Itokawa in 2018 (Watanabe et al., 2019). This mission characterized the irregularly shaped body Itokawa and also furthered asteroid science in unexpected ways. One way includes the expansion of YORP theory and also furthering evidence of the presence of contact binaries in the near-earth asteroid population.

## 1.2 Shape Modeling of Small Bodies

The accurate capture of the surface and bulk shape is an important data product for science and navigation. It enables the precise mapping of the gravity field, and better target characterization for relative navigation solutions. One method for creating a shape model is by the combination of optical images which capture various poses and features of the target body.

When spacecraft are deployed to study small bodies in our solar system, they lose the consistent ability to access classical systems for communication such as the Deep Space Network which relays messages from the ground-based operators. However, as the sensitivity of the actions executed by these spacecraft increases, such as during the Touch-And-Go maneuver that OSIRIS-REx achieved when sampling the surface of Bennu (Berry et al., 2013), autonomy becomes critical. With radio communications, there is a delay of minutes between sending commands and their execution time which can mean the difference between a landing and a large miss when targeting small bodies for rendezvous or even flybys. This necessary level of autonomy can be achieved by allowing for the onboard processing capabilities that enable navigation and mission-related decision making. Optical information is the primary focus of this study for its advanced development in navigating spacecraft (Owen, 2011), despite it's challenges in the space environment (DellaGiustina et al., 2018), where careful planning is required to handle the varying lighting conditions. This work focuses on the con-

struction of the shape model data product during the approach trajectory phase when the body has many pixels of resolution and the silhouette is discernible. This moves away from feature-focused shape modeling approaches such as SPC (Gaskell et al., 2008), stereophotogrammetry (shape from motion)(Hartley and Zisserman, 2000), and many other algorithms which identify shadows, craters, rocks and boulders, and even ridges in order to inform the shape. These alternate methods use specific feature detector algorithms to identify surface variations mathematically (Lowe, 2004). It is simpler to take advantage of the contrast of a high-albedo body versus a background of space in order to extract a silhouette which can be identified as the limb and terminator of the observable surface. The capabilities accessed via this data type have been shown in previous limb-focused localization approaches by Christian (Christian, 2017).

Silhouette-based methods of shape modeling are used extensively for the reconstruction of singular objects in the computer vision community(Franco et al., 2009)(Matusik et al., 2000)(Boyer and Franco, 2003). As the small-body community encounters a similar problem, there is a push to investigate limb information as a solution to onboard processing limitations (Panicucci et al., 2020)(Liounis, 2018). A limb refers to the contour of the edge of the body on the lit side and is differentiated from the background of space. A shape such as an asteroid or a binary system is a good candidate and many variations of these natural shapes have been investigated by previous studies. Alongside simulated tool development, these practices have been applied in-house for mission data solutions. The OSIRIS-REx mission developed and applied a limb-based tool (LIMBER) to resolve a pre-SPC model with accuracy of 3-4m when image frequency was  $10^\circ$  and the spacecraft was located in a hovering position within 200km from the target (E.E. Palmer, J.R. Weirich, 2019). Their approach followed very similar procedure as the work presented here, but was not able to apply information from the terminator. Other teams have focused on a similarly simulated method based on finding the silhouette and carving the 3D shape from a preset voxel cube (Bandyonadhyay et al., 2019). The aim of each of these efforts is to show that the silhouette information is both robust and computationally efficient as a candidate for onboard processing. Previous work has highlighted the requirements of the image processing stage when sourcing limb information from

optical data (Li et al., 2013). The shape model built using approach observations in the optical range can reach a precision level high enough for navigation purposes with few assumptions at the current stage of development. The future goal is to evolve a dynamic shape model stored onboard, which can be used to inform future navigation decisions; this would improve the overall mapping performance, heightening the autonomy of the mission (Pesce, Agha-Mohammadi, and Lavagna, 2018).

In this work, the models presented are generated from simulated data sources and compared to the most resolute shape models available for the bodies in question. The method is tested on both a convex and irregular body in order to show how our overlaid silhouette trimming procedure responds to self-shadowing, the presence of concavity, as well as phase angle projections of the terminator introduced by the orientation of the sun and camera. This algorithm will be developed as necessary to enable onboard shape model generation, but this paper serves to present and defend the method which uses a process of refinement based on extending the shape along the silhouette cutout in space, and narrowing down the three-dimensional hull through multiple viewing angles. As the small body community looks to grant more SIMPLEx-level missions to asteroids, it is necessary to develop the autonomous onboard navigation capabilities that make those missions possible.

### **1.3 Dynamics and the YORP effect**

Small bodies in our solar system and particularly in the near-earth environment are of interest to scientists for their resources, their connection to the proto-planetary origins of our Earth, and the possible threat of impact with our planet. Many factors make this population difficult to characterize, such as their limited size, low albedo surfaces, and the difficulty of predicting precise orbits due to low frequency of observation and unmodeled forces. Collective survey efforts have yielded a possible 30% of the  $>100\text{m}$  population found while the rest remain undiscovered. Observation efforts are increased each year in order to increase the database of known bodies and also our confidence in the dynamics of dangerous suspects that could intersect with our own planet's orbit (Jones, Jurić, and Ivezić, 2016)(Mainzer et al., 2011). These efforts reveal new targets for space missions that aim

to flyby or rendezvous with small bodies to learn more about their surfaces and possibly conduct sample return for deeper Earth-based compositional analysis. In any case, the entire size range of small bodies is of high interest to the scientific and planetary defense communities. This work focuses on the smallest members of the asteroid population, bodies under 1km in diameter, and the particular thermal interactions changing their orbit in ways that have only recently been observed. We have just discussed the motivation towards shape modeling for navigation purposes, and now we will apply what is known of these shapes towards further understanding of the dynamics of small bodies as a whole.

The Yarkovsky-O'Keefe-Radzievskii-Paddack (YORP) effect is a force that becomes dominant for asteroids with a diameter below one kilometer. This is a radiation recoil force that acts to change the spin rate and pole orientation via asymmetries in the shape of a body. The surface imparts additional torque during the process of absorbing and re-radiating thermal energy that applies secular forces over the course of it's rotational day and year. The surface asymmetries of the body contribute to the change in the spin rate, either spinning the body up or down depending on the bias of the features. Spin-pole obliquity change occurs due to global deviations in symmetry, imparting a tilt on the spin axis which could eventually lead to tumbling. Note that the YORP effect is acting purely on the local attitude of the body via interactions with the surface and it's irregularities, while the Yarkovsky effect acts on all bodies to cause a change in the semi-major axis of the orbit due to the thermal inertia that retains solar heating and emits it at a different phase angle(Vokrouhlický, Milani, and Chesley, 2000). We have thus far observed 12 bodies in our solar system that exhibit dynamical changes due to YORP (Durech et al., 2023). This is due to the increase in efforts to observe and model the YORP effect. It is shown that YORP is extremely sensitive to small-scale topography such as boulders and craters on the surface, or even a smaller approximation of surface roughness through regolith modeling (Statler, 2009)(Rozitis and Green, 2011)(Rozitis and Green, 2013). It is of significant interest to characterize YORP accounting for common features of small bodies in the YORP-dominant size regime, such as boulders, craters, and regolith (Zhou and Michel, 2023)(Walsh et al., 2019). We choose to investigate the populations and properties of boulders.

Boulders have geological significance because they hold information about local surface processes and natural movement of materials (Murdoch et al., 2015). For the case of small bodies, we assume boulder motion is due to local landslides, regolith redistribution from tidal forces or planetary encounters, and surface sublimation causing fracturing (Delbo et al., 2022) (Barnouin et al., 2022). The parameters of size, shape, texture, and comparative composition are all indicators of the time history of geological evolution for a small body. Boulders have been found on all rubble-pile asteroids and they contribute unique properties thermally, geologically, and dynamically (Küppers et al., 2012). As fractured protrusions, they absorb and radiate heat tangent to the surface (Golubov and Lipatova, 2022). Their continuous motion and degeneration contributes majorly to the changing shape of small bodies (Molaro et al., 2020) (Scheeres, 2015)(Scheeres, 2018)(Zhang et al., 2022). Lastly, they are a vehicle of energy dissipation via infilling, escape, and aggregation (Holsapple, 2010). Due to the small sample size of observed asteroid surfaces, there is no deterministic way to analyze the boulder distribution on all possible asteroid shapes. The surfaces that are available for analysis come from recent mapping and sample acquisition missions such as OSIRIS-REx which successfully mapped Bennu to a mean accuracy of 30 cm (Bennett et al., 2021). Despite this, the possible shapes of small bodies in our solar system are highly variable and extremely difficult to constrain from ground-based observations. The approach taken in this work is to develop statistical approximations for the size and frequency of boulders on an asteroid surface from the currently available image datasets (DellaGiustina et al., 2019)(Fujiwara et al., 2006)(Watanabe et al., 2019).

In this work, we will largely focus on calculating the normal YORP torque, produced from the absorption and re-radiation of thermal energy from a facet-approximated surface and an array of boulders artificially included in the shape. Other ways that the YORP effect is observed are in crater YORP and tangential YORP. Tangential YORP is also the result of protrusive features as they allow for the possibility of total thermal acclimation that will result in a pro-spin radiative force. This is because the boulder diameter is less than the thermal skin depth for a body of ideal specific heat, thermal conductivity, and spin rate (Golubov, 2017).

This approximation serves to constrain the possible variability in YORP due to boulders

for bodies in these size regimes. Rather than using a purely stochastic random walk approach, the uncertainty is informed by Monte Carlo simulation of a known shape decorated with boulder populations following the distributions modeled after real surfaces. We approach the question of YORP variability from a new direction, using observational data to calculate possible bounds on YORP torque due to the additional presence of boulders. We will characterize the magnitude of YORP spin torque due to a singular boulder in different conditions.

## 1.4 Thesis Statement

The thesis of this work can be summarized with the following statement:

*This research models and analyzes the effect of boulder populations on asteroid surfaces to characterize the uncertainty in the YORP spin rate and obliquity evolution due to these features. This informs model resolution requirements for more accurate characterization of the YORP effect from ground-based measurements.*

## 1.5 Thesis Overview

### 1.5.1 Contributions

This dissertation

- (1) Developed a method to statistically analyze the impact of boulder populations on YORP
- (2) Demonstrated by comparison that meter-level uncertainty of boulders on asteroid surfaces is the largest contributor to uncertainty in the YORP effect for sub-half kilometer diameter bodies
- (3) Found that boulders of 1/500th of the asteroid radius contribute 99% of YORP spin acceleration but make up 1.5% of the modeled population
- (4) Identified the boulder size range and locations that can drive the pole obliquity to change significantly

- (5) Developed shape-from-silhouette methods for on-board preliminary shape modeling and identifies resolution requirements for YORP model accuracy

## Chapter 2

### Boulder-induced YORP Altering Spin Acceleration

#### 2.1 Surface Interactions causing YORP

The YORP effect was first named by Rubincam, however it had been recognized as a secular component of small body dynamics for many years previous (Rubincam, 2000). Today it is observed on many bodies where we are capable of taking high precision measurements of spin rate change over time (Lowry et al., 2007). The general mechanism of YORP is the absorption and re-emission of thermal energy of the surface, dependent on the thermal inertia of the material, incident angle of sunlight, the body's orbit, and the current rotational velocity. The direction of this re-emission is the direction of the YORP force. As this is a force acting on the surface, the force is then translated to a torque about the central spin pole. In Fig.2.1, the incident angle of photons is shown by  $\alpha$ , the angle between the surface normal  $\hat{n}$  and the sun direction  $\hat{u}$ . The force is decomposed into its normal and transverse components,  $d\mathbf{F}_{\hat{n}}$  and  $d\mathbf{F}_t$  respectively. The direction  $\hat{s}$  corresponds to the direction of radiation, while  $p_{sr}$  and  $p_{\hat{u}}$  are the directions of torque due to solar re-radiation and incident solar energy.

Statler has shown through simulation that the YORP effect is extremely sensitive to changes in the small-scale topography of a surface, whether Gaussian roughness, craters, or boulders. This work states that at most 50% of the variance in YORP can be attributed to boulders larger than half the maximum size, which could be just one to five boulders in any given case due to steep power law size distributions (Statler, 2009). Overall, many studies have concluded that YORP is sensitive to small features and that the geometric and thermal properties of these features must be

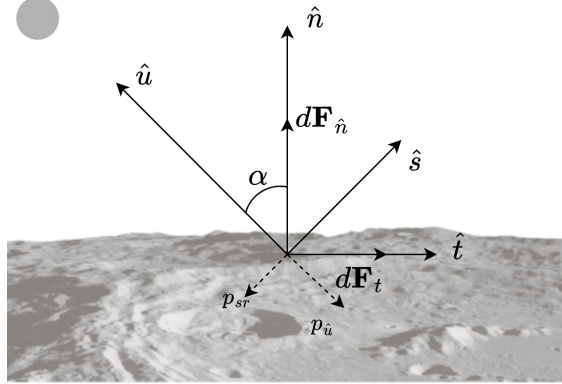


Figure 2.1: Diagram of solar radiation, absorption, and YORP re-radiation

taken into account for a fully representative YORP model (Breiter et al., 2009).

Different thermophysical models have been proposed to increase accuracy of YORP predictions for surfaces. These models can be one-dimensional or three-dimensional, and instantaneous or time delayed (Rozitis and Green, 2012). In this work, we use a one-dimensional instantaneous thermal model which is dependent only on emission directions and assumes diffuse Lambertian re-radiation of photons, and a low surface reflectivity or albedo of 0.05, which represents the dark surfaces seen on rubble-pile bodies such as Bennu (Golish et al., 2021). This is to follow the approximations made by Scheeres for the polyhedral normal YORP model (Scheeres, 2007).

Accounting for surface roughness can change predicted YORP torque depending on the magnitude at which it is modeled (Davidsson and Rickman, 2014) (Davidsson et al., 2015). One can go down to the microscopic level using the Hapke model for emission directions of regolith as was previously done in an examination of tumbling bodies experiencing YORP (Breiter and Vokrouhlický, 2011). However, there is a range of roughness at the size regime of the diurnal thermal skin depth (1 cm) and greater that was ignored. This is addressed as thermal-infrared beaming emission modeling done by Rozitis and Green (Rozitis and Green, 2011). Roughness was modeled as a combination of craters with varying depths and opening angles, as well as low- and high-resolution Gaussian random height models to represent surface variability at the range of 1 cm to several meters. Results from this modeling show that when directional thermal-infrared beaming is considered

for a surface, the YORP torque can be damped by up to half of its original magnitude for a zero-obliquity rotating body. This model also assumes similar surface geometry as the original smooth facet model, and is therefore not equivalent to modeling boulder features which include new normal directions which perturb the original surface geometry drastically. Modeling boulders, craters, and regolith roughness in tandem correlates a more accurate model for YORP and informs the bounds of variability with higher precision and confidence. Other dynamical models address the nature of tumbling bodies, which is a possible end-state induced by long-term influence of YORP re-emission (Cicalò and Scheeres, 2010) (Breiter and Murawiecka, 2015). In order to investigate the sensitivity of YORP to boulder parameters, we will continue with a uniform principal-axis rotator that is not near a dynamical end-state of spinning up to disaggregation or spinning down to a dissipative low-energy tumbling state.

## 2.2 Coordinate Frames

The coordinate frames required to examine YORP obliquity evolution are the inertial frame, the body-fixed frame, and the heliocentric orbit frame. The variables of motion being used are expressed in the body and orbital contexts. The inertial frame is given by the unit vectors  $\hat{\mathbf{X}}_i$ ,  $\hat{\mathbf{Y}}_i$ , and  $\hat{\mathbf{Z}}_i$ . The heliocentric orbit frame is then defined by  $\hat{\mathbf{X}}_H$ , which is the unit vector pointing towards the argument of perihelion,  $\hat{\mathbf{Z}}_H$ , which aligns with the orbit angular momentum direction out of plane, and  $\hat{\mathbf{Y}}_H$ , the third vector which completes this right-handed frame definition and aligns with the velocity vector at perihelion passage. Applying classical orbit elements, we express our heliocentric orbit frame in the inertial frame as follows.

$$\begin{aligned}\hat{\mathbf{X}}_H = & [\cos \bar{\omega} \cos \Omega - \sin \bar{\omega} \sin \Omega \cos i] \hat{\mathbf{X}}_E \\ & + [\cos \bar{\omega} \sin \Omega + \sin \bar{\omega} \cos \Omega \cos i] \hat{\mathbf{Y}}_E \\ & + \sin \bar{\omega} \sin i \hat{\mathbf{Z}}_E\end{aligned}\quad (2.1)$$

$$\begin{aligned}
\hat{\mathbf{Y}}_H = & -[\sin \bar{\omega} \cos \Omega + \cos \bar{\omega} \sin \Omega \cos i] \hat{\mathbf{X}}_E \\
& + [-\sin \bar{\omega} \cos \Omega + \cos \bar{\omega} \cos \Omega \cos i] \hat{\mathbf{Y}}_E \\
& + \cos \bar{\omega} \sin i \hat{\mathbf{Z}}_E
\end{aligned} \tag{2.2}$$

$$\hat{\mathbf{Z}}_H = \sin \Omega \sin i \hat{\mathbf{X}}_E - \cos \Omega \sin i \hat{\mathbf{Y}}_E + \cos i \hat{\mathbf{Z}}_E \tag{2.3}$$

In these equations,  $i$  is inclination of the orbit,  $\Omega$  is the longitude of ascending node, and  $\bar{\omega}$  is the longitude of ascending node as per Scheeres' 2007 notation. We will make use of the body frame notation in our equations of motion in order to describe the YORP accelerations experienced by the surface and how they are influencing the spin pole directly. These forces can be translated to the orbital or inertial frame by these frame definitions given here. The body frame is defined here with variable definitions to follow.

$$\begin{aligned}
\hat{\mathbf{x}}_B = & [\sin \alpha \cos \phi + \cos \alpha \sin \phi \sin \delta] \hat{\mathbf{X}}_E \\
& + [\cos \alpha \cos \phi - \sin \alpha \sin \phi \sin \delta] \hat{\mathbf{Y}}_E \\
& + \sin \phi \cos \delta \hat{\mathbf{Z}}_E
\end{aligned} \tag{2.4}$$

$$\begin{aligned}
\hat{\mathbf{y}}_B = & [\sin \alpha \sin \phi + \cos \alpha \cos \phi \sin \delta] \hat{\mathbf{X}}_E \\
& - [\cos \alpha \sin \phi + \sin \alpha \cos \phi \sin \delta] \hat{\mathbf{Y}}_E \\
& + \cos \phi \cos \delta \hat{\mathbf{Z}}_E
\end{aligned} \tag{2.5}$$

$$\hat{\mathbf{z}}_B = \cos \alpha \cos \delta \hat{\mathbf{X}}_E + \sin \alpha \cos \delta \hat{\mathbf{Y}}_E + \sin \delta \hat{\mathbf{Z}}_E \tag{2.6}$$

In these unit vector definitions,  $\alpha$  is the right ascension of the asteroid spin pole,  $\delta$  is the declination, and  $\phi$  is the instantaneous rotation angle that marks where the asteroid is oriented within it's spin period. With these unit vectors we go on to define the body frame solar inclination,  $i_s$  which will be our proxy for spin pole obliquity. We will also define the angle  $\Omega_s$ , along with it's value at a defining epoch,  $\Omega_{s,0}$ , which is the longitude of the ascending node of the asteroid's orbit.

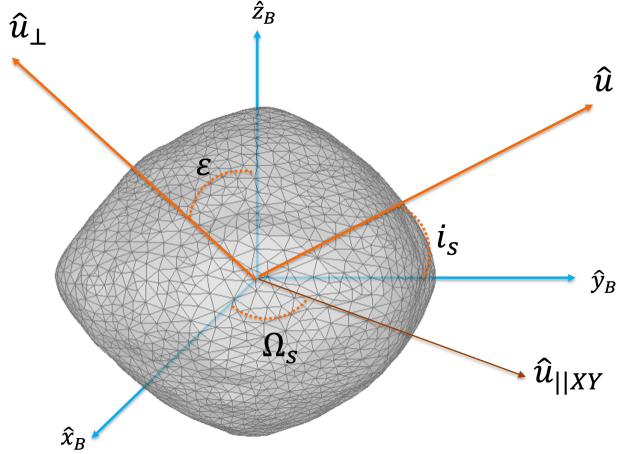


Figure 2.2: Body frame diagram which shows  $\hat{u}$ , the sun-pointing vector,  $\hat{u}_{||xy}$ , the projection of the sun-pointing vector into the body x-y plane,  $\hat{u}_\perp$ , the perpendicular vector to the sun-pointing vector, the body frame unit vectors  $\hat{x}_B$ ,  $\hat{y}_B$ , and  $\hat{z}_B$ , as well as the solar inclination angle  $i_s$ , the longitude of the ascending node  $\Omega_s$ , and the spin pole obliquity angle  $\eta$ .

### 2.3 Fourier YORP Coefficient Modeling

We apply the YORP modeling techniques derived by Scheeres in the polyhedral YORP model. This is an analytical approach to solving for rotational dynamics under YORP perturbation and provides a solution based on discretized shape geometry. The assumptions required for this model are that the body is uniformly rotating on a primary axis, thermal inertia can be parameterized as a constant lag,  $T_{lag}$ , orbital elements are evolving secularly, and shadowing is considered as an occultation calculation between all facets. For a bulk shape, the force and torque can be decomposed into Fourier coefficients based on the dual periodicity of the asteroid day and year. These coefficients are then used as an approximation for discussing the explicit force and moment, which are related linearly to first-order coefficients through orbital and geometric properties.

$$\mathbf{F} = P(R) \left[ \mathbf{A}_0 + \sum_{n=1}^{\infty} [\mathbf{A}_n \cos(n\lambda) + \mathbf{B}_n \sin(n\lambda)] \right] \quad (2.7)$$

$$\mathbf{M} = P(R) \left[ \mathbf{C}_0 + \sum_{n=1}^{\infty} [\mathbf{C}_n \cos(n\lambda) + \mathbf{D}_n \sin(n\lambda)] \right] \quad (2.8)$$

Reproduced in Eq.2.7 and Eq.2.8 is the derived force and moment expressions as Fourier decompositions into coefficients of  $n$  order. These relate as  $M_i = r_i \times F_i$  and their same-order coefficients (e.g.  $C_0$  and  $A_0$ , etc.) relate similarly.

$$\mathbf{C}_n = \sum_{i=1}^N \mathbf{r}_i \times \mathbf{A}_{n,i} \quad (2.9)$$

Equation 2.9 is the relationship between the moment coefficients and the force coefficients as they are evaluated over each facet and then summed. As we discuss the YORP coefficient  $C_0$  in later sections, note that it contains the moment relationship that considers the facet position  $r_i$ . This parameterization into coefficients allows the calculation of bulk force using discretized geometric orientation factors and simplified thermal constants. The variable  $P(R)$  is the solar pressure as a function of distance of the body from the sun,  $R$ . The iterative variable  $n$  represents the unbounded order of Fourier decomposition, and  $\lambda$  is local solar longitude, which is later used in the illumination function to integrate over solar rise and set angles ( $\lambda_r, \lambda_s$ ) for specific facets.

For approximating torque due to features, we focus on the normalized zeroth-order z-component of the moment coefficient, or  $\bar{\mathbf{C}}_{0,z}$ , which can be a function of  $\epsilon$ , the spin pole obliquity of the asteroid. This value directly correlates to spin evolution due to YORP as shown in Eq.2.10.

$$\dot{\omega} = \frac{G_1}{I_z a^2 \sqrt{1 - e^2}} \bar{\mathbf{C}}_{0,z}(\epsilon) \quad (2.10)$$

The angular acceleration is calculated from orbit parameters (semi-major axis  $a$ , eccentricity  $e$ , and obliquity  $\epsilon$ ), mass distribution ( $I_z$ ), and incident solar flux ( $G_1$ ) scaled by the orbit-averaged spin coefficient. The YORP spin coefficient is derived from a global summation of re-emitted thermal radiation over the surface area while within illumination bounds. In future work, the orbit-averaged first-order moment coefficients in the x- and y-directions ( $\bar{C}_{1,x}, \bar{C}_{1,y}, \bar{D}_{1,x}$ , and  $\bar{D}_{1,y}$ ) may be addressed as they pertain to the change in obliquity over time which leads to coupled changes in the spin. This work is focused on the spin-evolution and will only briefly mention obliquity torques due to boulders here. For further explanation of the procedures necessary to evaluate these coefficients, see Scheeres 2007, Sections 3.2 and Appendix A (Scheeres, 2007). The next section

will focus on the model design developed to calculate boulder-induced YORP torque through this polyhedral approach.

## 2.4 Comments on Orbit Averaging

The equations from Scheeres lead to results showing the secular rates of change for asteroid rotation rate and rotation pole orientation (Scheeres, 2007). In order to contextualize the YORP torque over spin and orbit for long-term evolution, these rates were averaged over the entire orbit where it is assumed that the orbit is elliptic. This means that our results can be extended for long term simulations as long as the surface distribution of boulders does not change or move, there is no cratering, and the obliquity and spin rates stay within specific bounds. If the obliquity became much different, then it would be necessary to recalculate the spin and obliquity YORP coefficients due to the altered range of sun exposure angles. If the spin rate became much higher or lower, then we approach the bounds of thermal inertia and must apply new models in order to accurately capture the physics of heat exchange of the asteroid surface materials for the new angular spin velocity. This is similarly considered in Golubov's work where the bounds of tangential YORP are such that if a boulder that is too thin or thick then it cannot display tangential YORP as well as if an asteroid spins too fast or slow it either cannot absorb heat or can be approximated as isothermal, respectively (Golubov, 2017).

## 2.5 Boulder Simulation Design

The components that make up the probability density of the spin coefficient are considered in Eq.2.11.

$$f(C_{0,z,total}) = f(C_{0,z,N}) + f(C_{0,z,B}) + f(C_{0,z,C}) + f(C_{0,z,T}) \quad (2.11)$$

This is the probability density function associated with a specific value of YORP spin coefficient. It is a convolution of several source distributions of uncertainty: normal YORP as well as boulder-induced YORP, crater YORP, and tangential YORP. Each of these sources have their own factors

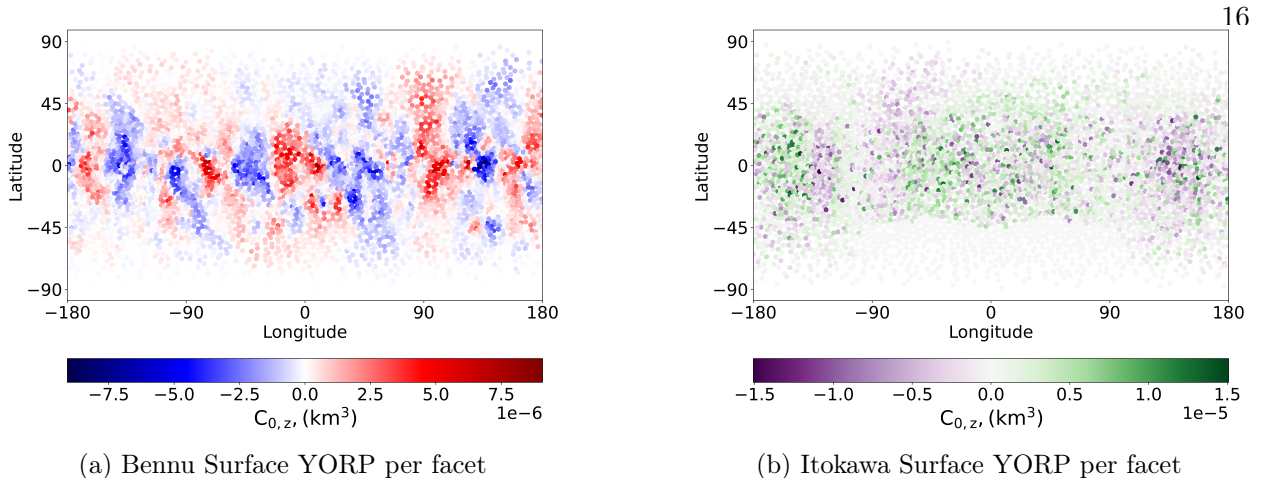


Figure 2.3: First-order YORP spin coefficient variation per facet on Bennu and Itokawa

influencing variability. In this analysis, we isolate the parameters that affect boulder-induced YORP, and discuss the associated contributions of crater YORP and tangential YORP for the entire probability density function. We also discuss the variation in normal YORP based on shape model resolution, and how to interpret different YORP spin torque results from low and high resolution models when the effect is extremely sensitive to small changes in surface normals. Delving deeper into boulder-induced YORP will then expand our capability to estimate YORP from an unresolved or poorly resolved surface that does not capture the resolution required to see the many small boulders.

### 2.5.1 Boulder Shape

In order to recreate the impact of boulders on an asteroid, we use an appropriate approximation of their shape. The nature of boulders leads to several options, but due to their variety there is no deterministic way to replicate all possible boulder shapes. The simple options are buried spheres (Golubov, Scheeres, and Krugly, 2014), walls (Golubov, 2017), or wedges (Bottke et al., 2006). Due to their directionality, wedges can direct YORP in preferential ways due to their longitudinal asymmetry. This activates YORP spin influence from a singular boulder whereas a symmetric boulder shape could not have an isolated effect on spin. In Fig.2.4, it is shown how the leading or

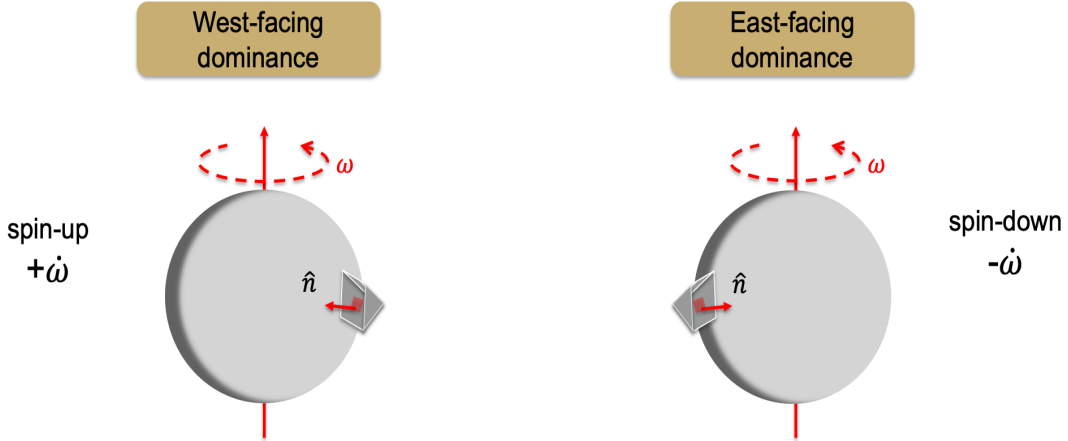


Figure 2.4: Wedge shape boulders provide asymmetry that induces YORP effect

trailing larger face can impart the dominant YORP re-radiation in either the prograde or retrograde directions which determines the acceleration of the spin axis. We assume a Lambertian-scattering surface with the added dimension of boulder shapes at the size regimes expected for their respective parent body, from 10 cm to tens of meters. The bottleneck of this simulation and many simulations attempting realism is the computational burden due to resolution of details. This dilemma prompts the use of low-resolution shape models and low-resolution boulders. We justify this low-fidelity boulder shape by the fact that boulders have no predefined shape characteristics and can exist in many configurations and orientations, especially in micro-gravity environments. This wedge then becomes the isosceles prism shown in Fig. 2.5, which is scaled linearly with the diameter chosen for the boulder during simulation.

In this model, there is variation in both YORP re-radiation torque magnitude and direction depending on the local orientation on the surface. Aligning a perpendicular face directly tangential to the spin-axis maximizes the magnitude of re-radiation torque, while the geometry of the isosceles prism (or wedge) boulder creates a balance of one larger dominant face metered by two equal-sized faces whose off-axis dampen each other and their individual spin influence is diminished by a factor of  $\sqrt{2}$ .

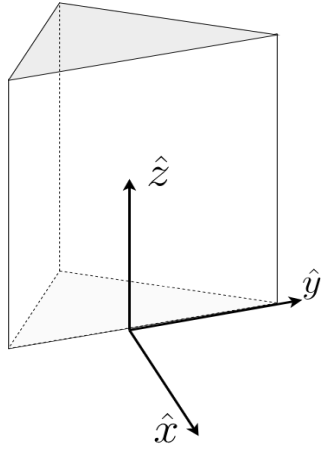


Figure 2.5: Boulder model with frame

With this shape, we see a clear relationship between the dominant flat-face orientation and magnitude and sign of YORP spin contribution as we trace the changing ratio of west to east-facing surface area. The definition of orientation here is clockwise beginning with directly west-facing in the local asteroid surface frame, as shown in Fig. 2.8. West and east here are defined by the body spin axis and direction; therefore a west-facing boulder is one where the  $\hat{x}_B$  direction is aligned with the anti-spin direction.

### 2.5.2 Bennu and Itokawa Surfaces

The asteroids selected to study YORP variability have been visited and characterized to a high level of detail. By detail, we refer to boulder counting studies which give actual numbers and sizes and locations of the discernible boulders at the time of spacecraft visitation. These asteroids are considered representative cases for their respective taxonomic classes.

The near-earth asteroid Bennu is a prime example of a nearly spherical rubble pile classified as a B-type, or a subclass of the more general C-type (chondrite) bodies that exhibit darker surfaces and are made up of some of the oldest bare materials in the Solar System (Lauretta et al., 2019). With a largest diameter of 565 m, it is easily binned into the category of small bodies for which YORP torque dominates spin evolution. Examining a low-resolution model of Bennu with the

addition of boulders on the surface can provide clues for how feature deformities can impact long-term evolution of both the surface itself and the contribution of the YORP effect to the dynamics. Secondly we examine the asteroid Itokawa, which is another member of the Apollo family of near-Earth objects. An S-type body with a spin period of 12.1 hours, this elongated ellipsoidal shape can be investigated to learn more about the difference in YORP contribution based on the lever arm potential of a feature. It has been found that a shift in center of mass of 15m could reverse the direction of YORP from spin-up to a spin-down state, further proving the sensitivity of the shape to the YORP effect (Scheeres and Mirrahimi, 2008). Findings from the simulation of these population can be compared to the measured YORP parameters for these bodies, presented in Table 2.1. While we have implemented the current simulations using a low-resolution surface models for modeling speed (5898 and 5714 facets for Bennu and Itokawa respectively), they exhibit the desired characteristics of general convexity and near-symmetry, or ellipsoidal non-convexity, which allows us to generalize the findings here for other bodies similar to either or somewhere between the two.

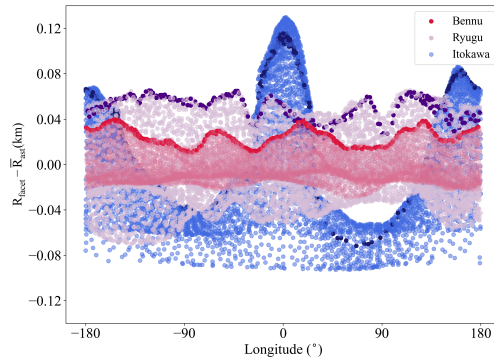


Figure 2.6: Difference of per-facet distance from body center of mass and the average radius for three asteroid shape models: Bennu, Ryugu, and Itokawa. Darker points represent equatorial facets. Itokawa exhibits the greatest variation over longitude.

The advantage of this approach is the availability of statistics on the body-specific boulder populations which could be shaped by specific material properties, cratering and regolith migration history, disaggregation or congregation during their formation events, or many other hypothetical

and unobservable factors. The assumption of these physical processes is unnecessary because we use the current surface distribution directly. When it comes to future approaches simulating boulder motion, the material behavior and likelihood of dynamical outcomes must be approximated.

A common configuration found in near-earth asteroids is the roughly axi-symmetric spheroidal shape, such as Bennu and Ryugu. This is an ideal shape for examining the dependence of YORP on the latitude distribution of additional features because the total surface area is roughly equally distributed across all latitudes and longitudes. The results shown throughout this work will represent the possible YORP values for the spin component,  $C_{0,z}(\delta_s)$ . It is important to note that a completely z-symmetric asteroid surface, such as a sphere or ellipsoid, would not experience YORP torque, but the addition of asymmetric boulders would induce a new torque by permuting the surface and adding asymmetry. In Fig.2.6, the surface contours of three mapped asteroids are shown. The difference between the facet location and the mean radii is shown in longitude radius space to highlight the spread of each surface from a symmetric distribution, which would be a straight line. The asteroid Bennu shows the least amount of variance in facet distances, while Itokawa presents the most drastic variance in differences as it follows an asymmetric ellipsoidal pattern. Each shape consists of roughly 6000 facets each, and it is interesting to note that both Bennu and Ryugu have their largest radii along the equator, while Itokawa has surface points that reach farther and fall outside of the  $2^\circ$  equatorial bound designated here.

For the base models, we start with 6,000 facet shape models of asteroids Bennu and Itokawa. We evaluate the YORP contribution to torque and obliquity of each facet based on its orientation in a  $0^\circ$  obliquity sun angle over a single day. You can see the patterns of magnitude and sign in the shape model YORP distribution in Fig. 2.3. You can see a divergence in magnitude of YORP and clustering on both of the two bodies. The base model that is used when examining the YORP

Body	Dimensions (km)	Surface Area ( $\text{km}^2$ )	Spin Rate (rad/sec)	Calc. $\dot{\omega}_{YORP}$ , ( $\text{rad}/\text{day}^2$ )	Obs. $\dot{\omega}_{YORP}$ , ( $\text{rad}/\text{day}^2$ )
Bennu	$(0.505, 0.492, 0.457) \pm 0.002$	$0.787 \pm 0.0004$	$4.0613 \times 10^{-4}$	$1.00378 \times 10^{-6}$	$3.63 \pm 0.52 \times 10^{-6}$
Itokawa	$(0.535, 0.294, 0.209) \pm 0.001$	$0.3928$	$1.4385 \times 10^{-4}$	$-2.03797 \times 10^{-5}$	$3.54 \times 10^{-8}$

Table 2.1: Bennu's Properties and Itokawa's Properties

contribution of boulders is significant as it determines how strong of a torque a feature can induce at a specific location. For reference at different points in this work, we see the observed YORP spin accelerations given in table 2.1. This is gathered from observations of Bennu, (Daly et al., 2020a) (Scheeres et al., 2016) (Hergenrother et al., 2019), and Itokawa, (Fujiwara et al., 2006) (Lowry et al., 2007) (Breiter et al., 2009). We also show the values of YORP spin acceleration calculated from our polyhedral facet YORP model. We focus on Bennu and Itokawa in order to observe the differences in boulder-induced YORP affect-potential on bodies with different levels of asymmetry and moments of inertia. Itokawa has a smaller surface area and is at a different dynamical state in its YORP timescale versus Bennu, which has a larger surface area and larger observed YORP spin acceleration. We will discuss in Sec.2.11 why the calculation and observation values of YORP torque are different and how model resolution and natural sources of YORP uncertainty can be the cause.

### **2.5.3 Boulder Population Studies on Bennu and Itokawa**

Size, location, and dominant re-radiation direction (which will be referred to as "west-pointing") all affect the YORP torque of asteroid boulders. The morphology of boulders on a rubble-pile body can indicate formation and impact history or possible thermal fracturing. These different pathways to boulder presence change the expected size range for each body. As we examine the impact of boulders on the two candidate asteroid shapes, we take information from detailed boulder counting studies for sampling expected sizes.

The spatial distribution of observed boulders is not uniform, depending on topographic valleys and gravitational potential (Jawin et al., 2020). It has also been suggested that since this distribution is highly dependent on the current state of surface evolution and regolith migration, it may be more appropriate to model distributions as fully uniform, or preferring shallower sloped regions or regions of low gravitational potential (Jawin et al., 2022).

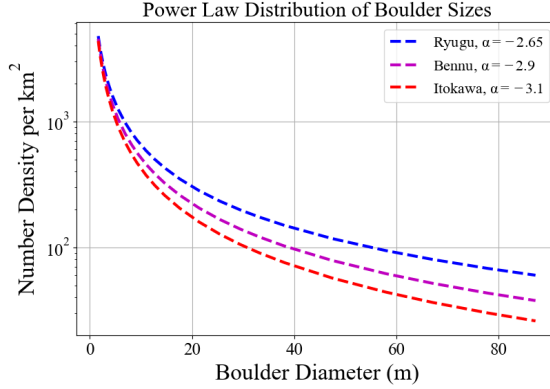


Figure 2.7: Cumulative number of boulders per square km

The sampled distributions for boulder sizes chosen in this work are shown in Fig.2.7. This is the overlaid power law size relationship for three bodies, our two candidates and Ryugu for comparison. For the instantiation of a boulder population, we impose this power law on boulders randomly sampled across the surface. In reports on Bennu's surface characteristics, it is stated that it is "dominated" by boulders larger than 1m in diameter, and additionally we find hundreds above 10 m (DellaGiustina et al., 2019).

#### 2.5.4 Applying a Simplified Thermal Model

As mentioned in Delbo et al, the Yarkovsky effect is highly dependent on the surface material's thermal inertia. However, normal YORP is not (Delbo et al., 2015). The normal YORP effect modeled here is independent of thermal inertia and dependent on the shape, self-shadowing, and surface roughness causing re-radiation dispersion. However, in the theory of tangential YORP (TYORP), the propagation of thermal energy internally through a boulder is considered and thermal inertia is a factor. This type of YORP can impart a force tangent to the surface as the thermal differential between the initially sun-incident side of a boulder becomes equilibrated with the afternoon side, emitting additional radiation always in the pro-spin direction. Tangential YORP is metered by two qualities: the spin velocity and the boulder width. If an asteroid is spinning too fast or slow, it will either experience a constant temperature at the surface or exhibit thermal equilibrium with incident radiation (replicating Rubincam's approximation), respectively. For size limits, a boulder

that is too thick will experience internal dissipation before the thermal energy can reach its opposite side. For the case where a boulder is too small or thin, the two sides can again be approximated as having instantaneous thermal equilibrium and the TYORP torque goes to zero (Golubov and Krugly, 2012).

As we consider the normal YORP (NYORP) for analyzing the addition of boulder shapes, we are primarily concerned with the geometric properties. This makes it more necessary to calculate accurate shadowing, and the thermal assumptions are simplified as a thermal lag as in Scheeres approximation. Further analysis will consider the addition of TYORP within its effective size regime, but our boulder population extends over a much broader range of radii. This will be seen in Sec. 2.11.

### 2.5.5 Polyhedral Facet YORP Evaluation

The surface-wide normal YORP torque is calculated on a facet-by-facet basis, allowing for granularity in the surface geometry and a functional approximation for absorption and remission vectors. A shape model made up of vertices, facets, and facet normal directions can be used for the entire basis of YORP calculations in all solar latitude orientations. The most intensive and necessary calculation is the visibility function, which determines where, when, and for what duration self-shadowing occurs on the body. This visibility coefficient is used to linearly scale the torque contribution from a specific facet. For this formulation, and computational efficiency, boulders here are not considered as shadow-inducing features. Force imparted on a facet element of a body is a combination of the normal and transverse elements of the YORP effect. Using terms specifically for solar irradiation, we reference the indexed force equation for the  $i$ th facet of an asteroid (Scheeres, 2007):

$$\begin{aligned} \mathbf{f}_i(\hat{\mathbf{u}}) = & -[\rho s(2\hat{\mathbf{n}}_i\hat{\mathbf{n}}_i - \mathbf{U}) + U \cdot \hat{\mathbf{u}}\hat{\mathbf{u}} \cdot \hat{\mathbf{n}}_i \\ & + a_2\hat{\mathbf{n}}_i\hat{\mathbf{n}}_i \cdot \hat{\mathbf{u}}] H_i(\hat{\mathbf{u}}) A_i, \end{aligned} \quad (2.12)$$

where it is shown that the force due to solar radiation scales linearly with the area of the facet, moderated by the illumination function  $H_i(\hat{\mathbf{u}})$ . We apply this equation to evaluate the YORP contribution of a given boulder based on its surface area and facet orientations, assuming that the entire surface and every feature of the body has 0% specularity, a reflectivity coefficient of 0.05, and exhibits ideal Lambertian scattering behaviors. Each boulder shape is analyzed for the possibility of being shadowed by surface contours, which is required in order to accurately consider the sun-rise and sun-set angles, as well as the horizon occultations that may occur throughout the day if a boulder inhabits a shadowed valley. The shape is iterated over to calculate shadowing of each facet until all of the shadowing angle bounds are found,  $\lambda_r$  and  $\lambda_s$ . The components of YORP torque are then calculated from the orientation, thermal assumptions, shadowing bounds and visibility function, and facet area. For a non-zero obliquity  $\epsilon$ , the body will wobble between the  $[-\epsilon, +\epsilon]$  bounds of the equivalent solar latitude, so the overall YORP torque from the normalized coefficient must consider the entire range of possible illumination angles.

## 2.6 Analysis of boulder impact on YORP spin torque

Bennu's collection of boulders is one representative sample of size range, placement, and global impact that we will be presenting here to examine the relationship between additional surface features and total YORP spin. It is interchangeable with any asteroid boulder population that has been characterized, or theoretical boulder distributions. We define total YORP in this context as:

$$T_{YORP} = T_{NYORP} + T_{BoYORP} \quad (2.13)$$

This is the combination of the base surface YORP, or normal YORP, and the additional effect of added boulders on the surface, boulder-induced YORP (boYORP). These are both calculated via the simple thermal model and geometric analysis of sun illumination angle and duration. It is boYORP that we are examining with statistical variability, assuming that we know our surface to the degree that the shape model is accurate. When discussing the percent impact of an individual boulder, this means the ratio of the singular boulder's normal YORP versus the total YORP of the

surface and every boulder. We also reiterate the focus on just the first-order spin torque component of YORP described by proxy with the  $C_{0,z}$  Fourier coefficient. The impact of tangential YORP experienced by boulders will be discussed in later sections.

### 2.6.1 Power Law Distribution of Boulder Size

We expect to see a probability of any size boulder within the bounds of minimum and maximum observed size to be characterized as follows.

$$p(x) \propto x^{-\alpha} \quad (2.14)$$

The power  $\alpha$  is characterized by boulder counting studies. In computation, the distribution is bounded by physical minimum size. A formula for sampling random numbers in this distribution is derived in Clauset et al. (Clauzet, Shalizi, and Newman, 2009).

$$x = x_{min}(1 - r)^{-1/(\alpha-1)}, \quad r \in \mathbf{U}(0, 1) \quad (2.15)$$

This provides a random selection of  $x$ , the boulder diameter, selected from the bounded power law distribution of sizes.

The entire boulder population sample set, spanning the range of surface area and orientation, is roughly 2.95 million individual features. This number is arrived at by generating one boulder model on each facet of a low-resolution model, which equates to 1 boulder per  $130 \text{ m}^2$  of surface area, and varying the orientation with a resolution of  $\frac{2\pi}{500}$  for all possible angles. This constitutes the full sample set  $n$ , where we then choose  $k$  number of boulders at random to form one instance of an asteroid surface distribution. The variable  $k$  is set to match the expected feature density of the body. This is done  $p$  times until statistical significance is confidently ensured, typically 500 times to give 500 possible asteroid surface instantiations per body. The power law size distribution of boulders is imposed after choosing location and orientation, which is possible to apply in post-processing due to the linear approximation of the YORP coefficient as a function of boulder surface

area. We assume that scaling a boulder in this way will not change shadowing orientations that were found and the boulders themselves are not considered to impart shadows themselves. In the imposition of these probability distributions, we are left with Gaussian equatorial bias in latitude due to the larger equatorial surface area, as well as a uniformly sampled orientation angle. The size distribution is biased towards smaller diameter boulders as one would expect from real surfaces. We can define the binomial coefficient allowing for resampling as follows:

$$\binom{n+k+1}{k} = \frac{(n+k+1)!}{k!(n+1)!}. \quad (2.16)$$

In this formulation,  $n$  is the 2.95 million initial boulder set, while  $k$  is the 5000 boulders selected to form a single possible observation of a boulder distribution. This number is astronomically large, meaning that we will see unique placement and orientation combinations in each sample set. We select this set  $p = 500$  times to gather information about the significance of boulder size, location, and orientation over many samples. We go on to explain the relationship between boulder size and its individual level of significance in the evaluation of the YORP torque over an entire asteroid.

To analyze the statistical likelihood of boulders contributing greatly to YORP, we select 500 sets of 5000 boulder models per body.

An impactful boulder can be defined as contributing in magnitude to the YORP torque felt by the asteroid past a specified threshold, defined as a percent of the asteroid YORP experienced with boulders. However, this is measured in absolute value and in large sets of boulders, one finds frequent complements in boulders contributing to both spin acceleration and spin slowing. The rapid spin-up attributed to one large west-facing boulder can be muted by many small east-facing features.

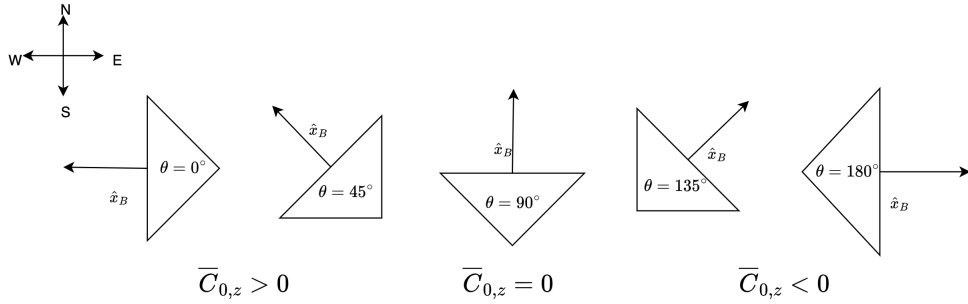


Figure 2.8: Orientation of Prism Boulder Rotating from West to East, from 0 to  $\pi$

### 2.6.2 Uniform Distribution of Boulder Location

There is no explicit dependence on latitude for a boulder to maximize its contribution to YORP torque. For many spherical-like rubble piles, the spin moment encourages movement of material to the equator. As we analyze an oblate spheroidal shape, this relationship is clear. Longer torque arms at the equator maximize the contributions of YORP torque from boulders at this latitude. From the profile of surface distances shown in Fig. 2.6, it is clear that the largest lever arms are about the equator for Bennu and Itokawa. This is not true for every shape; therefore we investigate the range of distance from spin pole for the population of impactful boulders.

We begin with a distribution of equal sized boulders over a discretized shape model. The shape has been divided into facets of roughly equal area. Due to the fitting of equal triangles over ellipsoidal or spherical shapes, there are more boulders at equatorial latitudes than polar. In further analysis, we are able to bias the selection of boulders towards either preference, and we will show how that affects the YORP torque accordingly. We chose this discretization to allow for uniform sampling over the surface area of the body, leveraging the vectorization already contained within the base shape model.

### 2.6.3 Uniform Distribution of Boulder Orientation

The distribution of torque as a factor of orientation is symmetric about zero and it can be shown that the dominant directionality of boulder re-radiation is self-limiting when enough

boulders are sampled. However, we can depend on the variation in size to maximize or minimize the orientation dominant direction in asymmetric ways for random individual boulders which is what will provide an overall YORP torque. Some locations are sloped or shadowed such that they only allow a boulder to re-radiate in one direction, but that is captured in our YORP calculations as we vary every boulder over all orientations. Boulders tangent to the spin pole are also able to exist in intermediate positions that meter the total torque effects in a sinusoidal relationship, see Fig. 2.9. Here we calculate torque directly from the spin coefficient for a single value of true anomaly.

$$T_{boYORP} = P(R)C_{0,z} \quad (2.17)$$

The torque here is related to the spin coefficient by the solar pressure at  $R$ , the distance of the body from the sun. The sign of the YORP torque relationship shown varies over three cycles for an entire rotation, which shows that, for this specific isosceles prism shape, we observe a high amount of variability. Future studies may investigate more realistic boulder shapes and the impact of variance in orientation on the YORP torque.

The equation-of-fit corresponds to the Fig. 2.9. We examine a 10 m diameter boulder placed at the equator with the underlying facet normal aligned to the body  $-\hat{x}$  axis. The torque is calculated as it rotates with angle  $x_{rot}$ . The fit is a sum of sine function with coefficients provided in table 2.2. This fit provides an r-value of 0.995 to the torque function of this specific boulder size, placement, and normalizing parameters corresponding to the asteroid Bennu's orbit.

$$\bar{T}_{fit} = a_1 \sin(b_1 x_{rot} + c_1) + a_2 \sin(b_2 x_{rot} + c_2) + \dots \quad (2.18)$$

Fit Coefficients	$a_i$	$b_i$	$c_i$
1	0.2177	2.887	1.896
2	0.06712	0.4036	0.276
3	0.09053	2.599	-0.3521
4	0.01993	5.052	-1.813
Parameters	$\phi, Wm^{-2}$	$R_{ast}, km$	$P(R), kgkm^3s^{-2}$
	1400	0.244	5.55e-3

Table 2.2: Coefficients for the sum of sines fit of boulder YORP for single boulder at equator and aligned to body  $-\hat{x}$  axis.

The dominant re-radiation orientation of a boulder is highly stochastic therefore the uncertainty due to the orientation is uniformly distributed. Our choice in shape conditions the final distribution of boulder-induced YORP with its sinusoidal function resulting from the rotation of a standing isosceles prism.

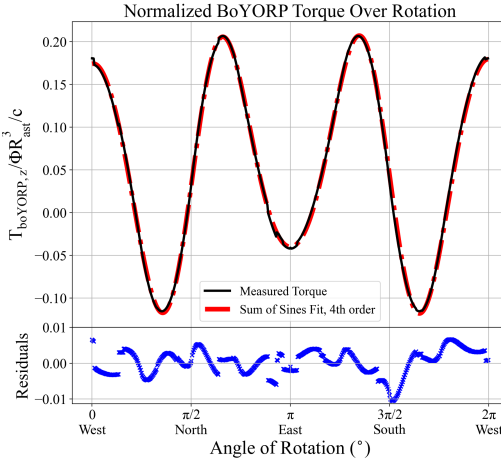


Figure 2.9: Sinusoidal relationship of boulder orientation to YORP torque. Asymmetric boulder at equator and perfectly tangent to spin pole

#### 2.6.4 Overall Uncertainty Distribution

We are uncertain about the distribution of boulder sizes on an asteroid and how far it may deviate from perfect power law behavior, but the latest observations have corroborated a power-law like distribution. We can sample this power law uniformly many times to find a variance in the typical population size. We assume uniform distribution of the small boulders, as has been reported in previous work (DellaGiustina et al., 2019). However, the local slope of the body, which is only known to the level of mapping detail, can affect the distribution of large boulders that have higher potentials. The orientation of the boulder that allows for the maximum vector of YORP torque is completely random in most natural cases. We propose biasing events and examine the outcome of this in the discussion, but for the natural statistics, we must assume that this is uniformly random. Collectively, we can characterize the uncertainty of boulder-induced YORP by these qualities: the resolution of the surface, the stochasticity in boulder sizing based on age and type, the likelihood of concentrations of boulders in valleys versus uniform spacing, and the orientation which directly affects the sign of the YORP torque.

We can model the uncertainty due to the sampling of the power law as the uncertainty in the slope parameter,  $\alpha$ . This is a measure of the steepness of the power law. The uncertainty in the slope parameter is given by the variance,  $\sigma_\alpha^2$ . Since the power law itself is analytically an asymptotic function, its variance is a function of the sample size,  $n$ , and is proposed to be asymptotically Gaussian. The maximum likelihood estimator of the slope parameter is given by the formula to follow (Clauset, Shalizi, and Newman, 2009).

$$\sigma_\alpha^2 = \frac{\alpha - 1}{n}^2 \quad (2.19)$$

The other source of uncertainty in the power law is in the minimum diameter. This can be equally described in the uncertainty of image resolution and resulting shape model resolution, so we will not consider it as a separate source of uncertainty.

Since we derived our sampled data from optical measurements, we can incorporate the uncertainty from pixel resolution. The OSIRIS-REx PolyCam instrument achieved a 0.33 m per

pixel resolution, while it's MapCam imaged down to 1.1 m per pixel. These are the sources for our boulder-counting data sets (DellaGiustina et al., 2019). As the boulder sizes are reported, we can assume that they are only accurate to 0.33 m. As for Itokawa, the mapping camera aboard Hayabusa2 was able to capture 0.7 m per pixel in their high resolution mapping campaign (Saito et al., 2006). This is the data used to report boulder size and location distributions (Michikami et al., 2008). These data sources inform the bounds on our certainty of size for each respective boulder distribution. The low-resolution shape model of Bennu that is applied in this work is a degraded surface approximation from the SPC version 20 model presented by Barnouin. Similarly, we have down-processed the SPC model of Itokawa by Gaskell (Gaskell et al., 2006). This degradation was required for computational speed of the Monte Carlo methods. We will show in future sections that this is not be concerning due to the ratio of YORP torque imposed from boulders less than 1m. However, as it pertains to uncertainty as a whole, we can only expect our model to have a surface YORP resolution comparable to a 25m facet. This resolution does change the calculations of YORP for the base shape, and we compare the low and high resolution YORP values in section 2.11. However, we use this rough approximation in order to place boulders in locations that are reasonably distributed across the body. The boulders themselves are much higher resolution and we examine their values independent of base shape resolution.

## 2.7 Bennu Results

### 2.7.1 Total Boulder Impact

Each individual global simulation case was evaluated for YORP spin contribution per boulder, which included calculating rise and set longitudes as well as shadowing bounds. These boulders were randomized in location, orientation, and size along their individual distributions. In Fig.2.10, we show the collective results from 500 randomly chosen samples.

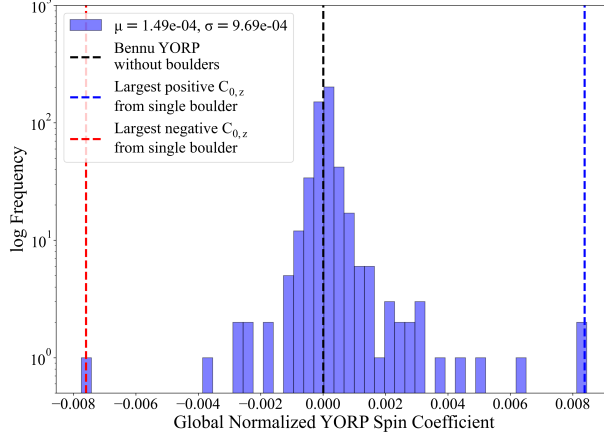
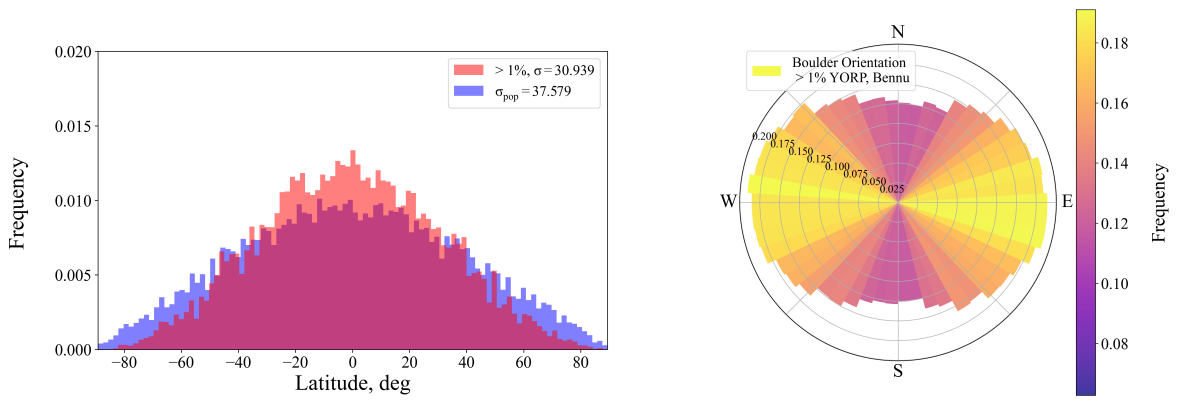


Figure 2.10: Frequency distribution of YORP with 500 random boulder populations for Bennu

The addition of boulders can affect the global YORP up to 135 times the magnitude of the original value for the asteroid Bennu. This is equivalent to the contribution of a single large well-placed boulder, contributing a YORP spin coefficient value of  $1.77 \times 10^{-4}$  compared to the Bennu base shape YORP coefficient,  $1.324 \times 10^{-6}$ . This largest magnitude spin coefficient from a single boulder is at  $-20.26^\circ$  latitude, and has a diameter of 54 m, the highest bound of the size distribution and roughly equivalent to the boulder BenBen. While the existence of these large contributors is rare in most of the global population cases, their influence is necessary to consider when quantifying the variability in YORP. Throughout the next section, we will show the trends related to boulders that are considered large contributors to YORP, at a proportion of 1% of global YORP spin torque.



(a) Latitude distribution of impactful boulders and the entire population set      (b) Frequency of boulder orientation for the impactful boulder population on Bennu

Figure 2.12: Bennu distribution comparison of normalized frequencies of boulder latitude and orientation in the > 1% YORP spin coefficient boulder population.

### 2.7.2 Large Influence Boulder Parameters

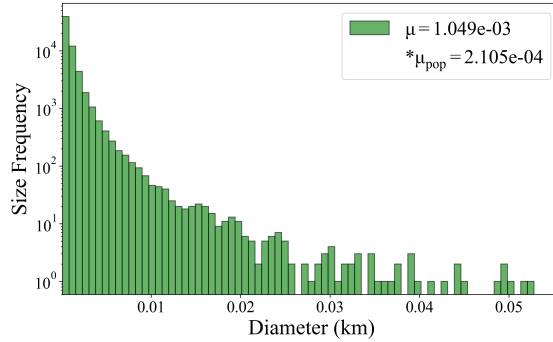


Figure 2.11: Size distribution and mean diameter of boulders where  $C_{0,z,i} > 1\%$  on Bennu

#### 2.7.2.1 Size Comparison

When analyzing the population of boulders that contribute to greater than 1% of total torque, there is a clear trend. The mean diameter of an impactful boulder, at this scale, is roughly 5 times larger than the population average, as shown in Fig. 2.11. The minimum and maximum of this subset of boulders considered impactful ranges from the population minimum, 10 cm, to the population maximum, 54 m. This subset contains just 1.2% of our large population. Note

that this encompasses 500 instances of a "Bennu" surface with boulders, consolidated together and individually compared to Bennu's base shape YORP torque plus boulders to find the subset of boulders that provide over 1% additional torque. With these results, it is expected that each instance of a boulder population could contain 60 individual boulders that change torque for the entire body more than 1% of the global value. However with further consideration of the uniform distribution of positive and negative torque boulders due to orientation, this effect may be self-damped as number of boulders increases.

#### **2.7.2.2 Location: Equatorial Trend**

The distribution of impactful boulders has a stronger density about the equator of Bennu, as shown by the standard deviation of the distributions in Fig. 2.12a. When comparing the full resampled population to the ones filtered for having greater than 1% global YORP spin influence, the standard deviation is 18% smaller. This can also be described by comparing the relative frequency at the equator. In the unfiltered population, it is expected to find a boulder at the equator with a normalized frequency of 0.01. This increases to 0.014 when examining only the boulders that contribute over 1% to YORP spin. This highlights that Bennu is oblate, seeing as the most impactful boulders congregate around the equatorial region. The average boulder distance from the z-axis on Bennu is 127 m, compared to its largest equatorial radius of 282 m, which aligns with expectations for oblate spheroid geometry.

#### **2.7.2.3 Orientation Bias: West or East**

Once more, filtering for large YORP contributors while considering another influential parameter, we clearly see in our oval-shaped direction distribution that there is a higher frequency of boulders pointing more west or more east, in spin-delta maximizing orientations. This is emphasized by our selection of a boulder geometry which can maximize torque in preferential orientations: specifically, the alignment of the largest flat face pointing direction with the spin pole tangent.

The boulders that point north or south, at angles  $\pm\pi/2$  away from local west, are depleted

in this subset. In the coming sections we show the impact of biasing boulders towards the west at greater than uniformly random proportions. This will show the global impact of orientation dominance that may arise from biasing events such as spin-related weathering or longitudinal ridge formation.

## 2.8 Itokawa Results

### 2.8.1 Total Boulder Impact

When examining the variation in Itokawa surface simulations with boulders added, a smaller extent of variability is found versus our previous model. Shown in Fig.2.13, the strongest variation from Itokawa's natural calculated YORP value is 12 times larger, where Itokawa's base normalized coefficient is  $-0.0036$  and the largest magnitude case of difference is  $-0.0423$ . The variability in this data set arises from the distributions applied to the predetermined boulder factors of size, orientation, and location.

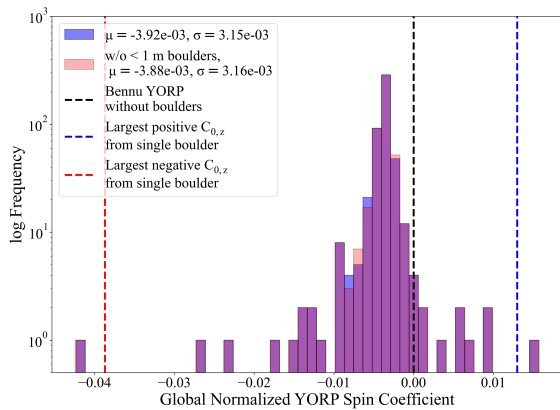


Figure 2.13: Frequency distribution of total boulder YORP spin coefficients for Itokawa

## 2.8.2 Large Influence Boulder Parameters

### 2.8.2.1 Size Comparison

Itokawa has a population of boulders similar to Bennu in this simulation, 10 cm to 50 m and a size power law coefficient of 3.05. In Fig.2.14 is the distribution of boulders that impact Itokawa's YORP spin with more than a 1% contribution, compared by spin coefficient. The difference in mean size between the resampled data and the filtered impactful data is 16 times larger than the population mean, compared to the 500% seen for Bennu. The number of boulders that provide more than 1% of magnitude compared to the global YORP is 29.3% of the 500 possible sets of 5000 boulders simulated. Note again that we are comparing magnitudes and not signs when considering this data, in order to illustrate the strength of YORP imparted by a single feature in the positive or negative direction. As was discussed in Sec. 2.6, the sign of YORP is evenly distributed as the orientation changes and therefore a dampening of this effect is seen when considering a large number of boulders in a population.

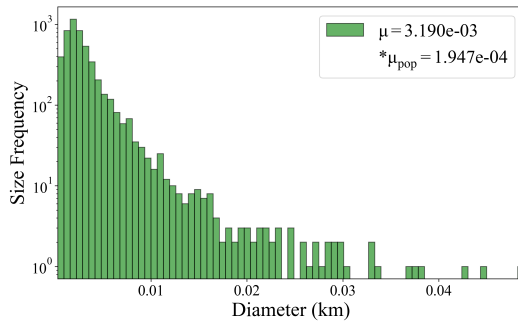


Figure 2.14: Size distribution and mean diameter of boulders where  $C_{0,z,i} > 1\%$  for Itokawa

### 2.8.2.2 Location: Sub-30 Degree Latitude Preference

We see in Fig.2.15a, there is a natural tendency for boulders with longer lever arms, such as ones found at the far lengths along the equator, to have a larger YORP spin coefficient. The standard deviation of the latitude distribution of boulders that contribute more than 1% to global

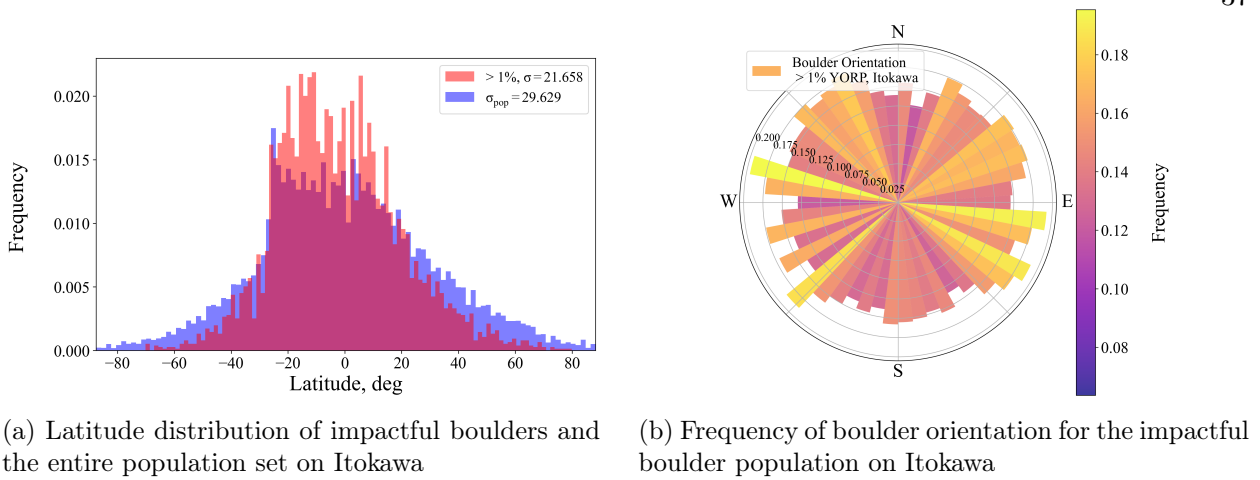


Figure 2.15: Itokawa distribution comparison of normalized frequencies of boulder latitude and orientation in the  $> 1\%$  YORP spin coefficient boulder population.

YORP is 27% smaller than the full population. This is a more dramatic relationship than seen in the Bennu influential latitude distribution. The frequency of boulder latitude between  $\pm 30^\circ$  on Itokawa is at times double the population distribution frequency. Itokawa has longer torque arms at the equator relative to non-equatorial latitudes and this feature is pronounced in the ellipsoid versus a spheroidal shape.

### 2.8.2.3 Orientation Bias: No Pattern

The impact of orientation changes on Itokawa have a much more damped effect versus the spheroidal shape of Bennu. There is a larger collection of impactful boulders in the directly east direction, but at a much lower variation of 7% difference from the full population of uniformly distributed boulders. It is a barely perceptible difference in the full distribution seen in Fig. 2.15. Boulders pointing east had a stronger bias than any pointing directly west, but overall the variation from a uniform distribution is small.

The largest factor for defining an impactful boulder in Itokawa is the torque arm, which in this shape is related to latitude. As seen in Fig. 2.3, Itokawa has its largest positive and negative torque coefficients on the far regions of the head and posterior lobes. At these locations, a slight

tilt in either the westerly or easterly directions can be magnified and therefore smaller boulders here will have a larger contribution to global YORP. There is more investigation to be done on the relationship of YORP torque and surface evolution as we see bodies like Bennu that have reached a relatively axi-symmetric spherical stable shape and attitude, while bodies like the contact binary Itokawa could be evolving away from or towards a more symmetric shape as the lobes contribute to YORP spin-down.

## 2.9 Sensitivity Analysis

We find that for each body, the effective size required to contribute just 1% to the global YORP acceleration can be relatively small and only bounded by the minimum of the possible distribution. The contribution ratio is also altered by properties that can increase the stochasticity of YORP emission and even alter the sign of torque. By producing many models of boulder populations, we have provided a significant sample size in order to address the variance in the YORP effect due to boulders. Now we will show how sensitive our global YORP torque calculations are to limited size bounds, enforced directionality, and simulated latitude restrictions. This is to find how influential each component can be for our simulation set of boulders.

### 2.9.1 Size Thresholding

The natural size distribution of boulders on a surface follows a steep power law. This entails that smaller boulders are much, much more likely to be found on a surface versus larger boulders. This fact was not necessary to prove, as we used observations from several rubble-pile asteroids as a basis for sampling. In this analysis, we focus on Bennu's boulder population as representative for both cases to detail the impact ratio of each boulder size on the global YORP torque. Further analysis is performed to compare boulder sensitivity on both bodies for orientation and location biases.

When estimating YORP based on rough shapes, smaller boulders will not be observed or captured in the resolution of the model. In our simulation, the smallest boulder can be 10 cm

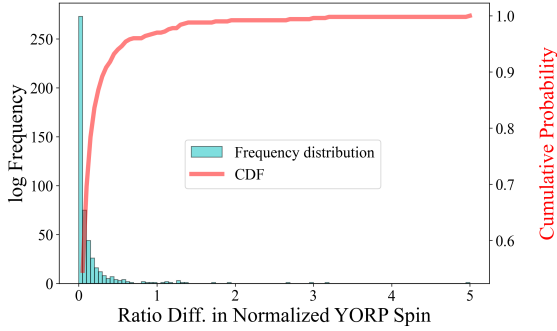


Figure 2.16: Change in Bennu's global YORP spin coefficient with boulders, shown in Fig.2.12, when removing boulders  $< 1\text{m}$ , roughly 99% of original population.

in diameter, but in most studies, boulders around several meters are analyzed as they are easily observable and characterized. Here we compare the contribution of boulders by size range, binned in ranges of below 50 cm, between 50 cm and 1 m, between 1 m and 10 m, and above 10 m. This captures the size ranges that are both heavily sampled from our power law as well as the most obvious and impactful boulders on rubble-pile surfaces for bodies less than 1 km in diameter.

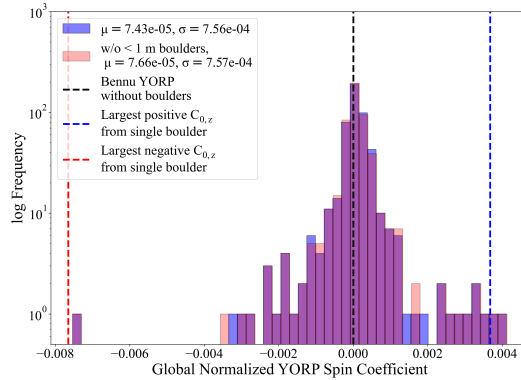


Figure 2.17: Overlaid distribution of normalized YORP with and without 1 m boulders

When the boulders less than 1 m in diameter are removed from the summation, we do not see a very large shift in the average global YORP. The distribution in Fig.2.16 shows a much higher frequency of changing YORP spin less than 50% of the original value. This distribution is skewed by the large contributing boulders discussed in section 2.7. However, the cumulative distribution function shows an extremely steep increase below 100% and continues to act asymptotically as we

approach the single case where normalized YORP changes by 5 times the original value with the elimination of boulders less than 1m.

We capture the same population statistics when only 1.11% of our original simulated features are considered, with the size bins and their associated YORP distributions given in Fig.2.18. The result of filtering out boulders less than 1 m in diameter is shown in Fig. 2.17. The mean of the distribution changes by 3%. and standard deviation varies by 0.13%. This is a powerful observation that can limit our further simulations to boulders of significant size and contributions instead of the full realistic size regime. This analysis is focusing on the variation in global YORP spin as it is totaled, versus the previous sections which looked at individual contributors by magnitude. We use a different metric for consideration of impact when considering the global YORP delta versus the individual boulder YORP.

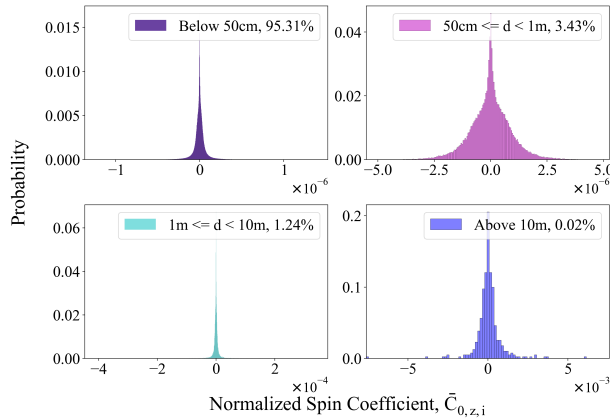


Figure 2.18: Boulder spin coefficients for Bennu, separated by size bins. Percentages represent the proportion of boulders in each bin to the size of the sample population.

There are large boulders seen on other asteroids that are possibly earlier on in their evolution. The boulder Dhol on the limb of the secondary of the Didymos system is estimated to be 16 m in diameter (Daly et al., 2024) (Pajola et al., 2024). When compared to the 160 m diameter of the secondary itself, this is the same size fraction as the 54 m boulder seen on Bennu. Due to the deformation observed on Dimorphos, we expect that rubble-pile bodies with these mechanical

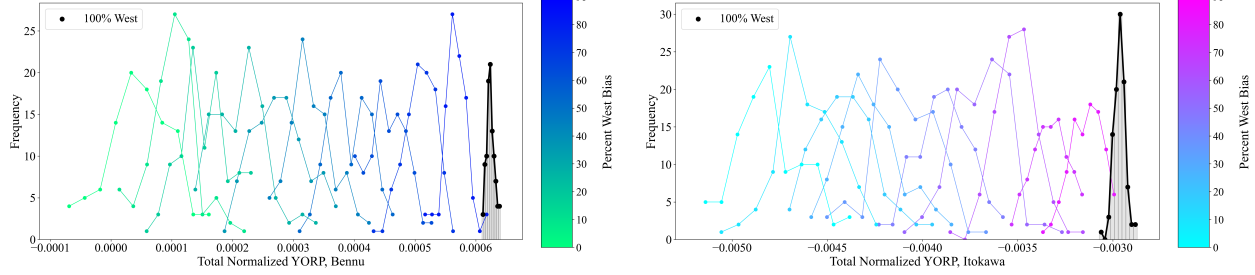


Figure 2.19: Change in global YORP spin coefficient when enforcing a percentage of boulders with a westward orientation bias. Each profile is a histogram of global YORP spin coefficients. The black histogram represents the 100% west bias for all boulders

properties will have young and dynamic surfaces (Raducan et al., 2024). Just one boulder of 10% of the overall body diameter can change YORP more than 100 times over or reverse its sign; however most of our simulated cases show a change in YORP of 10% or less with the large population of mid-range boulders above 1 m making the bulk of the difference. As an asteroid evolves, it is less likely that the largest boulders will move and instead they may fragment and change their dominant orientation faces. We can also expect them to be buried if found at low latitudes or slope downhill, and conversely they may be excavated if found at high latitudes where material is flowing away from them. We discuss the implications of these circumstances in the coming sections.

### 2.9.2 Orientation Biases: West Preference

In surface observations of Bennu, preferential orientation of boulders was observed due to surface slope, where boulders aligned their long axes to the downhill direction of the local mass flow (Tang et al., 2023). Here we simulate varying degrees of orientation bias relative to local cardinal direction, ranging from 10% to 100% west-facing preference. This is done by evenly distributing boulders on every facet and enforcing a constant size of 1 m in diameter for each boulder, but choosing random individuals at the predetermined ratio to be pointing within 0.05 radians of directly west. We see that the average global YORP changes when 100 samples of boulder populations are simulated with the orientation bias enforced at each percentage level. The zero bias case is representative of a uniformly distributed random set of orientations for each boulder on the surface, and

is therefore considered the control.

In calculating the averages associated with Fig.2.20, we see that the mean global YORP for both Bennu and Itokawa trends positive as boulders are biased to point westward. Bennu begins with a positive global YORP value and increases shallowly as west bias increases, whereas Itokawa begins much more negative and increases steeper with increasing west-pointing bias. A similar analysis can be done with eastward bias showing an increasingly negative contribution to boulder-induced YORP as more boulders align the dominant radiative face towards the spin direction. We also see a shallower increase in Itokawa's total boulder-induced YORP, showing a higher inertia to westward orientation preference of boulders. This is due to the lower percentage of equatorial surface area on this body as compared to Bennu, where most facet normals align more strongly with the equatorial plane versus the z-axis.

Another possibility for bias is that of one large boulder shifting in the dominant re-radiation direction on the surface, such as in the case of mass flow alignment or fragmenting due to heat cycling. This will also change the global YORP torque in the direction of bias. As shown in section 2.7, just 1.6% (or about 96 out of 6000) of the largest members of our base population are needed to model boulder YORP contributions and a single large boulder can be the driver of the most extreme edge cases. A change in the magnitude or sign of the torque vector of the largest boulders will have a proportionally large effect on the global spin. A large boulder is also unlikely to move, and will act as a static rudder of sorts, continuously changing YORP in a secular direction until it is removed, buried, or permanently shadowed.

### **2.9.3 Location Bias: Polar Migration**

The very old geological history of Bennu has been referenced to explain the variation in material composition as well as the distribution of boulders we see today. As Bennu migrated to its current orbit, material migrated towards areas of high gravitational potential. This has caused the Roche lobe feature at the equator (Scheeres et al., 2019). To examine the conditions that caused this conglomeration of material, we bias boulder placement outside of the Roche lobe,

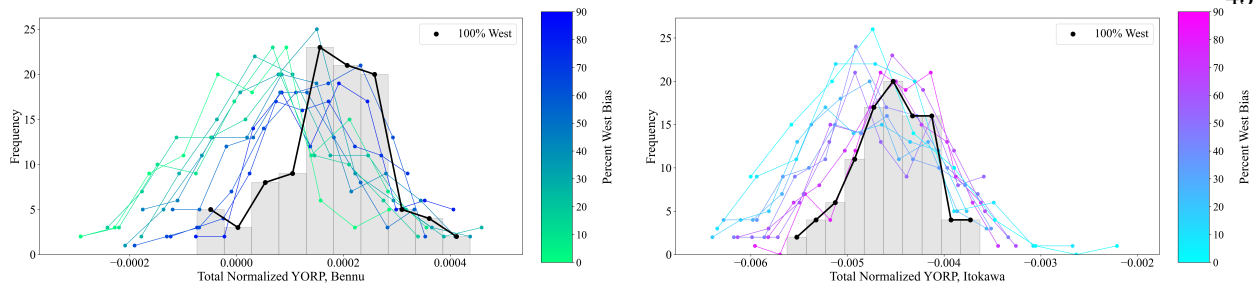


Figure 2.20: Change in asteroid global YORP spin coefficients when removing boulders outside of  $\pm 30^\circ$  latitude, varying the percentage until 100% are outside of the the bounds equivalent to a liberal cushion about Bennu’s Roche lobe

or above and below  $\pm 30$  degrees latitude. This could also simulate boulders migrating to this area during an era of YORP spin-down, or the case of leftover boulders after larger ones have left the body through migration to the equator and reached escape velocity. The investigation of this configuration of boulders outside of the equatorial regions provides insight to how boulder-induced YORP changes as the surface redistributes material over time and eventually becomes what we see today. Future work will examine the gathering of boulders in craters or piling against larger gravitationally downhill features.

We simulated 100 cases of boulders on each shape model, with the number equal to facet resolution of the shape, with a varying percentage of bias in the location, similar to the process of inducing orientation bias. The random selection of orientation was kept consistently uniform while the size selection was standardized at 1 m in diameter. The distribution outlines in the top plot of Fig.2.20, in gradient colors of green to blue up to the 100% polar bias case in black, have small variations in boulder-induced YORP as the bias increases. We see that the removal of boulders from the polar regions of Bennu moves the average in the positive direction and the lower bound of each distribution increases as the bias gets larger, but not as dramatically or linearly as seen with orientation bias.

When performing the same analysis on Itokawa, we see a similar shift of the data mean in the positive direction. The lower and upper bounds of the 0% bias case are the widest of any histogram shown, and the 100% bias is the most constricted. One interesting feature of these results is that

the distribution of 100% polar bias on Itokawa is entirely negative boulder-induced YORP values.

If we observed a large boulder closer to the pole of an asteroid, such as Bennu's large southern hemisphere feature, the implications on YORP evolution would be affected by induced prevention of material moving towards the equator by the damming effect this large feature will have on smaller, more dynamic particles on the surface. As material moves in mass flows, more regolith and small boulders will aggregate against the uphill of the large feature, increasing it's size and YORP contribution as well. This can serve to amplify the original YORP contribution of the large boulder until the local potential is overcome or the feature is somehow removed. Our bias analysis examines the case of one feature causing the collection of many, therefore increasing the presence of boulders in polar regions which would increase the YORP torque if the trend seen on Bennu and Itokawa follows for other pro-grade rotators in this size regime. Similarly, an large equatorial feature would be continuously buried by smaller particles moving downhill, and the YORP torque would be reduced as the feature is covered and smoothed. In these cases, as seen with increasing polar bias, we expect that YORP spin torque evolution will occur incrementally and predictably as the surface evolves unless a catastrophic disruption were to occur.

## **2.10 Efficiency of Boulder Shape**

The shape chosen to represent a boulder in this work is the wedge of a cube split down the diagonal on one face. This means that there are three faces perpendicular to the asteroid surface, two of which are equal sized and one is longer.

## **2.11 Total YORP Discussion**

### **2.11.1 Crater YORP**

Craters were observed on the asteroid Bennu with detail due to the hovering image survey carried out by the OSIRIS-REx mission (Walsh et al., 2019), the same survey from which our boulder population statistics were derived. Studying the crater population has opened investigations about

the surface and its age. Specifically, studying craters informs how a proposed armoring factor has an influence on the presence of specific sizes of craters and allows for better characterization of resurfacing processes on rubble-pile bodies (Bierhaus et al., 2022). The population was characterized and reported following shape modeling efforts (Daly et al., 2020b). The depth-to-diameter ratios are reported for 108 impact craters larger than 10 m in diameter. We present here the calculated YORP contribution from the crater population on Bennu, according to Zhou et al.’s formulation. Their findings have shown that craters with depth-to-diameter ratios less than 0.05 can be ignored. For the most realistic case of surface roughness, craters can reduce total YORP torque by tens of percents (Zhou and Michel, 2023).

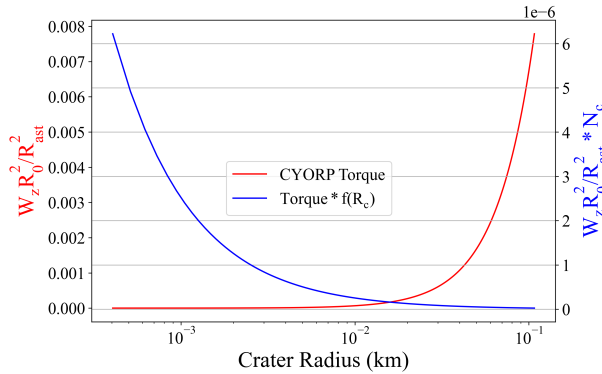


Figure 2.21: Normalized CYORP Contribution scaled by crater diameter frequency

For the size regime of craters on the asteroid Bennu, which stretches from 8 cm to over 200 m in diameter, we see an exponential relationship with how much a crater of a particular radius will contribute to the global CYORP sum. This data is provided by detailed analysis of Bennu surface maps which characterized the craters in order to age the surface material (Bierhaus et al., 2022). For comparison in blue, the torque is scaled by the prevalence of that size crater on the surface for an arbitrary body. We see that contributions of larger craters are tapered due to their lower frequency, while smaller craters could realistically dominate or negate the YORP forces of one large crater. This follows our power law distribution of boulder size and frequency. However, the difference in magnitude between the two y-axes shows that the limitations of the crater diameter

power law reduce total CYORP torque by a factor of roughly one thousand. CYORP differs from normal YORP because it considers the thermal reabsorption that is specifically induced by a concave structure inclusive of self-shadowing and self-heating. For the spin-inducing component, we show a plot of magnitude of torque related to crater diameter, though there are other position factors that can make the torque either pro- or anti-spin, which varies the sign of the torque.

According to semi-analytical models, a crater in this capacity is defined as the difference between flat ground and the depression of a crater. At specific sizes above the shape model resolution, these craters would be captured in the normal YORP calculation when this analysis is done as a sum of polyhedral facets. The same is true for very large boulders, and this will be discussed in the next section. Crater YORP is important to include in full discussions of the YORP effect of highly detailed surfaces and we go on to compare to other sources of YORP that have been shown.

### 2.11.2 Tangential YORP

Tangential YORP is the by-product of the thermal inertia of protruding asteroid surface material. As heat is absorbed over a day, it is transferred through the volume at a rate determined by its mineral properties and geometry, summarized as the heat conductivity length,  $L_{cond}$ . This length is determined from analysis shown by Golubov (Golubov and Krugly, 2012).

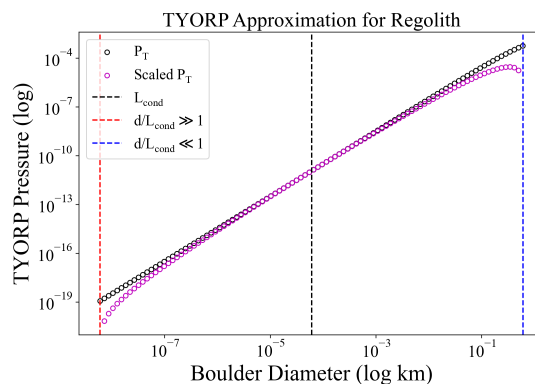


Figure 2.22: Incorporating the assumption of smooth transitions below and above the ideal thermal inertia length,  $L_{cond}$  with a logarithmic scale factor

Varying types of material have different thermal inertias, and asteroids can have clustered features with similar thermal properties such as Bennu's concentration of high thermal inertia regolith at the Roche lobe (Rozitis et al., 2020). Tangential YORP is negligible or non-existent if the boulder diameter is so thick that energy is not propagated entirely through. Conversely, there is no force if the diameter is small enough to approximate instantaneous heat transfer and equal temperatures on each opposing face. With equal faces opposing, the YORP spin torque is averaged to zero.

Here in Fig.2.22, we show the magnitude of dimensionless TYORP pressure as it relates to boulder size when approximated as a flat wall. In this calculation, the wall thickness is equivalent to the boulder diameter. We have also scaled the analytical form of TYORP to consider the declination in strength at the bounds far away from the heat conductivity length. This logarithmic scale factor considers  $d/L_{cond} = 100$  as an upper bound, and 1/100 similarly as the lower bound for effectiveness. Tangential YORP is known to impart positive rotational acceleration in most cases. What is presented here is a large variability in boulder-induced YORP. If any body has features that cause a preferentially negative normal YORP and boulder-induced torque and that same material falls within the bounds of thermal inertia necessary to induce TYORP, than the resultant spin could be non-accelerating. Golubov notes this may be the reason for a lack of observed YORP deceleration from the asteroid Itokawa, despite normal YORP calculations providing a small negative torque. With the additional consideration of boulders and craters, the sources of uncertainty grow and estimates of YORP must encapsulate this variability (Golubov and Krugly, 2012).

In comparing all the current models for YORP torque, we apply the obliquity-dependent TYORP equations from Ševeček which is also expanded upon in further works (Ševeček et al., 2016) (Golubov and Scheeres, 2019). We use the expression in Eq.2.20 which considers obliquity ( $\epsilon$ ), number of boulders ( $n_0$ ), the sign of angular velocity ( $sgn(\omega)$ ), and a boulder size power index

of 3.

$$T_{z,TYORP} = 4.5 \frac{\Phi R^3}{c} n_0 \mu \exp \left( -\frac{(ln(\theta) - ln(\theta_0))^2}{\nu^2} \right) \times (1 + \cos^2 \epsilon) sgn(\omega) \quad (2.20)$$

### 2.11.3 Overall YORP Comparison

The aim of this work is to characterize sources of YORP torque from small features that border the size limits of regolith as well as the maximal surface resolution obtainable from ground observations. By expanding the YORP torque model in this way, it could be possible to make better estimates of YORP from rough radar shape models. We have varying levels of shape model resolution for the asteroid Bennu and each one comes with a different YORP torque evaluation based purely on the geometry of the surface and its orbit. Here with Fig. 2.23 we see the relative strength of different YORP torque sources and their uncertainties when applied to the case of Bennu. The normal YORP in red corresponds to our analysis of the shape without boulders, and the BoYORP mean and upper bound (in yellow) correspond to the results of our statistical study,  $\mu + 1\sigma$  to show variation in log space. The crater YORP model, shown in blue, is reported from Zhou and shows the variation of depth to diameter ratios that one would expect to be the upper and lower bounds of the largest crater on Bennu ( $h/D_0 = 0.1 \pm 0.03$ ) (Zhou et al., 2022) (Daly et al., 2020b). We also report the observed YORP values from HST and their error bounds in green (Nolan et al., 2019).

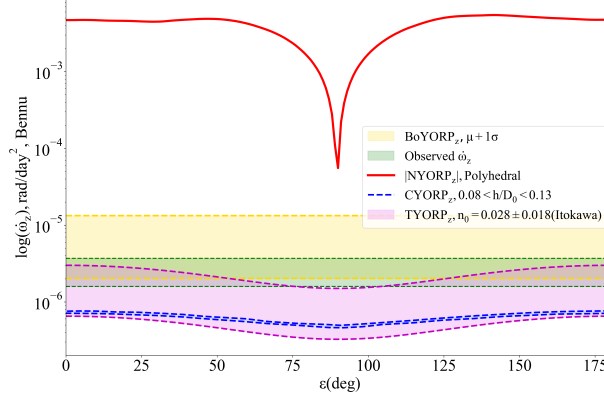


Figure 2.23: Comparison of analytical YORP spin components for Bennu as a function of obliquity

Tangential YORP in this formulation comes from Golubov and shows that, even without enforcing the size boundaries of effectiveness, we still see a small relative contribution from this effect (Golubov, 2017). The bounds reported here correspond to the error in the variable  $n_0$ , an approximation for surface area covered by boulders. The values reported for  $n_0$  of Itokawa are  $0.028 \pm 0.018$  and contain the variability reported in violet in our figure. Here we make the assumption that Bennu and Itokawa have similar boulder populations and therefore the same error in  $n_0$  can be applied to Bennu. We also assume that the mean boulder YORP value reported at zero degree obliquity is applicable at all obliquities if not larger. Boulder-induced YORP is the strongest influence in this comparison and while here we show the mean value of spin acceleration from our simulations, the largest cases are 2 to 3 orders of magnitude larger than the BoYORP mean for Bennu. In the log scale, we only represent the positive contribution of boulder-induced YORP, but we recognize that there is an equal possibility that we contribute a strong negative acceleration to the spin of the asteroid. This is not true for the models of crater and tangential YORP shown, which are analytically positive at all obliquities.

When considering the sources of uncertainty from each model of YORP spin torque, we can compare them in magnitude and combine them to report a total YORP uncertainty including the variability due to boulders. Included is the uncertainty due to shape model resolution, reported as the difference between the YORP torque calculated from a high-fidelity model and one calculated

from the 6k facet degraded Bennu shape model. We follow a root-square-sum procedure.

$$\sigma_{total} = \sqrt{\sigma_{BoYORP}^2 + \sigma_{TYORP}^2 + \sigma_{CYORP}^2 + \sigma_{NYORP}^2} \quad (2.21)$$

The error reported here is taken from the models shown in Fig.2.23, and the normal YORP error is extrapolated from the difference in YORP results in high and low resolution shape models of Bennu. This represents the variability due to the base shape. Boulder YORP error is the standard deviation from Fig.2.10. Tangential YORP and crater YORP have upper and lower limits with an associated standard error within that variability. The total YORP uncertainty is  $1.394 \times 10^{-5}$  deg/day<sup>2</sup>.

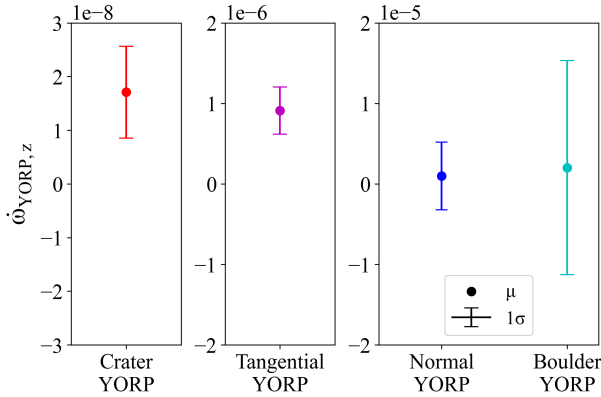


Figure 2.24: Comparison of mean and standard deviation from several YORP models

## 2.12 Application to YORP Estimates

As we consider tangential and feature YORPs from craters and boulders, this provides additional sources that could match ground estimates to actual in-situ measurements. For example, comparing pre-mission estimates of Bennu's YORP torque to the actual measurements from the OSIRIS-REx mission, we can map discrepancies due to resolution changes and unobserved features (Nolan et al., 2019). Another example is the lack of an observation of YORP from Itokawa. After mapping the surface, evaluation of the detailed model shows an expected YORP of  $-2.5$  to  $-4.5 \times 10^{-17}$  rad/s<sup>2</sup> from the geometry alone (Scheeres et al., 2007). The YORP acceleration has

also been calculated for Ryugu shape models with considerable uncertainty between 20 variations of the Hayabusa2 map results,  $(-6.3 \text{ to } -0.42) \times 10^{-6} \text{ deg/day}^2$  (Kanamaru et al., 2021). Their analysis varied the shape modeling method, stereophotoclinometry (SPC) or Structure-from-Motion (SFM), as well as the set of source images by day. Their requirement for shape model resolution was 49,000 facets.

The standard error for Ryugu's YORP acceleration would be  $1.47 \times 10^{-6} \text{ deg/day}^2$ , which is 10 times smaller than the total YORP uncertainty we derived from the combination of models for Bennu. The bodies are not extremely different in size or in the YORP observed or estimated for them. The uncertainty for Ryugu was derived from variation in shape model resolution, however, our uncertainty incorporated the expected contributions from boulders, craters, and tangential YORP. This shows the need for further consideration of the YORP impact from expected features and roughness and more complex thermal radiative patterns.

## 2.13 Boulder Motion

When the dynamics change, there can be new forces at the surface that induce boulder motion. This can be sliding, rolling, or escape that are all side effects of spin acceleration. Here we will show the difference in YORP spin torque contribution between a boulder at a single constant longitude, but varying between +45, 0, and -45 degrees in latitude. These are the same size (0.1m diameter) and orientation (directly west). The difference in torque between these boulders is equivalent to the change in dynamics due to a boulder moving from its original location to a new one. In Fig. 2.25, we show the YORP spin acceleration values for boulders at varying latitudes between -90 and 90 degrees, or south to north pole, that are all constrained within -173 and -178 degrees in longitude. Note that the distribution shows that boulders, all facing 100% west with their dominant face, can vary between negative and positive YORP spin acceleration even on the same hemisphere. The boulders closer to the equator contribute the most spin torque due to the longer lever arm length from the central spin pole. However, slight variations in the tilt of the base facet can cause these swaps from positive to negative on boulders close to each other.

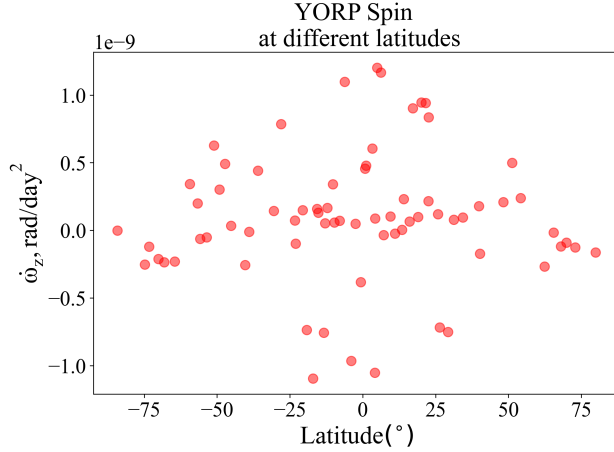


Figure 2.25: Differing amounts of YORP spin acceleration for boulders within 5 degrees in longitude but varying latitudes

We show the delta distribution of these boulders, in Fig.2.26, by taking the difference of YORP spin from each boulder compared to it's closest north neighbor. The change in latitude varies by boulder comparison, and we show the resultant change in YORP acceleration contributions based on this latitude change. Note that the maximum delta in longitude is just 5 degrees. There is no relationship between larger latitude change and YORP acceleration change. The motion represented by  $0 - 2^\circ$  of latitude change is the most common and shows the largest distribution, positive and negative, of YORP acceleration change.

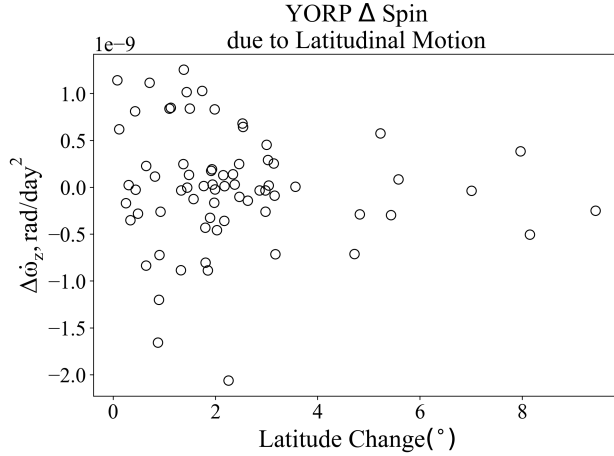


Figure 2.26: The change in YORP spin acceleration from boulder motion with the latitude degree change shown on the x-axis

This data shows how much YORP can change from the same size, same orientation, and same shape of boulder being assessed at different locations, mainly varying in latitude which is the larger driver of YORP spin acceleration change due to the lever arm length variation. The largest YORP spin acceleration delta is  $1.6828 \times 10^{-9}$ , which is equivalent to a doubling rate for Bennu of 76 million years from a single boulder delta. If extrapolated to the case where 1% of the boulders on the surface, now sized at 1m, were all to increase in YORP acceleration at this rate, then the doubling time due to just these boulders is now 153,000 years. In the Bennu lifetime, this is a short period for accelerating from a 4.3 hour period to 2.15 hour period. In the next chapter, we will show the rotational deformation speeds for these asteroids and compare these values to what we have found here.

## 2.14 Summary of Spin Evolution Findings

Boulder-induced YORP is the consideration of larger-scale surface roughness which can still be modeled through facet geometry therefore is not captured in regolith roughness approximations. We have shown that compared to the magnitude of other analytical models of YORP, it is a significant contributor to final magnitude and uncertainty. We can use this characterization of YORP from

boulders to inform future estimates of measured YORP versus actual shape, which aims to clarify the sources of uncertainty or bias in our current YORP estimates. Simulating realistic populations of boulders provides an applicable way to tie together observation and modeling of YORP in a way that purely analytical models have not.

- The mean boulder addition to YORP-induced spin acceleration on Bennu was  $.1039 \pm 1.329 \times 10^{-5}$  deg/day<sup>2</sup>, and  $-2.129 \pm 1.717 \times 10^{-5}$  deg/day<sup>2</sup> for Itokawa.
- Boulders contributing more than 1% to global YORP on Bennu were 18% more likely to be found within 30 deg. of the equator and 29% more likely to point west or east. Those values for Itokawa were found to be 9% and 3%, respectively.
- The average size of boulders that contribute more than 1% to Bennu's global YORP spin acceleration was 4x the full population mean, and 15x larger for Itokawa.
- The mean of total global YORP spin increased an average of  $7.913 \pm 0.574 \times 10^{-7}$  deg/day<sup>2</sup> with each 10% increase in westward orientation bias for Bennu, and  $1.029 \pm 0.110 \times 10^{-6}$  deg/day<sup>2</sup> for Itokawa.
- In the case of biasing boulders location towards the polar regions (outside of  $\pm 30^\circ$  latitude), the global YORP spin increased an average of  $2.262 \pm 3.052 \times 10^{-7}$  deg/day<sup>2</sup> with each 10% increase in polar bias on Bennu, and  $1.471 \pm 3.973 \times 10^{-7}$  deg/day<sup>2</sup> for Itokawa.
- The change in average of the global YORP spin acceleration when boulders < 1 m were removed was 1.11% and 1.36% for Bennu and Itokawa, respectively.

The TYORP effect is considered for it's part in the larger YORP model, but acknowledged for it's bounded contributions. We have analyzed the relationship between meaningful and observable aspects of boulders, such as dominant orientation, placement, and size, and the amount of re-radiative thermal torquing which will provide possible avenues for explaining specific routes in YORP evolution over time. In discovering the statistical contributions of varying sizes of boulders

on two asteroid models, we have shown that boulders less than 1m make up 90% of the YORP estimate despite being 1% of the total population of boulders. Capturing this level of detail in such a small portion of the population allows for further work to continue analyzing the dynamical impact of the presence and motion of larger, more observable boulder candidates.

We have compared the relative strength between the CYORP model and the contribution due to additional boulders. Craters experience self-shadowing and bouncing radiation and absorption and this behavior requires it's own specific semi-analytical model. To extend the complete analytical YORP model, we present here an extension of normal YORP applied to new small-scale geometries in the form of boulders. When analyzing asteroids visited in the future, we can use these results to make reasonable estimates on YORP from possibly incomplete or low-resolution shape models, such as ones obtained from flybys or impacts.

We have also analyzed the conditions under which consistent orientations or limitations of boulders in specific latitudes can influence the YORP torque experienced by a small body. Size variation notwithstanding, these enforced biases showed the sensitivity of initial YORP estimates. Incorporating a bias in orientation that preferentially points all shapes west greatly increased the original YORP torque bias whereas biasing the location of boulders towards the poles had a less direct effect.

The analysis here was concentrated to two bodies which exhibit different traits in symmetry and dynamics. There is much more analysis to be done on other asteroid shapes and data sets which vary in resolution and surface features. This begins to outline what features to emphasize in hypothetical YORP models that consider the full range of surface roughness which includes cratering, thermal inertia, and boulder populations.

## Chapter 3

### Obliquity Evolution under Boulder-Induced YORP Torques

We continue to model the sizes, positions, and orientations of boulders and randomize these properties to characterize the upper and lower bounds to YORP variability. In studying the shifting obliquity angle rate, we are also analyzing the ease of inducing instability in the dynamics. While the spin acceleration can be derived from longitudinal asymmetry and surface area, the angle acceleration depends on full 3-D asymmetry and the thermal inertia which governs where in the spin period the torque due to YORP is applied. The goal of investigating variance in the obliquity rate induced by the YORP effect originating from surface boulders is to find how much more likely a rough shape is to reach a YORP end-state. In this approach, we will not consider surface redistribution, however this is to be expected when varying the dynamics of a body. For this purpose, it is assumed that surfaces stay static until they reach their spun-up or spun-down dynamical end-state.

#### 3.1 YORP Torques for Obliquity

The equations of motion overall are the spin rate, spin acceleration, change in solar inclination, and change in solar longitude of the ascending node. These last two are substitutes for obliquity angle and right ascension of the pole direction. While solar inclination and longitude are parameterized in the body fixed frame, the obliquity and right ascension are properties of the orbit in the inertial frame. We continue with body-fixed parameters in order express our motion due to the local body-incident forces of YORP. As we've already reviewed spin rate dynamics in the previous chapter, we will reproduce the pole tilt equations of motion here for reference.

$$\dot{i} = \frac{W_B}{\omega} \left[ (\bar{C}_{1,x}(i) + \bar{D}_{1,y}(i)) \cos(\omega T_{lag}) + (\bar{D}_{1,x}(i) - \bar{C}_{1,y}(i)) \sin(\omega T_{lag}) \right] \quad (3.1)$$

$$\dot{\Omega} = -\frac{\cot(i) W_B}{\omega} \left[ -(\bar{D}_{1,x}(i) - \bar{C}_{1,y}(i)) \cos(\omega T_{lag}) + (\bar{C}_{1,x}(i) + \bar{D}_{1,y}(i)) \sin(\omega T_{lag}) \right] \quad (3.2)$$

The term  $W_B$  stands for the fraction  $G_1 \setminus I_z a^2 \sqrt{1 - e^2}$ , and is substituted here to further highlight the emphasis on the YORP Fourier coefficients.

Thermal inertia is approximated in these equations of as a constant time lag, serving to delay the time of emitted energy by some fraction of the period, and in this work we will apply a time lag of 1/8th of the asteroid's currently measured rotation period. This constant time lag ignores the variations in materials of the surface or inertia as a function of spin velocity or time of local day. However, it is useful in these twice averaged equations of motion and allows thermal lag to be isolated in trigonometric terms that scale the first-order YORP torque coefficients. In the next section we will discuss alternative approaches to thermal inertia considerations within these equations.

## 3.2 Results

### 3.2.1 Boulder Distribution Effects on Solar Inclination Change Rates

We find that for each combination of 5000 randomly selected boulders, scaled proportionally by the size distribution which is also randomly but sufficiently sampled from, we find significant variability in the solar inclination torque. We will also map this to the additional west/east surface area that is applied through this procedure. Sensitivity of the YORP effect to the individual boulders is tested by isolating the boulders that contribute more than 1% to the total inclination torque magnitude. This is then analyzed for the distribution in size, orientation, and location.

We have calculated the sum of the torque influence from each boulder and present it in Fig. 3.1 for both the asteroid Bennu and Itokawa shapes. For N=500 cases, we see different variance in

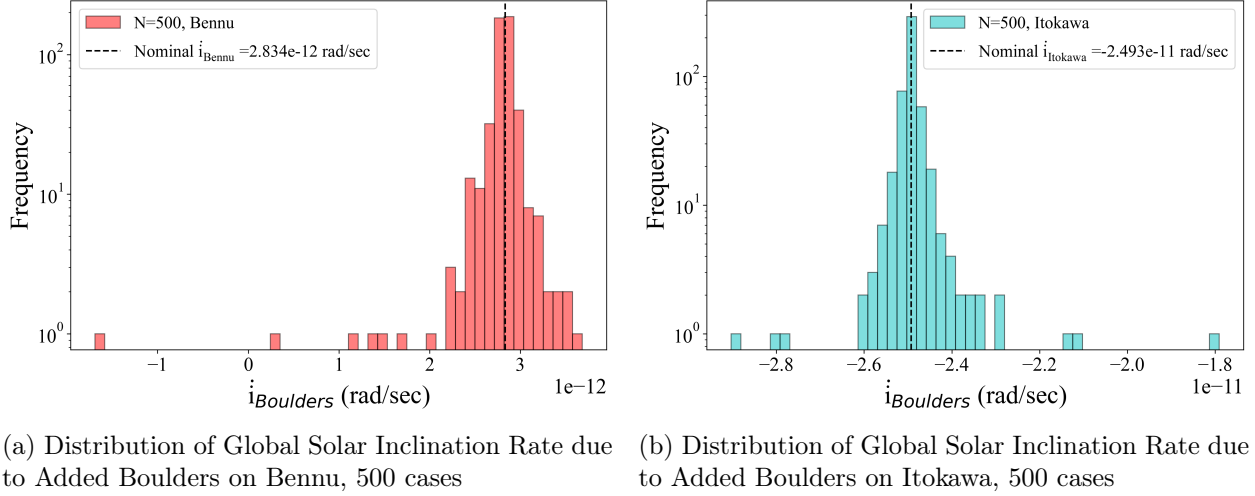


Figure 3.1: Solar Inclination Rates for entire asteroid with 5000 boulders added in 500 different configurations of size, orientation, and location on Bennu and Itokawa shape models

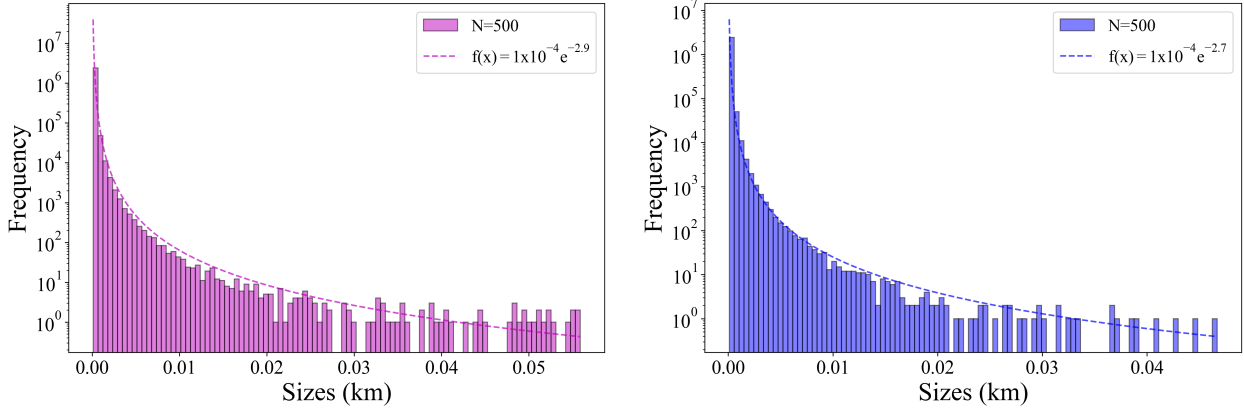
each case. While most of the cases have close to zero change in the obliquity shifting rate due to boulders, we see a handful of cases that deviate towards the maximum influences of  $2\text{e-}12$  and  $5\text{e-}12$ , for Bennu and Itokawa respectively. In the following subsections, we will show the significance of certain properties of boulders and what the distributions of the most influential individuals looks like.

### 3.2.2 Sensitivity

We have applied the characterizations of the size power law of boulders on Bennu and Itokawa that come from image-based analysis due to the OSIRIS-REx and Hayabusa missions. The size of each boulder selected randomly for surface placement was sampled from this power law, modeled by the dashed lines in Fig. 3.2. The histogram shows the full distribution of every size boulder selected for this simulation study. Now we will separate the population by which boulders contribute over 1% to the obliquity changing rate despite each representing a constituency of 0.02% percent of the population.

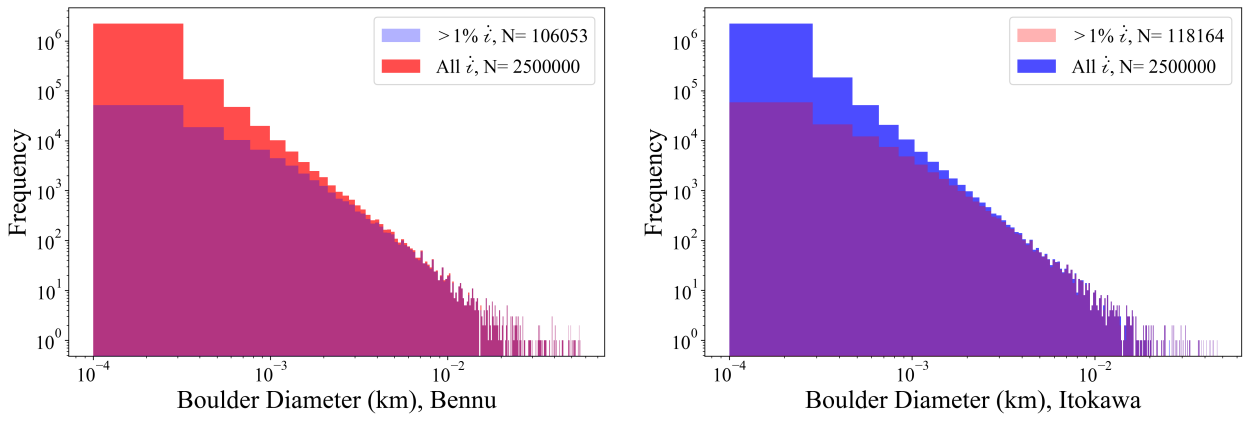
Now comparing Fig. 3.2 and Fig. 3.3, we see that the boulders smaller than 0.01m in diameter begin to be lost when filtering for large contributions to YORP obliquity change. It's the same result

independent of the underlying shape.



(a) Power law size distribution for Bennu in theory and sampled,  $\alpha = -2.9$  (b) Power law size distribution for Itokawa in theory and sampled,  $\alpha = -2.7$

Figure 3.2: Boulder diameter power laws: dashed line is the model and histogram represents the population sampled from power law



(a) Bennu's subsampled results of diameter and percent contribution to solar inclination change (b) Itokawa's subsampled results of diameter and percent contribution to solar inclination change

Figure 3.3: Full histogram of boulder diameters compared to the subsampled set that represents boulders contributing  $> 1\%$  to solar inclination change

The next factor that was randomized during simulations was the dominant face orientation of the boulder model. Each boulder was modeled by a wedge prism with a  $90^\circ$  angle, leaving one face to be the largest and projecting the dominant force for the shape. When binning boulders by their percent contribution to overall YORP, we see a trend arise with increasing YORP inclination change influence. The lightest color in Fig. 3.4 is the population contributing less than 0.1% to overall YORP. Each darker shade represents a 10x increase in the percentage bound. What is seen with this increase is a departure of boulders near  $\pi/2$  and  $3\pi/2$ , which represents directly North and South facing dominant boulders. This is subtle and only represents a 5% bias towards east and west facing boulders. There is a much larger bias when examining the difference in the angular acceleration terms.

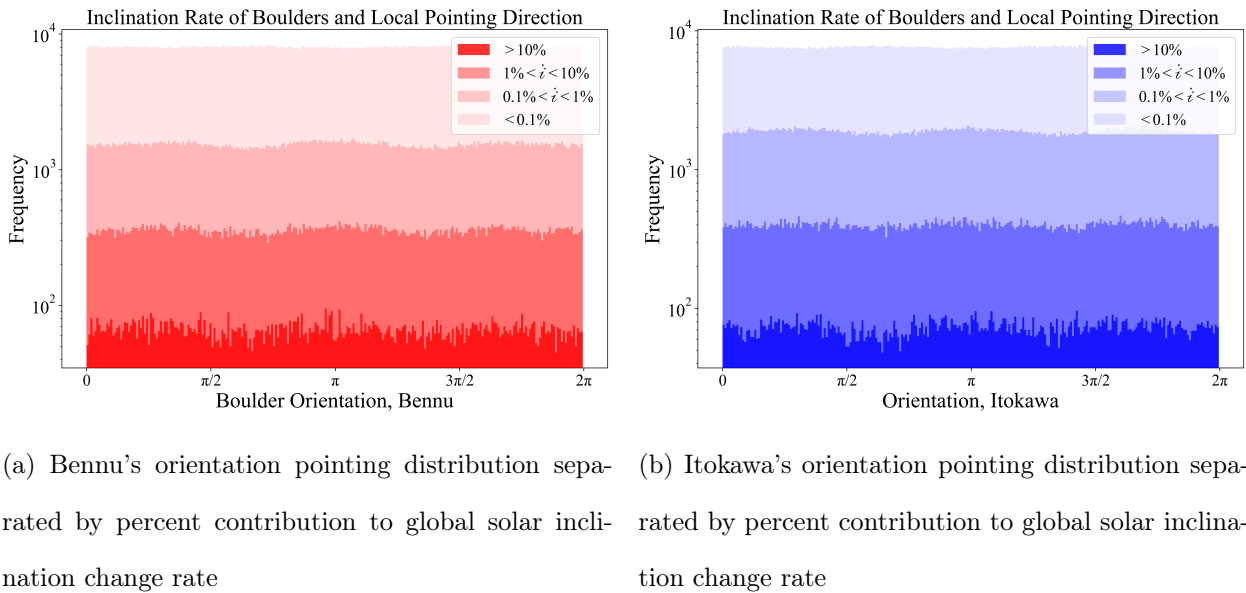


Figure 3.4: Varying bins of percent contribution to solar inclination change, with darker colors representing higher % change from a single boulder, distributed over dominant pointing direction

Lastly we examine the longitude and latitude biases for large contributing boulders. As YORP torque strength is proportional to the norm of the vector from the body center of mass to the surface location of the boulder, we would expect to see larger contributing boulders in areas

with high magnitude  $|\vec{r}|$ . An interesting result from this sensitivity analysis is that we see less influential boulders near the equators when filtering by inclination or obliquity rates. This is shown for both Bennu and Itokawa shapes, see Fig. 3.5. This is the opposite trend from large spin contributing boulders. This can be explained by the difference in spin-inducing YORP factors and obliquity-inducing YORP factors. When a boulder contributes a large value to YORP obliquity, it must induce asymmetry in the xy-plane. Therefore, the boulders located at the equator that contribute equally to torque in the northern and southern hemispheres cause a net close-to-zero solar inclination change.

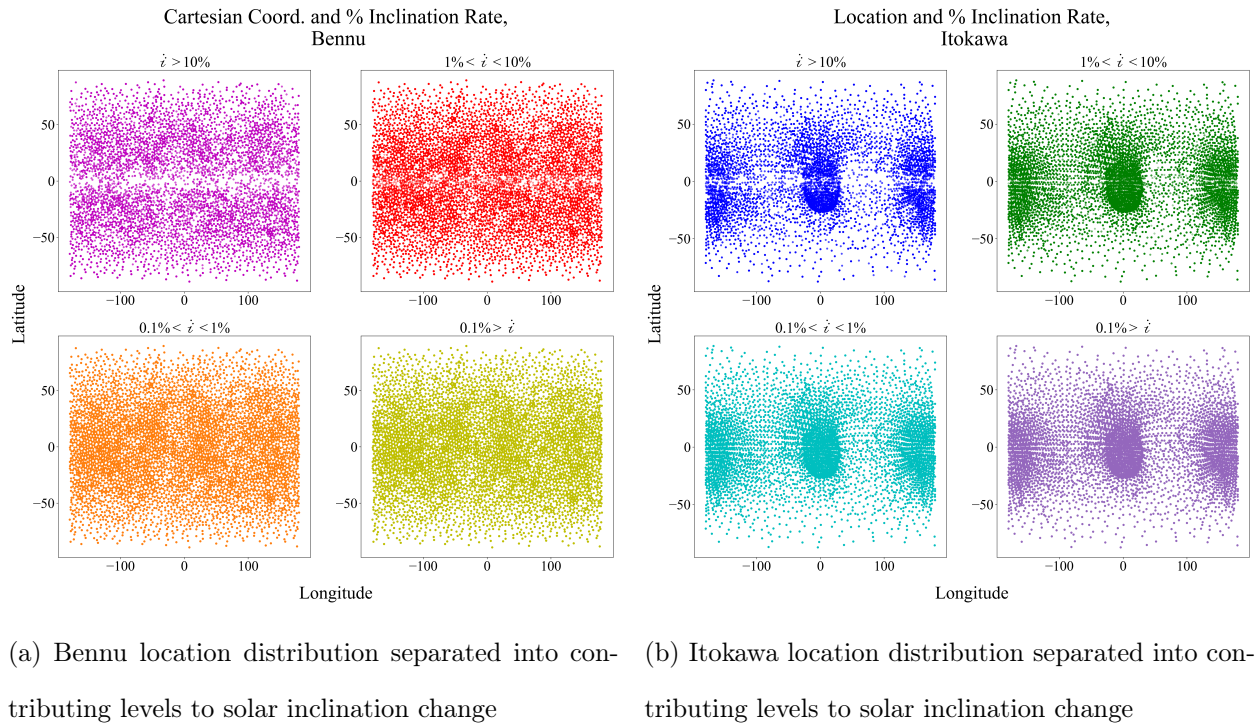


Figure 3.5: Boulder locations separated by percent contribution, showing a departure of boulders from equator at rates of  $> 1\%$  and  $> 10\%$  for both bodies

These results tell us about the influential factors that make an asteroid overall YORP obliquity rate estimate sensitive to boulder presence. This applies the statistics provided from observation and translates them into dynamical predictions. The range of  $\dot{i}_s$  shown here is the possible variation

in obliquity due to randomized boulders. Any of our current YORP estimates may fall into this range if boulders are mismodeled or unmodeled.

### 3.2.3 Boulder Motion

We compare boulder YORP contributions at different locations to make inferences about the impact of boulder's moving on the body's surface. This behavior has been discussed previously and explains the presence of features such as infilled craters on asteroids (Brack and McMahon, 2019). In Fig. 3.6, we sample boulders within  $5^\circ$  of longitude and up to  $9.43^\circ$  in latitude apart. Their obliquity rate contributions, shown as  $\dot{i}_s$ , follow a distinct linear relationship with latitude.

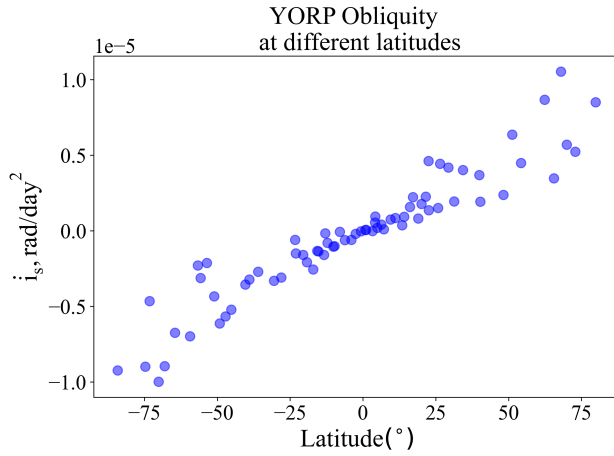


Figure 3.6: Differing amounts of YORP obliquity acceleration for boulders within 5 degrees in longitude but varying latitudes

Comparing the differences between neighboring boulders gives a more random relationship. It is shown that a boulder at a higher latitude could have a lower or higher amount of torque changing the body's obliquity. The largest change in  $\dot{i}_s$  is  $7.06 \times 10^{-6} \text{ rad/day}$ . If we saw this increase in obliquity torque from the most influential boulder in this test case, the single boulder alone could cause a spin pole tilt rate exceeding even the asteroid spin rate within 5 million years. This is one way of describing tumbling behavior and these numbers show how boulders could be the cause of such instability. This assumes uniform spin is independent of obliquity angle change and we

are only looking at dynamics due to a single boulder moving to a highly influential location. The calculations here serve to highlight the magnitude of change due to moving boulders on the surface. In future work, it will be highlighted how necessary it is to simulate boulders moving positions in time as the dynamics change due to YORP.

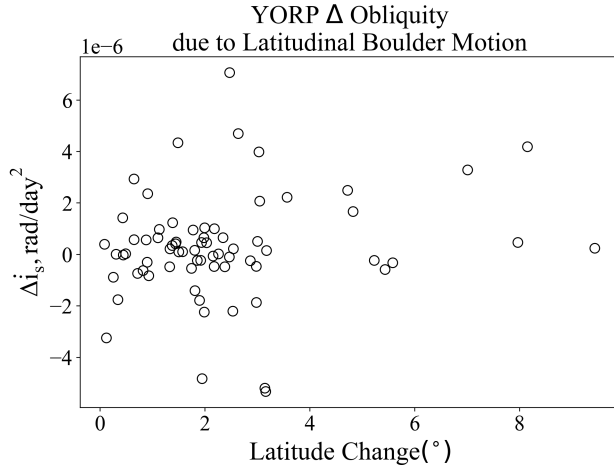


Figure 3.7: The change in YORP obliquity rate from boulder motion with the latitude degree change shown on the x-axis

There are other ways of describing YORP. There are other features which induce interesting thermal effects such as self-shadowing and self-radiation (craters). Boulders move over time as the dynamics change which resets the problem. Regolith roughness can scatter the initial thermal energy and induce even more stochastics to the geometric analysis of YORP. This work has applied what we know about heavily assumed models and high-resolution asteroid surfaces to show variability in the YORP effect. Further observations of asteroid surfaces could further constrain how bouldered they get, what asymmetry is typically induced, and the thermal properties of boulders which may have been fractured, buried, or excavated as the dynamics evolve. We hope to see this continued with more advanced thermal models, the application of boulder motion based on the gravitational field variations, and rigorous ray-tracing in order to get refined YORP coefficients from the original geometries.

## **Chapter 4**

### **Shape-from-Silhouette Modeling of Small Bodies**

#### **4.1 Introduction**

We present an approach to image processing and shape modeling for low resolution shape models. This involves real and simulated imagery, edge detection algorithms, and dramatic lighting conditions. In this work, the models presented are generated from both simulated and actual mission data sources and compared to the most resolute shape models available for the bodies in question. The method is tested on both a convex and irregular body in order to show how our overlaid silhouette trimming procedure responds to self-shadowing, the presence of concavity, as well as phase angles projections introduced by the orientation of the sun and camera. This work will be developed as necessary to enable onboard shape model generation, but this paper serves to present and defend the method which uses a process of refinement based on extending the shape along the silhouette cutout in space, and narrowing down the three-dimensional hull through multiple view angles. As the small body community looks to grant more SIMPLEx level missions to asteroids, such as the Janus mission which will rendezvous with a binary system, it is necessary to develop the autonomous onboard navigation capabilities that make those missions possible.

## 4.2 2D to 3D Mapping of Images to Shapes

### 4.2.1 Assumptions

In it's current formulation, this shape modeling method processes a batch of optical and infrared images taken at a reasonable distance away from a target body. The body does not need to be centered in the frame of the image, nor does it need to be fully lit. The assumptions made in the work to follow include full knowledge of the body frame, beginning with the orientation of the spin pole and further defined by convention. The orientation and location of the camera is known along with its frame, as well as the sun location in the body frame. In actual missions, there is a reasonable track of the spacecraft orientation and location in the inertial (sun-centered) frame, and a state estimate is formed for the body during approach and during ground-based observation campaigns. In this work, perfect certainty of the body location, spacecraft location, and the camera-pointing vector can be assumed.

### 4.2.2 Simulated Image Procedure

Simulated images were necessary to test the robustness of our modeling method. The process of generating these images was performed via Blender software [blender](#) with the goal of recreating conditions of the OSIRIS-REx approach phase to the asteroid Bennu. The shape model was of 6m resolution, sourced from the approach data results given by the OSIRIS-REx mission [Lauretta2019](#). Lighting conditions, such as the sun location, were manipulated to match the testing criteria but the inherent qualities were kept constant: a light strength of 5 MW, 0% specularity, and a radius of 1m were suitable to illuminate the target for the purpose of recreating mission-similar conditions. Both a regular and irregular body were tested. The camera dimensions were kept in accordance with the PolyCam on the OSIRIS-REx mission [Rizk2017](#).

### 4.2.3 Mission Data

The data obtained to further test the modeling software was sourced from the OSIRIS-REx and Hayabusa mission SPICE archives. Necessary data regarding the camera dimensions, frame-to-frame transformations, the state of the camera, body, and sun were accessed as well as the images themselves which came from the PDS archives but their timestamps allowed for coordination of state and image. Shown below is an example of similarity between the simulated image sets and actual mission data, which proves that moving forward with both can provide comparable results when focusing on the silhouette information.

#### 4.2.4 Identification of the Silhouette

The procedure of shape generation using optical data begins with processing the images and finding the desired information - the silhouette of the body. The data shows results where the camera is within 100km, 151km, and 8km of the target body for the simulated test cases, the OSIRIS-REx data, and the Hayabusa images respectively. Examples of the input are shown in Fig. The simulated images and the mission data differ most in their surface detail, where rocks and boulders can be seen readily on mission images but are majorly missing from the surface representations of the shape models processed by Blender. For the purposes of silhouette-based shape modeling, this detail is acceptable and there are many steps implemented to ensure that all data sets are treated equally. This algorithm begins with a pre-processing thresholding

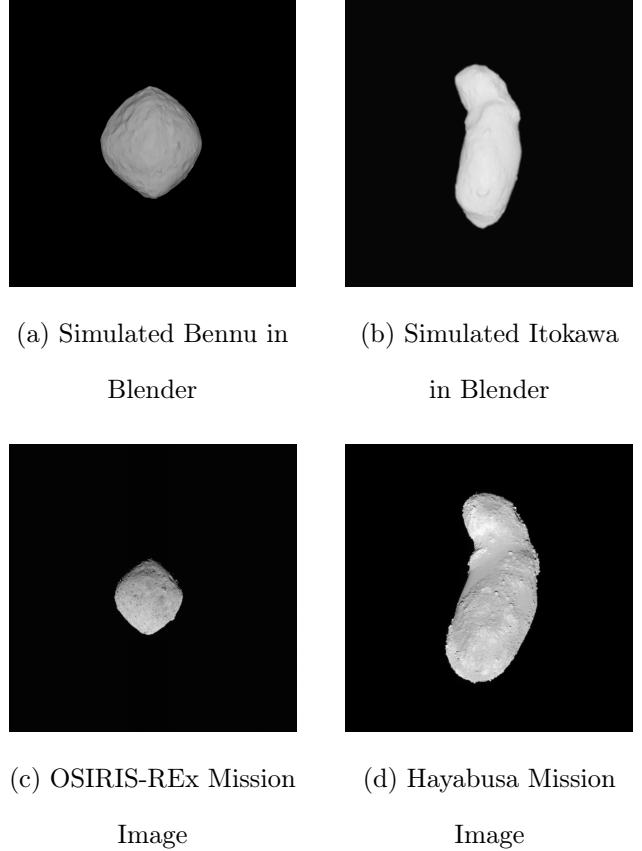
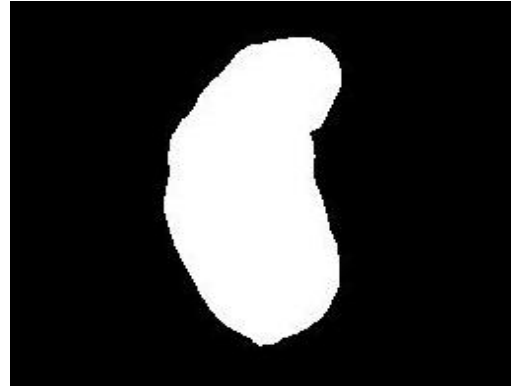


Figure 4.1: Example Images

procedure. An image is translated from RGB values into grayscale between [0,255] in intensity. These values are then flattened with the lowest intensity pixels (< 2) removed and all other intensities amplified by a factor of 1000. This produces a flat background of space with a bright masked featureless image of the body.



(a) Unprocessed Itokawa Image



(b) Processed Itokawa Image

With a preprocessed, thresholded image, the next step is to apply an edge detection function in order to differentiate the silhouette from the background of space. The function used here is the Canny operator, which can be tuned for sensitivities that correspond to the level of detail desired-Canny1986. The Canny algorithm applied via Matlab function involves several steps as follows. The first step is to apply another Gaussian filter to smooth the image and thus reduce noise for calculating the edge locations. The equation for the Gaussian kernel applied to the image is below, for an image of size  $(2k+1) \times (2k+1)$ :

$$H_{ij} = \frac{1}{2\pi\sigma^2} \exp\left(-\frac{(i-(k+1))^2 + (j-(k+1))^2}{2\sigma^2}\right); 1 \leq i, j \leq (2k+1) \quad (4.1)$$

After the Gaussian noise reduction kernel has been applied, the function needs to find the intensity gradients in the image in order to identify locations of possible edges. The Canny algorithm uses four filters to find four different directions of gradients: vertical, horizontal, and two different diagonal directions. The edge gradient and associated direction is given by the equation which

considers both the gradient in the x dimension and the y dimension.

$$G = \sqrt{G_x^2 + G_y^2} \quad (4.2)$$

$$\Theta = \tan^{-1} \frac{G_y}{G_x} \quad (4.3)$$

After the gradient is calculated over the image, the desired thresholding factor is applied to eliminate edges of very low or high intensity. In this approach, it is typical to eliminate a large proportion of low intensity edges which, in the particular data sets applied, corresponds to ridges and boulder shadows. At the end of the thresholding process, the algorithm can be confident to a significant degree that it has identified the edge of the objects captured in the given image.

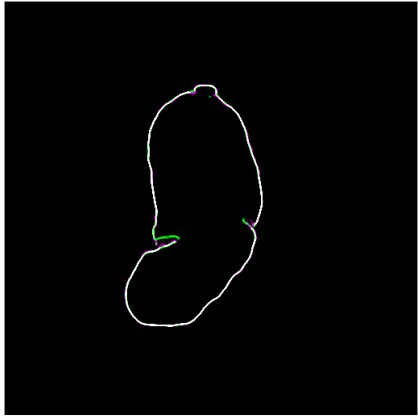


Figure 4.4: Four Edge Results Overlaid  
in Image Space

In order to capture the edge, the Canny operator was tested for effectiveness over many threshold and standard deviations. Examples of these results are given in Fig. which present the extremes that the function is capable of capturing from the typical asteroid image. The selected values for edge processing were  $T=0.5$  and  $\sigma = 5$ . Combined with the previous thresholding steps that output a flat mask, this operator has no issue identifying an appropriate edge for silhouette finding. After the edge is identified, the points are sorted in unit circle order, beginning at the traditional  $+x$  axis and moving counter-clockwise in the  $(u,v)$  plane. Each image is subsampled to contain an evenly spaced set of points from the full edge result. This is one way in which the data density is reduced for the purpose of faster processing. The original

Canny edge output represents each pixel identified as an edge, which can be thousands of data points.

Taking the four best results from the Canny investigation above, they are overlaid in Fig.

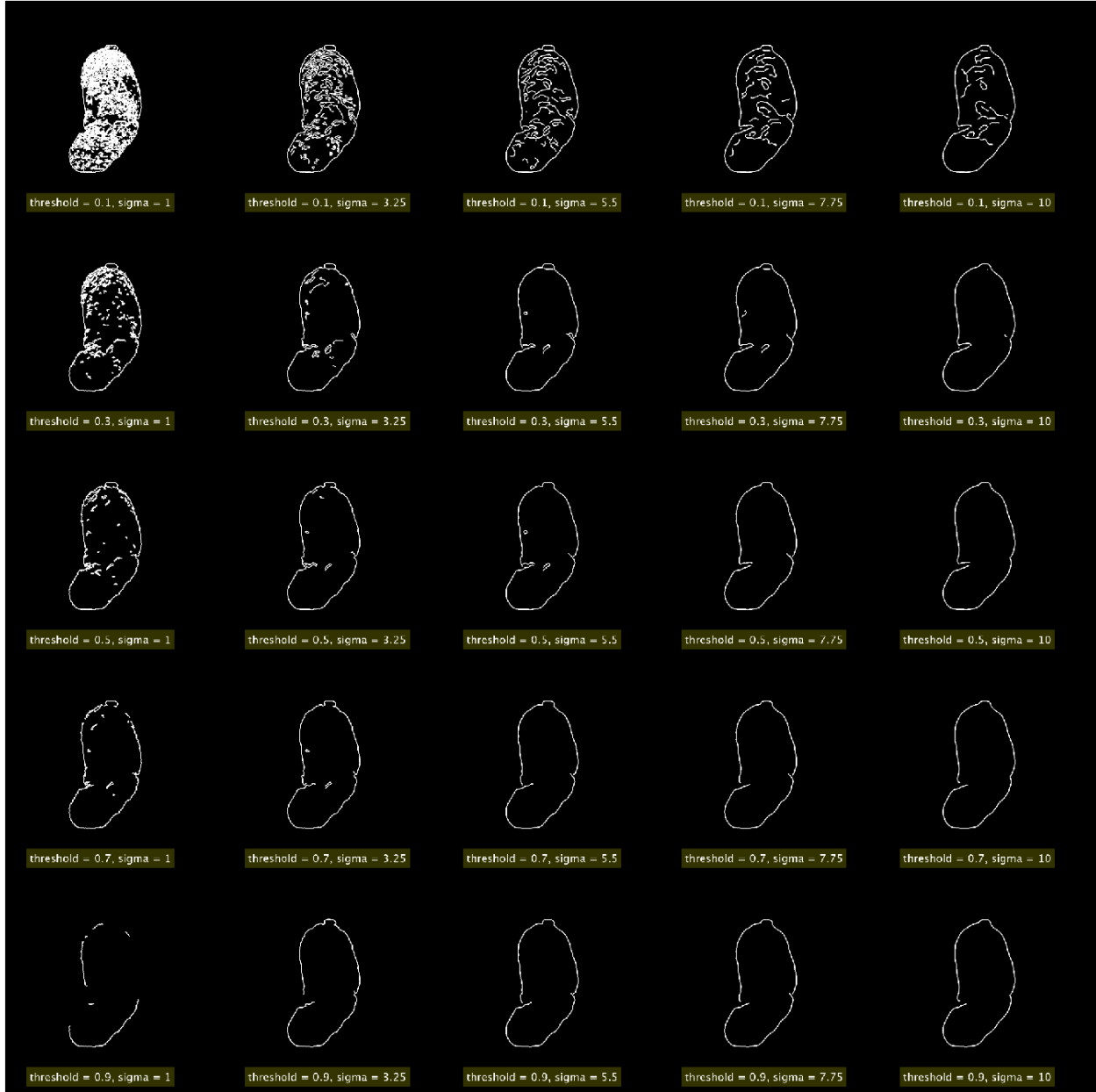


Figure 4.3: 25 Examples of Canny Parameters and Impact on Edge Detection

to show that differing parameters still provide similar results. The difference between each output is only measured by a few pixels, therefore it can be assumed that the ultimate shape results will not be majorly affected by changing the Canny parameters, as long as the parameters implemented have met the original requirement of identifying only the silhouette and excluding internal features.

After identifying the silhouette in the image frame and thus in the 3-D camera frame with

the addition of the range dimension, the points must be translated into the 3-D body frame which is predefined and known prior to processing. This is an assumption made based on the expected capability to obtain lightcurve information both on the ground and early in the flight plan which will inform about the spin pole and allow for a definition of the body frame to be made. However, for the purposes of this work, the body frame is accessed via SPICE and from scientific convention Fujiwara2006Scheeres2006. This transformation allows each image to be considered in the body frame against one another, which is what enables the ray trimming process. The points are extended towards and away from the camera direction with the center of the ray corresponding to the originally identified edge point.

#### 4.2.5 Terminator and Limb Discrimination

One major known quantity in any space mission is the direction of the sun vector. This is increasingly important for a small body in which the whole shape can be observed along with the terminator, which is dependent on the relationship between the body, the camera, and the sun positions. In this work, it is assumed that there is perfect knowledge of the sun location and thus the unit vector corresponding to the sun direction in the body and image frames. This state allows for a calculation of the phase angle which becomes crucial when differentiating a limb versus a terminator in an image of a body that is only partially lit. The knowledge of the sun unit vector in the camera frame allows for simple vector products to separate the edge points which are facing the sun and the points which are on the opposing side.

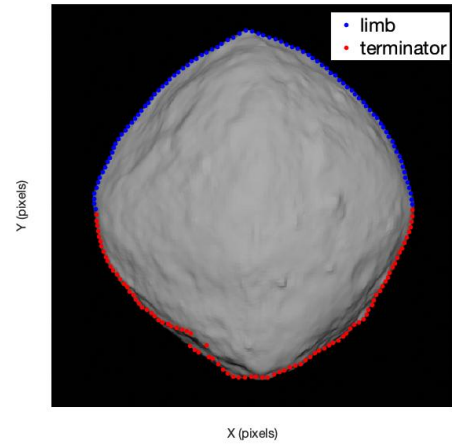


Figure 4.5: Limb and Terminator in Bennu Mission Image

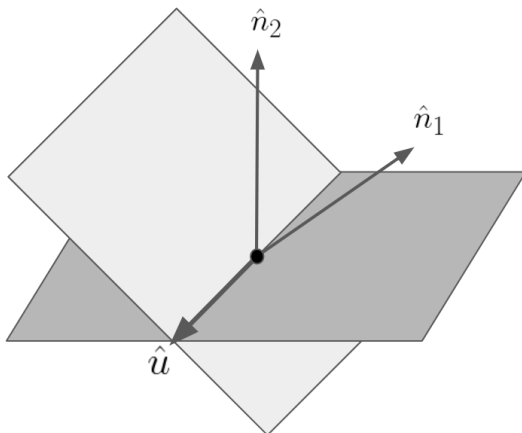
#### 4.2.6 Ray Generation and Trimming

The silhouettes have been identified and placed in their assumed positions in the bodycentric frame of the target, and now the next step is to extend these points into rays which will concentrically constrain the surface McMahan2018. The reason why the rays are necessary is that the points themselves may be misaligned, contain outliers, or possibly not hold enough information to solve for a reasonable resolution of the surface. Extending our points into rays which will be trimmed based on intersections and subsampled allows for more detail without requiring more information.

The rays are described using a line equation to characterize them in 3D body frame space. The equation of the line segments is as follows for  $i$  number of rays  $l$  in each view.

$$l_i = l_{i,0} + \eta L \hat{r} \quad (4.4)$$

In the above equation,  $l_{i,0}$  is the initial point of the ray,  $\eta$  is the scale factor from 0 to 1 describing how far along the rays length it's been trimmed (between 0 and 100 percent),  $L$  is the length of the pretrimmed ray, and  $\hat{r}$  is a generic unit view direction. For this investigation, the original ray length  $L$  is set to 2km, centered at the identified edge point and extended towards and away from the camera for limb points, with terminator points at a slight rotation proportional to the phase angle. The  $\eta$  factor is calculated after finding all intersections between each limb plane and trimming each ray down to its likely surface section, and this procedure will be described in later sections.



With a sample of  $N_p$  edge points, there can be  $N_p$  number of planar quadrilaterals formed by connecting each adjacent edge point as seen in Fig. , and calculating its surface normal direction with the following equation:

$$\hat{n}_k = \frac{\hat{r} \times (l_{i+1,0} - l_{i,0})}{|\hat{r} \times (l_{i+1,0} - l_{i,0})|} \quad (4.5)$$

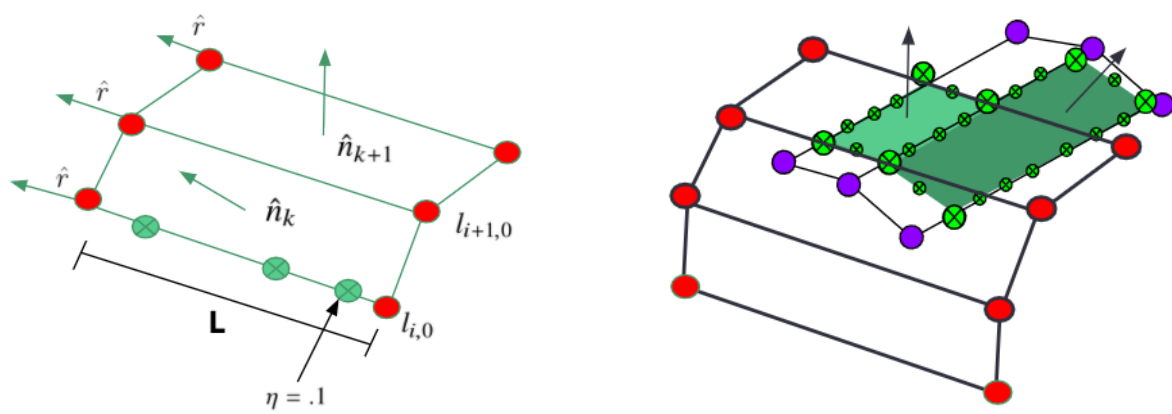
The planar quadrilaterals will be referred

Figure 4.6: Geometry of Two Intersecting Planes

to as patches in the following discussion. These patches have an associated normal vector, and two rays which describe the lines in the  $\hat{r}$  direction. Processing this information in a batch method, all of the rays are iterated through to find where each plane intersects with another plane from the found silhouettes. The locations of the intersection, along with the percentage along the ray that the location is identified, are saved and then evaluated to find where the rays need to be trimmed away. The line of intersection between two planes in 3D space exists if the cross product of the two normal vectors associated with each plane is nonzero. If  $n_1 \times n_2 = 0$ , then the two planes in question are parallel and will be ignored. In the implementation presented here, the threshold for a nonzero parallel evaluation is that the magnitude of the cross product of the normal vectors is above  $1 \times 10^{-10}$ . The line of intersection itself also lies along the cross product of the two normal vectors. If an intersection can be found, the  $\eta$  value corresponding how much of the line should be kept is saved, and the rest of the line is trimmed and the equation of this specific line is updated to go between  $\eta$  length and the other remaining end for the next iteration. Now the direction vector of the intersection line can be founds using the normal vectors of the two planes, as shown in Eq.3. The variable  $m$  gives the direction of slope, and a point on the line is found numerically, which corresponds to  $b$ , and from there a whole line equation is given in  $y = mx + b$  form.

$$m = \frac{\hat{n}_1 \times \hat{n}_2}{|\hat{n}_1 \times \hat{n}_2|} \quad (4.6)$$

The results from the line intersection calculations are many line equations describing the unit vector corresponding to the direction of the intersection line, the end points of the original rays, and the points corresponding to the physical end of the intersection line for these finite patches. The next step is to evaluate which parts of the ray must be trimmed away based on the identification of a crossing, and which portions of the ray are kept. The algorithm sorts the points along the intersection ray based on the percent along the ray which they fall, and then locates where the calculated projected normal directions switch in sign. This switch is the indicator of an intersection



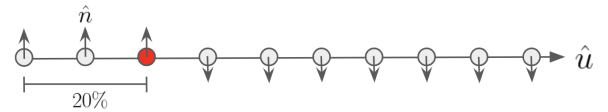
(a) Two adjacent edge planes with sampled points along the line of length  $L$       (b) Planes and their associated normal vectors: Two observations

Figure 4.7: Geometric Depiction of Patch Crossing Calculations

with another limb patch, and therefore serves to show where the ray must be trimmed. In Fig. the point identified is 20% along the intersection ray, with a positive normal direction. The point which will delineate the trimmed portion of the ray is at 50% along the original ray, where the surface normal vectors have switched. The derivation of a surface normal direction is crucial for the process of delineating which points intersect on the body and which points intersect off the body and therefore should be discarded. The points that theoretically constrain the surface are what's left after a ray has been processed to find intersections meant to eliminate the points that extend too far.

As the views are iterated over, the plane intersections are examined and a check is performed to find out if the plane segments are on the inside or outside of the silhouette using the calculation of the surface normal from Eq.3. The segments that are kept are not intersected at all, and therefore must represent our knowledge of where the surface is depending on the resolution of our observation data. As shown in Fig. one view overlaps with another view and two patches are found. One patch is formed from coplanar limbs and the green points represent the intersections saved. The other patch only intersects the first view on one side, so only one side of the original limb gets trimmed down and resampled. Both of the resulting patches, shown by the green planes, have new normal directions based on the normal directions of the limbs that were intersecting to form them.

After iterating through each view and trimming off the pieces of the rays that become intersected by another silhouette, the algorithm saves the remaining points as a point cloud output result. The segments of the original ray that are kept are the ones that were never inter-



sected. This evaluation is strict and a misidentified edge point could result in the trimming of necessary and correct surface data. This drawback is kept in mind during the tuning procedure of the Canny edge detection function, which is designed to be the least sensitive and therefore refined to only identify true edge points. Depending on the

Figure 4.8: Intersection Ray from Two Patches - Ten Sampled Points and Associated Ray Normals

range of the observations about the target body, the surface can be resolved to different magnitudes. It is possible to localize using single-view geometry because of the assumption that range is known. Without this assumption, a multiple-view refinement of location using the coordination of edge points along epipoles within the image frame would be required. This estimation capability can easily be implemented in future iterations of this work in order to reduce assumptions and provide further autonomy to the method. However, in the scope of this work, it is assumed that the attitude and range are known quantities for our spacecraft. If a full equatorial survey is able to be conducted, the resulting model will have more data and thus can be further refined by our method compared to a survey with less frequent observations taken. In the test cases presented in this paper, simulated data was used to represent an optimal scenario of observational ability. Using Blender blender, the case of a  $0^\circ$  phase angle could be simulated for maximum limb brightness and the elimination of a terminator. Data sets were collected for both Itokawa and Bennu, to examine the individual challenges of mapping an irregular shaped body versus a symmetric body.

#### **4.2.7 Outlier Rejection Scheme**

Once the limb rays have been iterated on and their final intersections have been trimmed down, the remaining points and their associated surface normal directions are saved as 3D data suitable to represent a point cloud. In order to reconstruct a surface from the points, we first have to sample down the number of resultant points in order to eliminate outliers from a coarse trimming bias and promote a smoothing of the final surface Pomerleau2013. We also implement a function to filter out noisy particles Rusu2008. This function keeps any points that have 10 neighboring points within 1 standard deviation of the mean distance between all points in the point cloud.

#### **4.2.8 Surface Reconstruction with Ball-pivoting**

Solving for the final surface involves implementing a method that calculates triangular facets and their associated normal unit direction. The method implemented in our work is a ball-pivoting approach that results in a completely closed manifold. The ball-pivoting method forms a closed

shape from a point cloud using a ball with a pre-specified radius  $\rho$ . A triangular face is formed if the ball, initialized at a random point, contains no more than three points Bernardini1999. This ball moves along the edges of the triangles solved until it has reached every point available. From there, Delaunay triangulation is applied to find the optimal vertices for each facet and connect the shape as it would fit over a closed volume, as one would expect for a small body DiAngelo2011. These methods for reconstruction were chosen because of their geometric simplicity and their restriction to form a closed surface which is a requirement for any small body target. As shown in Fig.4.9, we capture some of the finer details of the shapes despite the lower resolution of the limb-based method.

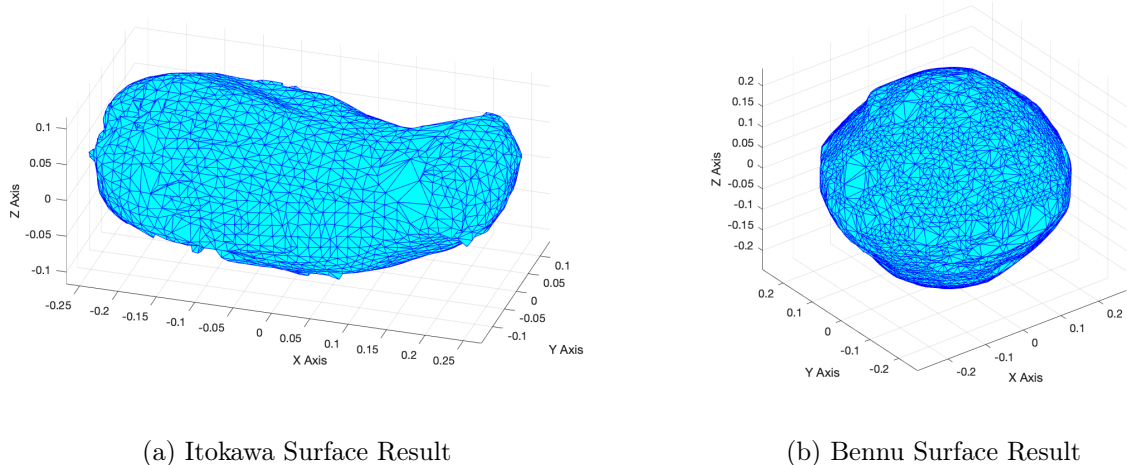


Figure 4.9: Ball-Pivoting Surface Reconstruction Results of Itokawa and Bennu Point Clouds

## 4.3 Shape Results

### 4.3.1 Simulated Data

Using 21 simulated images of Itokawa and 11 images of Bennu, spaced  $33^\circ$  apart along both the equator and prime meridian of the bodies, generated in Blenderblender, we were able to resolve the following point clouds and the resultant closed mesh. We also report the shape model's relative error compared to a high-resolution models of Itokawa and Bennu made using SPC Gaskell2006

from the Hayabusa and OSIRIS-REx missions, respectively. This error is calculated using a per vertex geometric distance between the measured mesh (built using iterative limb-trimming) and the reference mesh, or the detailed, high-resolution Gaskell models. We find that both models are extremely close to the truth, with error on the order of meters. Compared to more-precise methods that fit landmark data to maplets, our method gives similar results. The point-cloud post-processing steps are able to reduce the artifacts leftover from limb-trimming, typically observed as lines across the final surface. However, we would like to reduce the dependence on post-processing in future works for the sake of retaining information about smaller features that our current algorithm was not refined enough to pick up, such as large boulders on Bennu.

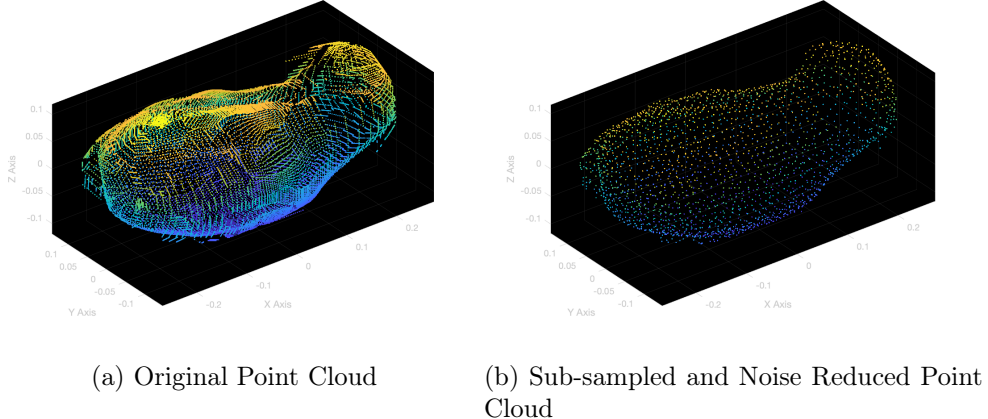


Figure 4.10: Pre- and Post-Processed Point Cloud of Itokawa Limb-Trimmed Shape

The reconstruction of Itokawa based on 21 simulated images is shown in Fig.4.11. The resultant shape is overall smooth along the surface, the concavities in the structure have been captured well based on the data survey, and the error in the shape when compared to a high-resolution model is between -22 and 33 meters, with an average surface error of -3 meters. The longest dimension of Itokawa is approximately 535 meters, which means that the body could be mismodeled up to 6 percent. The map shows that areas around the intersection with the x-axis present the most negative surface errors. This is believed to be caused by an assumption made about the rays extending from the camera frame to the edge of the body. The calculations described in previous sections assume

that  $\hat{u}$  are straight, parallel when traced from the body to the camera. However, the images were captured at a relatively close distance where this assumption cannot hold without repercussions in the final shape. A better modeling technique would be to consider the line-of-sight vector from the center of the camera frame to the edge of the body, which extends as a cone shape.

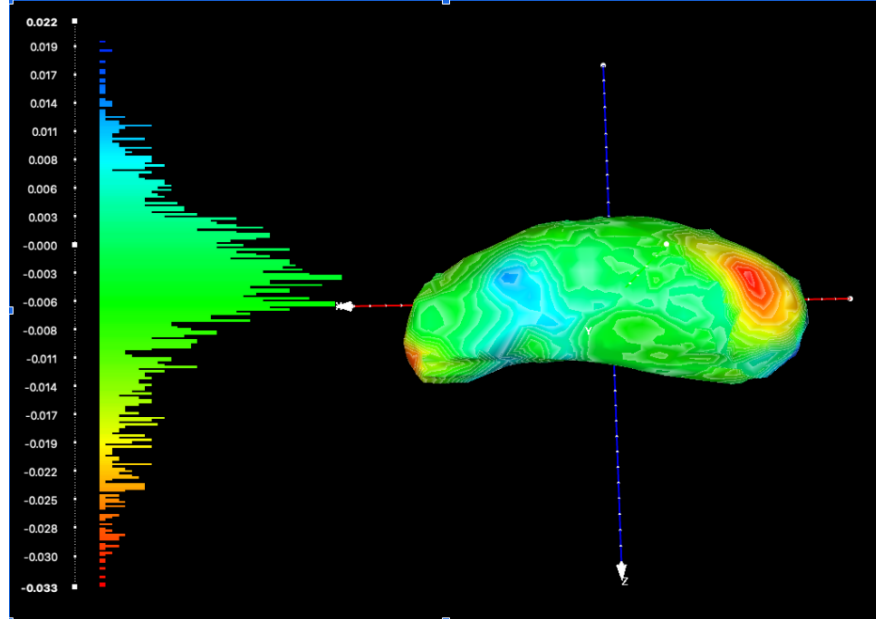


Figure 4.11: Limb-based Itokawa shape compared to SPC, with surface error in units of kilometers

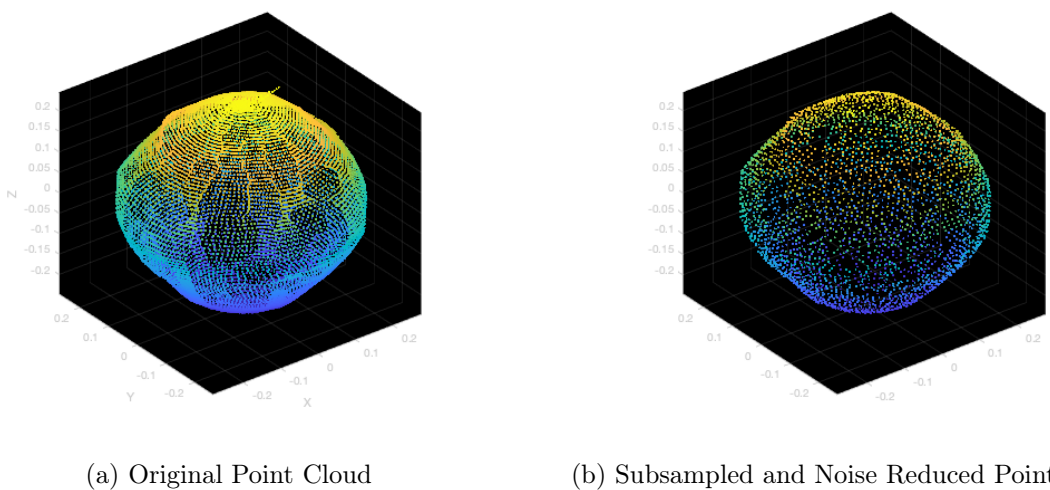


Figure 4.12: Pre- and Post-Processed Point Cloud of Bennu Limb-Trimmed Shape

The model shown here, developed using 11 images of Bennu along it's equator, is also a comparable shape result when measured against high-resolution models such as the 75cm surface model developed using observations made by OSIRIS-REx. The error found using the per-vertex geometric measuring approach is between -2.1 and 2.0 meters, with an average error of 0.5 centimeters. With the largest dimension of Bennu measuring at 565 meters, this represents a maximum mismodeling of 0.4 percent. This model has no predictable areas of under or over-estimation. The resulting shape is smooth, captures the size and general shape of the body, and could easily be used in any proximity navigation solutions. Using data from a relatively close range, we expected the same perspective errors as were found in the Itokawa model, however, the simple convex shape of Bennu was easily and accurately mapped using it's silhouette.

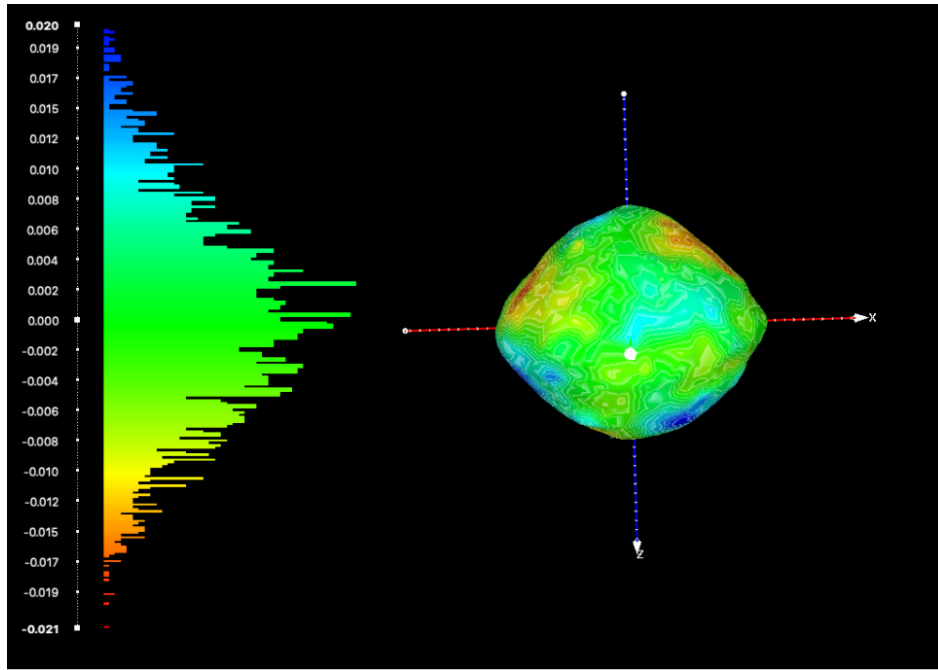


Figure 4.13: Limb-based Bennu shape compared to SPC, with surface error in units of kilometers

#### 4.3.2 Shape Modeling from Mission Data

The last limb-trimmed shape model presented is developed using real mission images taken during the approach phase of the OSIRIS-REx mission by the PolyCam instrument. The major

factor differentiating the previous simulated data models from the following model is the appropriateness of the zero degree phase angle assumption. For these reconstructions, we found views that had a low phase angle and therefore could easily ignore the terminator when searching for edge contours in the images without propagating large error in the model. It is to be expected that ignoring the phase angle between the sun and the body will always cause an under-determination of the shape by assigning the terminator as sunlit limb points. This drives forward future work in delineating terminator and limb from varying phase angles, however, the model presented here works under the assumption that the body is always lit from behind the direction of the camera.

Implementing the same procedures as shown in previous sections, we were able to process 70 images of the asteroid Bennu using Canny edge detection for the silhouette identification and limb-trimming for shape resolution in order to build a surface model from these initial silhouette points. The results show that the model is biased towards underestimating the size of the surface, with the error spanning from -55 to 7 meters, and a mean error of -7 meters. As predicted, the phase angle assumption caused terminator points to be associated with the edge, therefore reducing the size estimate of the body as a whole based on the trimming scheme. However, the shape is reasonably captured based on the dimensions of Bennu and could be used for initial navigation when better data is not yet available.

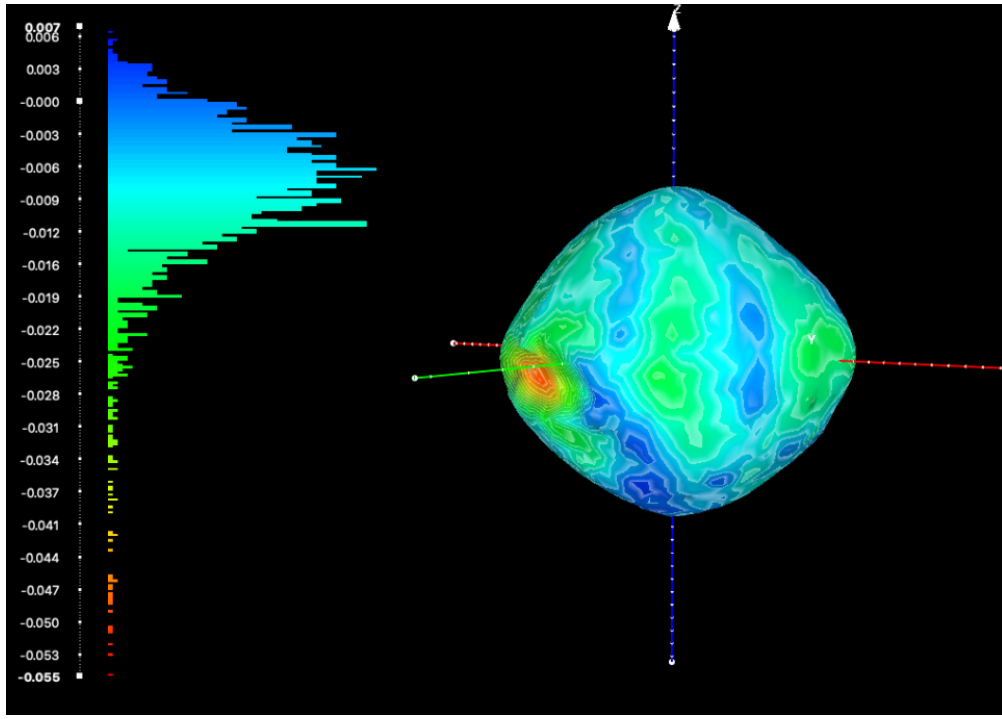


Figure 4.14: Bennu Shape Model from Real Images, compared to SPC, surface error in kilometers

## 4.4 Matching Localization with Normalized Cross-Correlation

### 4.4.1 Methods

The step of localization is important for any autonomous system to be able to navigate with the onboard generated map without human interference. Keeping a record of images with known locations about the body is one way to inform your future observations of their current orientation and range. We show a simplistic localization method based on finding correlations between test images and a library of images which were collected to build the initial model. With the asteroid Itokawa as our model, we use the Hayabusa mission image set from Oct. 1st, 2005 as the test images. The goal was to provide a test image with an associated latitude and longitude, and find the highest correlation score between this test image and the set of library images previously saved. Ideally, the highest correlation score would correspond to the same latitude and longitude between the test and library image. The process of correlation followed a simple iteration scheme where each test image was measured for a correlation score between each library image. We used a set of 36

library images of Itokawa generated in Blender with varying longitudes, spanning every 10 degrees. This library was acceptable for the images taken on approach, seeing as both the test images and the library set only greatly varied in the longitude orientation due to the spacecraft approaching the target body at an angle perpendicular to the spin axis on the day that the data was taken.

The correlation score is an important quantitative measure of similarity between images. This value,  $r$ , was measured between two binary images, and falls between 0 and 1, with 0 meaning no correlation between the images, and 1 meaning that the images have exactly the same pixel values for each location. The score used in this study was calculated as follows:

$$r = \frac{\sum_m \sum_n (A_{mn} - \bar{A})(B_{mn} - \bar{B})}{\sqrt{\left(\sum_m \sum_n (A_{mn} - \bar{A})^2\right) \left(\sum_m \sum_n (B_{mn} - \bar{B})^2\right)}} \quad (4.7)$$

In the correlation coefficient equation,  $m$  and  $n$  refer to the  $u$  and  $v$  axes of the images in question,  $A$  corresponds to the test image,  $B$  corresponds to the reference image, while  $\bar{A}$  and  $\bar{B}$  refer to the two-dimensional mean of the pixel intensities in image  $A$  and  $B$ , respectively. The images in both the test set and the library were all 1024x1024 pixels. No stars were obvious in any of the test images, however, the test image corresponding to 89° was found to be flat.

#### 4.4.2 Results

Correlating two images based on pixel values has proven to have some promise, however, our approach did not successfully match test images to the correct corresponding library image. The test case based on the asteroid Itokawa has shown that the body exhibits symmetries along certain axes that make it difficult for this correlation method to match the correct longitudes. We have learned that high correlation scores are possible between images that are meant to be matched, which shows that the 2-D correlation coefficient can see some similarities between images taken at the same longitudes. If this method were to be applied for localization procedures, it would need more rigorous matching capabilities. Shown in Fig.4.15, the two images presented are both focused on the same latitude and longitude, both 0°. The corresponding correlation coefficient is above 0.9, which means these images are a strong match to each other. However, the iteration scheme found

another image in our library with a higher matching score and associated our test image with the incorrect image shown in Fig.4.16.

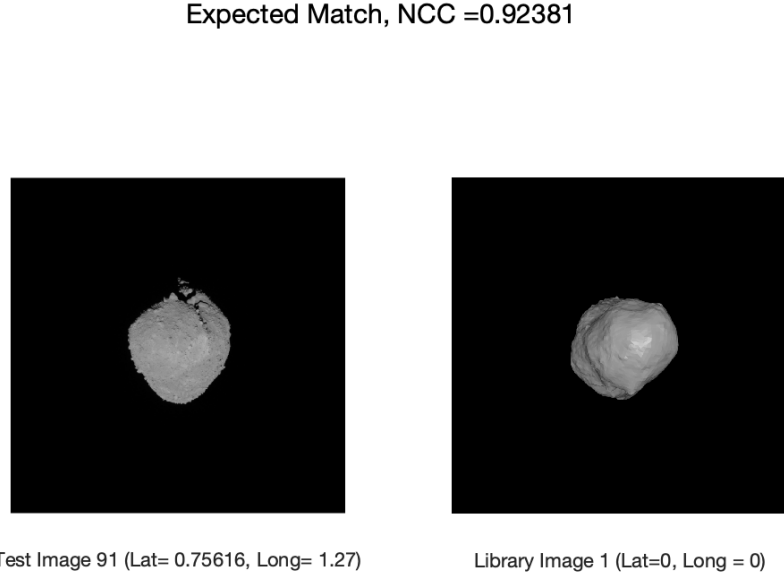


Figure 4.15: Test image and Library Image, Expected Match Pair

We can see from these comparisons that the algorithm failed to account for rotations in the body orientation. The expected match and the actual match have correlation scores within 0.005 of each other, showing that the algorithm can still correlate similarities well. However, this cannot be claimed as a success for navigation purposes seeing that the error in the matched longitude is  $168.66^\circ$ . Further analysis shows that for all of the images in the library, the score of the correlation between the library image and a test image follows a symmetric pattern, shown in Fig.4.17. If this method of localization was successful and we could match test images to their correct library equivalent, we would see the highest correlation scores following a  $y = x$  trend across the score map. The observations made instead show that the highest correlation scores follow the symmetry of the body, and the most likely match in the images are when the asteroid is being viewed from the  $0^\circ$  and

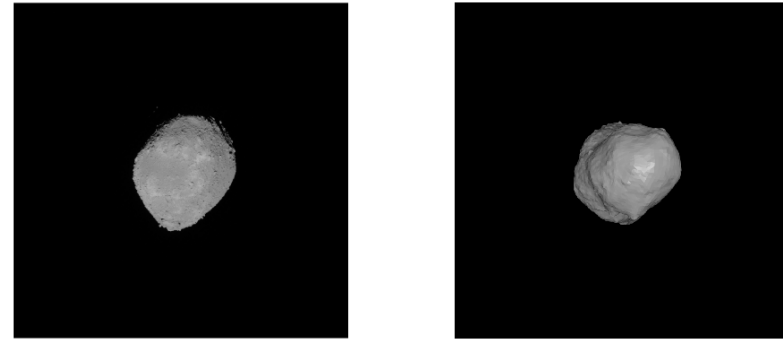
**Highest Scoring Matched Images, NCC =0.92712**

Figure 4.16: Test Image and Library image, Actual Match Pair

180° orientations. This data could be improved with further centering of test images during pre-processing, testing flipped orientations of the library images, or possibly examining the silhouette only for localization. Another avenue of testing could be for lighting-condition invariance, where many phase angles are tested and machine learning is applied to match features despite different sun angles (Manni, 2020).

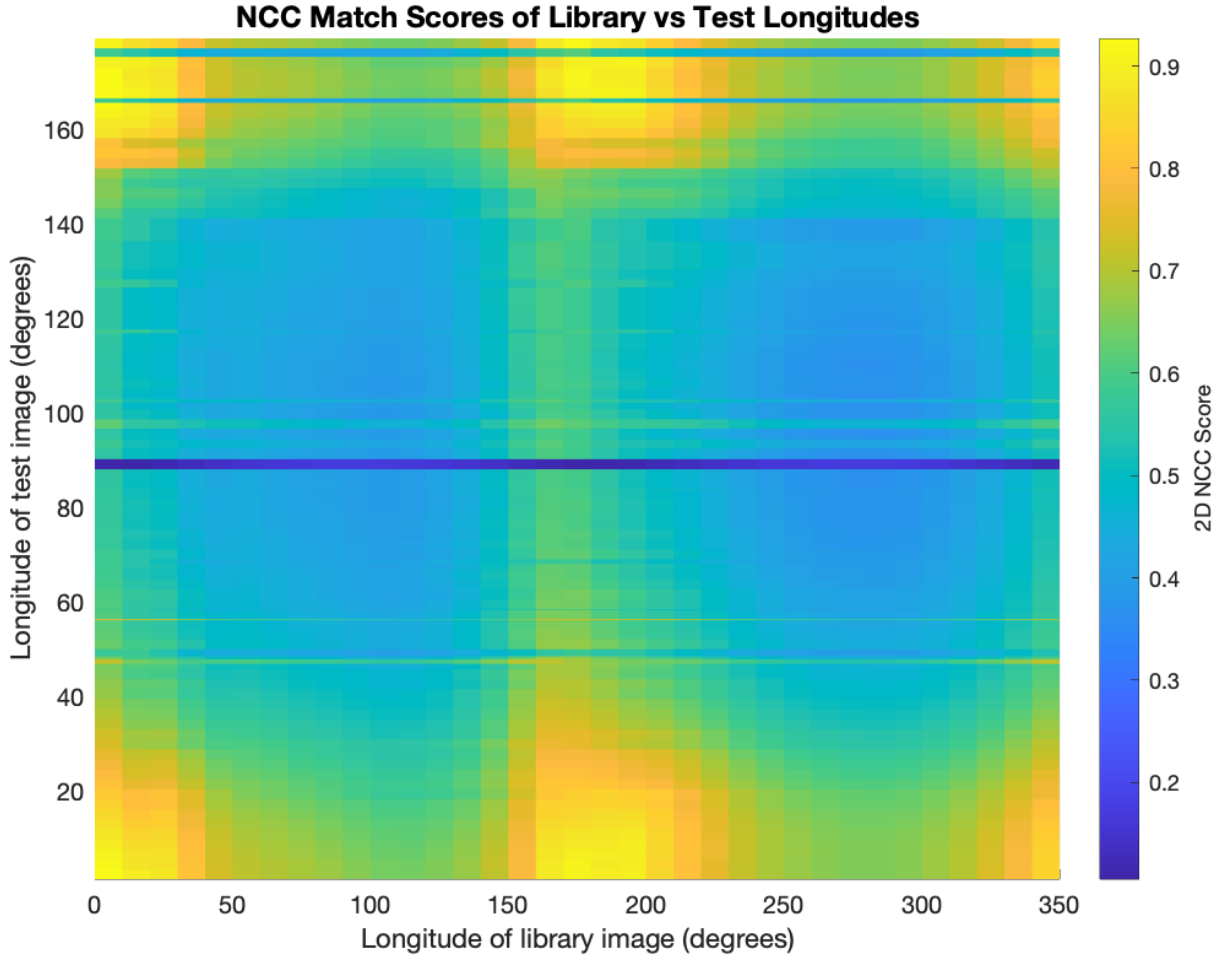


Figure 4.17: 2D Correlation scores between all library images and all test images, based on longitude

## 4.5 Analysis

### 4.5.1 Error Evaluation

The models generated with the limb-trimming method have been compared to mission-derived truth models of the same bodies. The 101955 Bennu shape model used for comparison is sourced from data during the approach phase of the OSIRIS-REx mission, and was made available publicly in November 2018. This model has a resolution of 6m over the surface. The 25143 Itokawa shape model used for comparison is the Gaskell shape model produced with Hayabusa with a resolution of 49,152 facets (Gaskell, 2004). A surface comparison between two shape models is performed using

a Distance from Reference Mesh function, which calculates the closest distance from the reference mesh, or truth model, to the measured mesh, which is the model produced via limb trimming. The distance is left signed to appropriately characterize under- or over-estimated volumes.

#### 4.5.2 Boulder Resolution

With the error ranges seen here, we can expect to model boulders to at least 33 meter accuracy as the worst resolution bounds. Areas with higher accuracy modeling on these shapes can resolve boulders down to 2 meters in diameter. As we have shown in YORP modeling, highly effective radiating boulders (with flat faces) need to be at least 1 meter in diameter to contribute significantly to the global YORP torque. With more realistic shapes such as rounded wedges, this can increase to the tens of meters range. One major takeaway from previous chapters is that for bodies of the rough diameter of Bennu and Itokawa, the boulders that matter for modeling YORP are 1m in diameter and above, with more emphasis placed on large boulders up to the maximum size of 55m in diameter. In this modeling procedure, we can expect to capture the absolute largest boulder on the surface (in the tens of meters range) which will give a small glimpse as to the boulder-induced YORP torque that could be measured by surface modeling. Higher fidelity surface modeling is the driver of better YORP torque models. As we've examined the boundaries of significance, we show that a well-made shape model is necessary for calculating the accurate YORP torques.

We conclude that we are capable of building a shape model for an irregular as well as a convex body given low phase angle imagery. This shape model was comparable in size and shape to the target body and with improvements, could serve as a reliable data product for navigation in a scenario without reliable surface feature identification methods. This work also tests a preliminary, matching-focused localization method that we would like to integrate into a full navigation scheme with further testing. It has been shown that limbs can serve as reference data for a spacecraft navigating about a body, but that irregularities in the shape can cause major error between the predicted limb locations and the observed limb locations (Liounis, 2018). We would also like to challenge many of our assumptions, such as the low phase angle on approach, perfect knowledge

of range and attitude, as well as our fine tuning of the Canny edge detection thresholds. We hope to find ways to iteratively update our model, ingesting new observations after the surface has been constructed, and allowing a transition between low and high resolution mapping methods as a spacecraft finds that better data is available.

## **Chapter 5**

### **Conclusion and Future Work**

This chapter discusses what has been presented here and possible future extensions of this dissertation.

#### **5.1 Summary**

This dissertation analyzes the impact of boulders on asteroid dynamics, puts them in the context of observability from shape-from-silhouette shape modeling, and discusses the possible dynamical outcomes of boulder motion. Using images to build a shape model as well as to inform boulder statistics, we investigated details of the shape and the impact of the resolution of both the base shape model and the boulder diameters. We aimed to provide detail to the concept that the YORP effect is uncertain and stochastically applied in long simulations of asteroid family dynamics. To do so, we sourced in-situ observations of asteroid boulders to inform a simulation model. We assumed a wedge model for inducement of orientation asymmetry, and imposed size, location, and orientation distributions on our full population. We simulated 500 models of 5000 boulders on two separate bodies of similar radii to investigate the impact of convex versus irregular shaped bodies on the boulder-induced YORP effect. These simulations calculated the YORP coefficients  $C_0$ ,  $C_1$ , and  $D_1$  in order to find the rate of angular velocity and rate of solar inclination change for each facet of the shape and boulders. This expanded the computational effort of calculating YORP by 8 times due to the consideration of 8x5000 more facets from boulders versus the 5000 facet base shape models. Further analysis was done to induce biasing in the locations and orientations of boulders to

find the sensitivity of YORP spin acceleration to these factors. We've shown how boulder motion in latitude can accelerate the YORP timescale or induce tumbling modes. The statistics presented in this work will inform ground-based YORP estimates for bodies in the rubble-pile size regime.

## 5.2 Applications of Boulder YORP Modeling

One application of this work is to compare ground-based YORP measurements of Bennu with the highly detailed measurements made by OSIRIS-REx and make up the difference in measurements with randomized boulder models. The same can be done for Itokawa which has ground-based and space-based shape models as well as boulder statistics and boulder-induced YORP calculations shown here. Through this verification, it can be shown what extreme boulder cases are possible when trying to solve for the difference between ground and space based YORP measurements. The solution of boulder size and locations from YORP measurements will never be fully unique, but additionally applying knowledge of the geology of local materials and their breakup potential, it can be narrowed down that from a maximum boulder size of tens of meters, a certain percentage of them need to be in specific latitude ranges to induce observed YORP accelerations. Each new observation of an asteroid and measurement of its YORP acceleration opens up the possibilities for applying this statistical analysis.

## 5.3 Further Investigations

Future extensions of this work can involve inducing a time-varying thermal inertia. The assumption made in our equations of motion is that we can use a 1/8th period equivalent thermal lag for the obliquity varying equations. This approach would require re-deriving the equations of motion from Scheeres will retaining the consideration of a time-varying, or material-varying thermal inertia value. Other extensions of this work could include the integration of optical and thermal-based limb observations. Sensor fusion is often applied to enhance spacecraft navigation data products such as the trajectory, and in the case of shape modeling, one could observe the unlit side of the body which is still differentiable from space in the infrared wavelength. Another future

work possibility includes the integration of boulder motion in the dynamical sense, of propagating the asteroid spin and orbit dynamics through time and initiating a surface redistribution when facets reach their cohesive or friction limit. This is highly applicable to cases such as Apophis, which is an asteroid on course to come near the Earth in 2029. Planet conjunctions can induce large gravitational and centripetal forces through the hyperbolic flyby that could easily redistribute boulders on the surface. While this isn't expected for the body in question, it is an interesting problem for other more dynamic surfaces.

## Bibliography

- Bandyonadhyay, Santarshi et al. (2019). "Silhouette-Based 3D Shape Reconstruction of a Small Body from a Spacecraft". In: **IEEE Aerospace Conference Proceedings**. Vol. 2019-March. ISBN: 9781538668542. DOI: [10.1109/AERO.2019.8741753](https://doi.org/10.1109/AERO.2019.8741753).
- Barnouin, O. S. et al. (2022). "The Formation of Terraces on Asteroid (101955) Bennu". In: **Journal of Geophysical Research: Planets** 127.4, pp. 1–21. ISSN: 21699100. DOI: [10.1029/2021JE006927](https://doi.org/10.1029/2021JE006927).
- Bennett, C. A. et al. (2021). "A high-resolution global basemap of (101955) Bennu". In: **Icarus** 357.October 2019. ISSN: 10902643. DOI: [10.1016/j.icarus.2020.113690](https://doi.org/10.1016/j.icarus.2020.113690).
- Berry, Kevin et al. (2013). "OSIRIS-REx Touch-and-Go (TAG) Mission Design and Analysis". In: **36th Annual AAS Guidance and Control Conference**. Breckenridge, CO, pp. 1–12.
- Bierhaus, E. B. et al. (2022). "Crater population on asteroid (101955) Bennu indicates impact armouring and a young surface". In: **Nature Geoscience** 15.6, pp. 440–446. ISSN: 17520908. DOI: [10.1038/s41561-022-00914-5](https://doi.org/10.1038/s41561-022-00914-5).
- Bottke, William F. et al. (2006). "The Yarkovsky and YORP effects: Implications for asteroid dynamics". In: **Annual Review of Earth and Planetary Sciences** 34, pp. 157–191. ISSN: 00846597. DOI: [10.1146/annurev.earth.34.031405.125154](https://doi.org/10.1146/annurev.earth.34.031405.125154).
- Boyer, Edmond and Jean Sébastien Franco (2003). "A hybrid approach for computing visual hulls of complex objects". In: **Proceedings of the IEEE Computer Society Conference on Computer Vision and Pattern Recognition** 1. ISSN: 10636919. DOI: [10.1109/cvpr.2003.1211421](https://doi.org/10.1109/cvpr.2003.1211421).

- Brack, Daniel N. and Jay W. McMahon (2019). "Modeling the coupled dynamics of an asteroid with surface boulder motion". In: **Icarus** 333.January, pp. 96–112. ISSN: 10902643. DOI: 10.1016/j.icarus.2019.05.038. URL: <https://doi.org/10.1016/j.icarus.2019.05.038>.
- Breiter, S. and M. Murawiecka (2015). "Tumbling asteroid rotation with the YORP torque and inelastic energy dissipation". In: **Monthly Notices of the Royal Astronomical Society** 449.3, pp. 2489–2497. ISSN: 13652966. DOI: 10.1093/mnras/stv433.
- Breiter, S. and D. Vokrouhlický (2011). "Yarkovsky-O'Keefe-Radzievskii-Paddack effect with anisotropic radiation". In: **Monthly Notices of the Royal Astronomical Society** 410.4, pp. 2807–2816. ISSN: 13652966. DOI: 10.1111/j.1365-2966.2010.17663.x.
- Breiter, S. et al. (2009). "The YORP effect on 25 143 Itokawa". In: **Astronomy and Astrophysics** 507.2, pp. 1073–1081. ISSN: 00046361. DOI: 10.1051/0004-6361/200912543.
- Christian, John A. (2017). "Accurate planetary limb localization for image-based spacecraft navigation". In: **Journal of Spacecraft and Rockets** 54.3, pp. 708–730. ISSN: 00224650. DOI: 10.2514/1.A33692.
- Cicalò, S. and D. J. Scheeres (2010). "Averaged rotational dynamics of an asteroid in tumbling rotation under the YORP torque". In: **Celestial Mechanics and Dynamical Astronomy** 106.4, pp. 301–337. ISSN: 09232958. DOI: 10.1007/s10569-009-9249-7.
- Clauset, Aaron, Cosma Rohilla Shalizi, and M. E.J. Newman (2009). "Power-law distributions in empirical data". In: **SIAM Review** 51.4, pp. 661–703. ISSN: 00361445. DOI: 10.1137/070710111. arXiv: 0706.1062.
- Daly, M. G. et al. (2020a). "Hemispherical differences in the shape and topography of asteroid (101955) Bennu". In: **Science Advances** 6.41, pp. 1–12. ISSN: 23752548. DOI: 10.1126/sciadv.abd3649.
- Daly, R. T. et al. (2020b). "The Morphometry of Impact Craters on Bennu". In: **Geophysical Research Letters** 47.24. ISSN: 19448007. DOI: 10.1029/2020GL089672.
- Daly, R. Terik et al. (2024). "An Updated Shape Model of Dimorphos from DART Data". In: **Planetary Science Journal** 5.1. ISSN: 26323338. DOI: 10.3847/PSJ/ad0b07.

- Davidsson, Björn J.R. and Hans Rickman (2014). “Surface roughness and three-dimensional heat conduction in thermophysical models”. In: **Icarus** 243, pp. 58–77. ISSN: 10902643. DOI: 10.1016/j.icarus.2014.08.039.
- Davidsson, Björn J.R. et al. (2015). “Interpretation of thermal emission. I. The effect of roughness for spatially resolved atmosphereless bodies”. In: **Icarus** 252, pp. 1–21. ISSN: 10902643. DOI: 10.1016/j.icarus.2014.12.029.
- Delbo, Marco et al. (2015). “Asteroid thermophysical modeling”. In: **Asteroids IV**, pp. 107–128. DOI: 10.2458/azu\_uapress\_9780816532131-ch006. arXiv: 1508.05575.
- Delbo, Marco et al. (2022). “Alignment of fractures on Bennu’s boulders indicative of rapid asteroid surface evolution”. In: **Nature Geoscience** 15.6, pp. 453–457. ISSN: 17520908. DOI: 10.1038/s41561-022-00940-3.
- DellaGiustina, D. N. et al. (2018). “Overcoming the Challenges Associated with Image-Based Mapping of Small Bodies in Preparation for the OSIRIS-REx Mission to (101955) Bennu”. In: **Earth and Space Science** 5.12, pp. 929–949. ISSN: 23335084. DOI: 10.1029/2018EA000382. arXiv: 1810.10080.
- DellaGiustina, D. N. et al. (2019). “Properties of rubble-pile asteroid (101955) Bennu from OSIRIS-REx imaging and thermal analysis”. In: **Nature Astronomy** 3.4, pp. 341–351. ISSN: 23973366. DOI: 10.1038/s41550-019-0731-1.
- Durech, J. et al. (2023). “Secular change in the spin states of asteroids due to radiation and gravitation torques. New detections and updates of the YORP effect”. In: **Astronomy & Astrophysics** 93, pp. 1–25. ISSN: 0004-6361. DOI: 10.1051/0004-6361/202348350. arXiv: 2312.05157.
- E.E. Palmer, J.R. Weirich, O.S. Barnouin (2019). “Stereophotoclinometry Models in Support of the Osiris-Rex Mission”. In: **Lunar and Planetary Science Conference** 2019.2132, pp. 4–5.
- Franco, Jean-sébastien et al. (2009). “Efficient Polyhedral Modeling from Silhouettes To cite this version : HAL Id : inria-00349103 Efficient Polyhedral Modeling from Silhouettes”. In: **IEEE Transactions on Pattern Analysis and Machine Intelligence**.

- Fujiwara, A et al. (2006). "The Rubble-Pile Asteroid Itokawa as". In: **Science** 312.June, pp. 1330–1334.
- Gaskell, R. et al. (2006). "Landmark navigation studies and target characterization in the hayabusa encounter with itokawa". In: **Collection of Technical Papers - AIAA/AAS Astrodynamics Specialist Conference, 2006**. Vol. 3, pp. 1541–1552. ISBN: 1563478226. DOI: 10.2514/6.2006-6660.
- Gaskell, R. W. et al. (2008). "Characterizing and navigating small bodies with imaging data". In: **Meteoritics and Planetary Science** 43.6, pp. 1049–1061. ISSN: 10869379. DOI: 10.1111/j.1945-5100.2008.tb00692.x.
- Gaskell, Robert W (2004). "Optical Only Determination of Small Body Shape and Topography". In: pp. 1–28.
- Golish, D. R. et al. (2021). "A high-resolution normal albedo map of asteroid (101955) Bennu". In: **Icarus** 355. ISSN: 10902643. DOI: 10.1016/j.icarus.2020.114133.
- Golubov, O. and V. Lipatova (2022). "Analytic theory for the tangential YORP produced by the asteroid regolith". In: **Astronomy and Astrophysics** 666, pp. 1–8. ISSN: 14320746. DOI: 10.1051/0004-6361/202243320. arXiv: 2203.15567.
- Golubov, O., D. J. Scheeres, and Yu N. Krugly (2014). "A three-dimensional model of tangential yorp". In: **Astrophysical Journal** 794.1. ISSN: 15384357. DOI: 10.1088/0004-637X/794/1/22.
- Golubov, Oleksiy (2017). "Analytic Model for Tangential YORP". In: **The Astronomical Journal** 154.6, p. 238. ISSN: 00046256. DOI: 10.3847/1538-3881/aa88ba. arXiv: 1708.07988. URL: <http://dx.doi.org/10.3847/1538-3881/aa88ba>.
- Golubov, Oleksiy and Yurij N. Krugly (2012). "Tangential component of the YORP effect". In: **Astrophysical Journal Letters** 752.1. ISSN: 20418205. DOI: 10.1088/2041-8205/752/1/L11.
- Golubov, Oleksiy and Daniel J. Scheeres (2019). "Systematic Structure and Sinks in the YORP Effect". In: **The Astronomical Journal** 157.3, p. 105. ISSN: 1538-3881. DOI: 10.3847/1538-3881/aafdc. arXiv: 1901.02555. URL: <http://dx.doi.org/10.3847/1538-3881/aafdc>.

- Hartley, Richard and Andrew Zisserman (2000). **Multiple View Geometry in Computer Vision**. 2nd Editio. Cambridge University Press. ISBN: 9780521540513.
- Hergenrother, C. W. et al. (2019). “The operational environment and rotational acceleration of asteroid (101955) Bennu from OSIRIS-REx observations”. In: **Nature Communications** 10.1. ISSN: 20411723. DOI: 10.1038/s41467-019-09213-x.
- Holsapple, Keith A. (2010). “On YORP-induced spin deformations of asteroids”. In: **Icarus** 205.2, pp. 430–442. ISSN: 00191035. DOI: 10.1016/j.icarus.2009.08.014. URL: <http://dx.doi.org/10.1016/j.icarus.2009.08.014>.
- Jawin, E. R. et al. (2020). “Global Patterns of Recent Mass Movement on Asteroid (101955) Bennu”. In: **Journal of Geophysical Research: Planets** 125.9, pp. 1–21. ISSN: 21699100. DOI: 10.1029/2020JE006475.
- Jawin, E. R. et al. (2022). “Global geologic map of asteroid (101955) Bennu indicates heterogeneous resurfacing in the past 500,000 years”. In: **Icarus** 381.March, p. 114992. ISSN: 10902643. DOI: 10.1016/j.icarus.2022.114992. URL: <https://doi.org/10.1016/j.icarus.2022.114992>.
- Jones, R. Lynne, Mario Jurić, and Željko Ivezić (2016). “Asteroid Discovery and Characterization with the Large Synoptic Survey Telescope”. In: **Proceedings of the International Astronomical Union** 10.318, pp. 282–292. ISSN: 17439221. DOI: 10.1017/S1743921315008510. arXiv: 1511.03199.
- Kanamaru, Masanori et al. (2021). “YORP Effect on Asteroid 162173 Ryugu: Implications for the Dynamical History”. In: **Journal of Geophysical Research: Planets** 126.12, pp. 1–23. ISSN: 21699100. DOI: 10.1029/2021JE006863.
- Küppers, Michael et al. (2012). “Boulders on Lutetia”. In: **Planetary and Space Science** 66.1, pp. 71–78. ISSN: 00320633. DOI: 10.1016/j.pss.2011.11.004.
- Lauretta, D. S. et al. (2019). “The unexpected surface of asteroid (101955) Bennu”. In: **Nature** 568.7750, pp. 55–60. ISSN: 14764687. DOI: 10.1038/s41586-019-1033-6.

- Lauretta, Dante S et al. (2023). "Origins, Spectral Interpretation, Resource Identification, and Security-Regolith Explorer (OSIRIS-REx) Project Sample Analysis Plan". In: **NASA OSIRIS-REx PI Office**.
- Li, Shuang et al. (2013). "Image processing algorithms for deep-space autonomous optical navigation". In: **Journal of Navigation** 66.4, pp. 605–623. ISSN: 03734633. DOI: 10.1017/S0373463313000131.
- Liounis, Andrew J (2018). "Limb-Based Optical Navigation for Irregular Bodies". In: **RPI Space Imaging Workshop**, pp. 1–17.
- Lowe, David G (2004). "Distinctive Image Features from Scale-Invariant Keypoints". In: **International Journal of Computer Vision**, pp. 1–28.
- Lowry, Stephen C. et al. (2007). "Direct detection of the asteroidal YORP effect". In: **Science** 316.5822, pp. 272–274. ISSN: 00368075. DOI: 10.1126/science.1139040.
- Mainzer, A. et al. (2011). "Neowise observations of near-earth objects: Preliminary results". In: **Astrophysical Journal** 743.2. ISSN: 15384357. DOI: 10.1088/0004-637X/743/2/156. arXiv: 1109.6400.
- Manni, Jonathan D (2020). "Template Matching for Terrain Relative Navigation under Varying Lighting Conditions". Masters. University of Colorado at Boulder, pp. 1–117.
- Matusik, W. et al. (2000). "Image-based visual hulls". In: **Proceedings of the ACM SIGGRAPH Conference on Computer Graphics**, pp. 369–374. DOI: 10.1145/344779.344951.
- Michikami, Tatsuhiro et al. (2008). "Size-frequency statistics of boulders on global surface of asteroid 25143 Itokawa". In: **Earth, Planets and Space** 60.1, pp. 13–20. ISSN: 18805981. DOI: 10.1186/BF03352757.
- Molaro, J. L. et al. (2020). "In situ evidence of thermally induced rock breakdown widespread on Bennu's surface". In: **Nature Communications** 11.1, pp. 1–11. ISSN: 20411723. DOI: 10.1038/s41467-020-16528-7. URL: <http://dx.doi.org/10.1038/s41467-020-16528-7>.
- Murdoch, Naomi et al. (2015). "Asteroid surface geophysics". In: **Asteroids IV**, pp. 767–792. DOI: 10.2458/azu\_uapress\_9780816532131-ch039. arXiv: 1503.01931.

- Nolan, M. C. et al. (2019). "Detection of Rotational Acceleration of Bennu Using HST Light Curve Observations". In: **Geophysical Research Letters** 46.4, pp. 1956–1962. ISSN: 19448007. DOI: 10.1029/2018GL080658.
- Owen, William M (2011). "METHODS OF OPTICAL NAVIGATION". In: **AAS Spaceflight Mechanics Conference**. New Orleans, Louisiana: Pasadena, CA : Jet Propulsion Laboratory, National Aeronautics and Space Administration, pp. 1–19.
- Pajola, M et al. (2024). "The Didymos and Dimorphos global boulder size-frequency distributions : implications on their mutual origin". In: **AAS Lunar and Planetary Science Conference**, pp. 5–6.
- Panicucci, Paolo et al. (2020). "Polyhedral Shape from Silhouettes for Small Body". In: **AAS GN&C Conference**, pp. 1–12.
- Pesce, Vincenzo, Ali Akbar Agha-Mohammadi, and Michèle Lavagna (2018). "Autonomous navigation & mapping of small bodies". In: **IEEE Aerospace Conference Proceedings** 2018-March, pp. 1–10. ISSN: 1095323X. DOI: 10.1109/AERO.2018.8396797.
- Raducan, Sabina et al. (2024). "Physical properties of asteroid Dimorphos as derived from the DART impact". In: **Nature Astronomy**. DOI: 10.1038/s41550-024-02200-3. URL: <https://doi.org/10.21203/rs.3.rs-2886652/v1>.
- Rozitis, B. and S. F. Green (2011). "Directional characteristics of thermal-infrared beaming from atmosphereless planetary surfaces - a new thermophysical model". In: **Monthly Notices of the Royal Astronomical Society** 415.3, pp. 2042–2062. ISSN: 13652966. DOI: 10.1111/j.1365-2966.2011.18718.x.
- (2012). "The influence of rough surface thermal-infrared beaming on the Yarkovsky and YORP effects". In: **Monthly Notices of the Royal Astronomical Society** 423.1, pp. 367–388. ISSN: 13652966. DOI: 10.1111/j.1365-2966.2012.20882.x.
- (2013). "The strength and detectability of the YORP effect in near-Earth asteroids: A statistical approach". In: **Monthly Notices of the Royal Astronomical Society** 430.2, pp. 1376–1389. ISSN: 00358711. DOI: 10.1093/mnras/sts723.

- Rozitis, B. et al. (2020). "Asteroid (101955) Bennu's weak boulders and thermally anomalous equator". In: **Science Advances** 6.41. ISSN: 23752548. DOI: 10.1126/sciadv.abc3699.
- Rubincam, David Parry (2000). "Radiative Spin-up and Spin-down of Small Asteroids". In: **Icarus** 148.1, pp. 2–11. ISSN: 00191035. DOI: 10.1006/icar.2000.6485.
- Saito, J. et al. (2006). "Detailed images of asteroid 25143 Itokawa from Hayabusa". In: **Science** 312.5778, pp. 1341–1344. ISSN: 00368075. DOI: 10.1126/science.1125722.
- Scheeres, D. J. (2007). "The dynamical evolution of uniformly rotating asteroids subject to YORP". In: **Icarus** 188.2, pp. 430–450. ISSN: 00191035. DOI: 10.1016/j.icarus.2006.12.015.
- (2015). "Landslides and Mass shedding on spinning spheroidal asteroids". In: **Icarus** 247, pp. 1–17. ISSN: 10902643. DOI: 10.1016/j.icarus.2014.09.017. arXiv: 1409.4015. URL: <http://dx.doi.org/10.1016/j.icarus.2014.09.017>.
- (2018). "Disaggregation of small, cohesive rubble pile asteroids due to YORP". In: **Icarus** 304, pp. 183–191. ISSN: 10902643. DOI: 10.1016/j.icarus.2017.05.029. arXiv: 1706.03385. URL: <https://doi.org/10.1016/j.icarus.2017.05.029>.
- Scheeres, D. J. et al. (2007). "The effect of YORP on Itokawa". In: **Icarus** 188.2, pp. 425–429. ISSN: 00191035. DOI: 10.1016/j.icarus.2006.12.014.
- Scheeres, D. J. et al. (2016). "The geophysical environment of Bennu". In: **Icarus** 276, pp. 116–140. ISSN: 10902643. DOI: 10.1016/j.icarus.2016.04.013. URL: <http://dx.doi.org/10.1016/j.icarus.2016.04.013>.
- Scheeres, D. J. et al. (2019). "The dynamic geophysical environment of (101955) Bennu based on OSIRIS-REx measurements". In: **Nature Astronomy** 3.4, pp. 352–361. ISSN: 23973366. DOI: 10.1038/s41550-019-0721-3.
- Scheeres, Daniel J. and Sepidehsadat Mirrahimi (2008). "Rotational dynamics of a solar system body under solar radiation torques". In: **Celestial Mechanics and Dynamical Astronomy** 101.1-2, pp. 69–103. ISSN: 09232958. DOI: 10.1007/s10569-007-9116-3.

- Ševeček, P. et al. (2016). "Obliquity dependence of the tangential YORP". In: **Astronomy and Astrophysics** 592, pp. 1–6. ISSN: 14320746. DOI: 10.1051/0004-6361/201628746. arXiv: 1605.06959.
- Statler, Thomas S. (2009). "Extreme sensitivity of the YORP effect to small-scale topography". In: **Icarus** 202.2, pp. 502–513. ISSN: 00191035. DOI: 10.1016/j.icarus.2009.03.003. URL: <http://dx.doi.org/10.1016/j.icarus.2009.03.003>.
- Tang, Y. et al. (2023). "Simulating impact-induced shaking as a triggering mechanism for mass movements on Bennu". In: **Icarus** 395.October 2022, p. 115463. ISSN: 10902643. DOI: 10.1016/j.icarus.2023.115463. URL: <https://doi.org/10.1016/j.icarus.2023.115463>.
- Vokrouhlický, D., A. Milani, and S. R. Chesley (2000). "Yarkovsky Effect on Small Near-Earth Asteroids: Mathematical Formulation and Examples". In: **Icarus** 148.1, pp. 118–138. ISSN: 00191035. DOI: 10.1006/icar.2000.6469.
- Walsh, K. J. et al. (2019). "Craters, boulders and regolith of (101955) bennu indicative of an old and dynamic surface". In: **Nature Geoscience** 12.April, pp. 242–246. ISSN: 17520908. DOI: 10.1038/s41561-019-0326-6.
- Walsh, Kevin J. (2018). "Rubble Pile Asteroids". In: **Annual Review of Astronomy and Astrophysics** 56, pp. 593–624. ISSN: 00664146. DOI: 10.1146/annurev-astro-081817-052013.
- Watanabe, S. et al. (2019). "Hayabusa2 arrives at the carbonaceous asteroid 162173 Ryugu-A spinning top-shaped rubble pile". In: **Science**. ISSN: 10959203. DOI: 10.1126/science.aav8032.
- Zhang, Yun et al. (2022). "Inferring interiors and structural history of top-shaped asteroids from external properties of asteroid ( 101955 ) Bennu". In: **Nature Communications**. DOI: 10.1038/s41467-022-32288-y.
- Zhou, Wen-Han and Patrick Michel (2023). "A semi-analytical thermal model for craters with application to the crater-induced YORP effect". In: **Astronomy & Astrophysics** 130, pp. 1–13. ISSN: 0004-6361. DOI: 10.1051/0004-6361/202346970.
- Zhou, Wen-Han et al. (2022). "The crater-induced YORP effect". In: **Astronomy & Astrophysics** 1.1. arXiv: 2210.15802. URL: <http://arxiv.org/abs/2210.15802>.